Uncertainties in the Hydrological Modelling Using Remote Sensing Data over the Himalayan Region

Thesis submitted in partial fulfilment

of the requirements of the degree of

Doctor of Philosophy

in

Civil Engineering

by

Brijesh Kumar

(Roll Number: 513CE1004)

based on research carried out

under the supervision of

Prof. Kanhu Charan Patra

March, 2017

Department of Civil Engineering

National Institute of Technology Rourkela

Department of Civil Engineering
National Institute of Technology Rourkela

March 31, 2017

Certificate of Examination

Roll Number: *513CE1004*
Name: *Brijesh Kumar*
Title of Dissertation: *Uncertainties in the Hydrological Modelling using Remote Sensing Data over the Himalayan Region.*

We the below signed, after checking the dissertation mentioned above and the official record book (s) of the student, hereby state our approval of the dissertation submitted in partial fulfilment of the requirements of the degree of *Doctor of Philosophy in Civil Engineering* at National Institute of Technology Rourkela. We are satisfied with the volume, quality, correctness, and originality of the work.

Kanhu Charan Patra Supervisor	Awadhesh Kumar Member (DSC)
Md. Equeenuddin Member (DSC)	Abanti Sahoo Member (DSC)
External Examiner	Shishir Kumar Sahu DSC, Chair Person

Department of Civil Engineering
National Institute of Technology Rourkela

Kanhu Charan Patra

Professor

March 31, 2017

Supervisors' Certificate

This is to certify that the work presented in the dissertation entitled *Uncertainties in the Hydrological Modelling using Remote Sensing Data over the Himalayan Region* submitted by *Brijesh Kumar*, Roll Number *513CE1004*, is a record of original research carried out by him under my supervision and guidance in partial fulfilment of the requirements of the degree of *Doctor of Philosophy in Civil Engineering*. Neither this dissertation nor any part of it has been submitted earlier for any degree or diploma to any institute or university in India or abroad.

Kanhu Charan Patra
Professor

Dedication

This thesis is dedicated to my parents Smt. Laxmi Devi Tiwari and Shri Govinda Prasad Tiwari; for their intensive care and blessings.

Brijesh Kumar

Declaration of Originality

I, Brijesh Kumar, Roll Number 513CE1004 hereby declare that this dissertation entitled "*Uncertainties in the Hydrological Modelling using Remote Sensing Data over the Himalayan Region*" represents my original work carried out as a doctoral student of NIT Rourkela and, to the best of my knowledge, it contains no material previously published or written by another person, nor any material presented for the award of any other degree or diploma of NIT Rourkela or any other institution. Any contribution made to this research by others, with whom I have worked at NIT Rourkela or elsewhere, is explicitly acknowledged in the dissertation. Works of other authors cited in this dissertation have been duly acknowledged under the section "References". I have also submitted my original research records to the scrutiny committee for evaluation of my dissertation.

I am fully aware that in case of any non-compliance detected in future, the Senate of NIT Rourkela may withdraw the degree awarded to me on the basis of the present dissertation.

March 31, 2017 *Brijesh Kumar*

NIT, Rourkela

Acknowledgement

I sincerely thank my supervisor, Prof. Kanhu Charan Patra for guiding me into this research field and for his constant help, encouragement, and endless support on my research work. His care and enlightenment strengthen every progress in this work.

I would like to express my profound gratitude to my mentor Prof. Venkat Lakshmi, School of Earth, Ocean and Environment, University of South Carolina, USA for his valuable suggestions throughout my research work. Prof. Lakshmi was the person who continuously motivated during my tough time and pulled me out to reach this work. His ten "V-Directions" has changed my though processes to progress in this research work. So, I am very grateful for his immense help.

I would like to convey my sincere gratitude to Prof. S.K. Sahu, DSC, Chair/Head Department of Civil Engineering, National Institute of Technology Rourkela, for his constant guidance and encouragement. I would also like to express my sincere thanks to Dr. N. Roy, Dr. S.P. Singh, Dr. M. Panda, Dr. C.R. Patra, Dr. K.C. Biswal, Dr. S.K. Das and Dr. M.Barik for their valuable suggestions at various time. I am also thankful to Dr. K. K. Khatua, Dr. P.K. Bhuyan, Dr. S.N. Sahoo, Dr. Robin Devis and Dr. R.N. Behera for their love and support. I would also like to take the pleasure of thanking my doctoral scrutiny committee members Dr. A. Kumar, Dr. Md. Equeenuddin and Dr. Abanti Sahoo for assessing my research work and providing me the valuable suggestions throughout the work.

Special thanks are due to Dr. Pramod Kumar Pandey, Faculty at Department of Population Health and Reproduction, University of California at Davis, CA and Prof. Mukesh Kumar, Nicholas School of Environment, Duke University USA for their enriching ideas and fruitful discussions. I also want to acknowledge here my dear friends Dr. Bin Fang, Dr. Mehmat Ercan, Dr. Jessica Price Sutton, Dr. Sachin Dev Verma and Mr. Ashwin patthi, University of South Carolina, USA for their help and encouragement during my stay in the Columbia, South Carolina.

I am grateful to two esteemed organizations Central Water Commission (CWC) Government of India and Department of Hydrology and Meteorology (DHM), Nepal for providing me the various hydrological and meteorological observations. I also want to acknowledge the names of Mr. Suresh Maskey and Mr. Saket Karn of DHM and Rajesh Singh (CWC, Patna) for their timely help during data collection. I also want to thanks Mr. Dilip Kumar Jena (CWC, Bhubaneswar) for their help during my initial work on Mahanadi River.

During my Ph.D work, I am very much grateful to my friends especially Nibedita Guru, Janki Ballabh Swain, Mrunmayee Manjari Sahoo, Abinash, Arpan Pradhan, Sachin, Swati Mishra, Gaurav Singh, Chudamani Dev Mishra, Rajesh, Shivam Gupta, Amarit, Shushindra, Anil Bankoti, Mayank Chaubey and Abhishek Sharma for their kind care, selfless help, and the deep friendship.

Finally, I wish to express my hearted appreciation to my Parents Mrs. Laxmi Devi and Mr. Givinda Prasad and my siblings Rakesh, Mukesh, Poonam, cousins Asha, Ashish, Dhiru. Their deep love, understanding, constant support and encouragement over the years are the great impetus to my study.

March 31, 2017 *Brijesh Kumar*

NIT, Rourkela Roll Number. 513CE1004

Abstract

Himalayas the “roof of the world” are the source of water supply for major South Asian Rivers and fulfill the demand of almost one sixth of world’s humanity. Hydrological modeling poses a big challenge for Himalayan River Basins due to complex topography, climatology and lack of quality input data. In this study, hydrological uncertainties arising due to remotely sensed inputs, input resolution and model structure has been highlighted for a Himalayan Gandak River Basin.

Firstly, spatial input DEM (Digital Elevation Model) from two sources SRTM (Shuttle Radar Topography Mission) and ASTER (Advanced Space borne Thermal Emission and Reflection Radiometer) with resolutions 30m, 90m and 30m respectively has been evaluated for their delineation accuracy. The result reveals that SRTM 90m has best performance in terms of least area delineation error (13239.28 km^2) and least stream network delineation error.

The daily satellite precipitation estimates TRMM 3B42 V7 (Tropical Rainfall Monitoring Mission) and CMORPH (Climate Prediction Center MORPHing Technique) are evaluated for their feasibly over these terrains. Evaluation based on various scores related to *visual verification method*, *Yes/no dichotomous*, and *continuous variable verification method* reveal that TRMM 3B42 V7 has better scores than CMORPH.

The effect of DEM resolution on the SWAT (Soil Water Assessment Tool) model outputs has been demonstrated using sixteen DEM grid sizes (40m-1000m). The analysis reveals that sediment and flow are greatly affected by the DEM resolutions (for DEMs>300m). The amount of total nitrogen (TN) and total phosphorous (TP) are found affected via slope and volume of flow for DEM grid size ≥150m. The *T-test* results are significant for SWAT outputs for grid size >500m at a yearly time step.

The SWAT model is accessed for uncertainty during various hydrological processes modeling with different setups/structure. The results reflects that the use of elevation band modeling routine (with six to eight elevation bands) improves the streamflow statistics and water budgets from upstream to downstream gauging sites. Also, the SWAT model represents a consistent pattern of spatiotemporal snow cover dynamics when compared with MODIS data.

At the end, the uncertainty in the stream flow simulation for TRMM 3B42 V7 for various rainfall intensity has been accessed with the statistics Percentage Bias (PBIAS) and RSR (RMSE-observations Standard Deviation Ratio). The results found that TRMM simulated streamflow is suitable for moderate (7.5 to 35.4 mm/day) to heavy rainfall intensities (35.5 to 124.4 mm/day). The finding of the present work can be useful for TRMM based studies for water resources management over the similar parts of the world.

Keywords: Uncertainty, Hydrological modeling, SWAT, Himalayas, Gandak Basin

Table of Contents

List of Figures

List of Tables

Chapter 1

Introduction

1.1 Overview

Hydrological processes modeling is a challange for Himalayan River Basins due to lack in the understanding of the hydrological regimes, acting as one of the primary source of uncertainty in measuring the regional hydrological inputs [1]. Diverse topography and climate create a hurdle to reaching an altitude >4000m to conduct meaningful research. However, it is evident that an alternative to traditional "alpine" meteorology, topography and glaciology are required for Hindu-Kush Himalayan Regions [2,3]. Hydrological uncertainty may arise from a variety of sources, such as inputs forcing, calibration accuracy and parameter's uncertainty and sensitivity [4]. Therefore, evaluation of available inputs and model structure for possible uncertainties is the need of the day for further hydrological processes modeling and climate change studies in the region [5]. Understanding hydrological uncertainties in River Basins requires a symbiotic union of simulation results versus field observations. To emphasize on monitoring model uncertainties in the hydrological simulations, it requires an enhancement of our knowledge on how the combined impacts of input forcing, model parameters and model structure influence the precipitated water into hydrological processes. This research facilitates satellite based remote sensing observations, ground truth data (*in-situ* observations) and computational modeling approaches to improve our understanding on hydrological processes modeling over the alpine Himalayas.

1.2 Goals and objectives

The overall objective of this research is to improve our understanding of various uncertainties for hydrological processes modeling over the alpine Himalayan regions. Here validation of input forcing have been carried out with the measured in-situ data and then simulated hydrological processes considering uncertainties in the inputs and model structure. Himalayan River Basin 'Gandak' - a trans-boundary basin between China, Nepal and India is being selected for the present research work.

In addition, hydrological processes modeling for the basin with best possible input forcing and model structure have been carried out which will enhance our understanding for water management, flood forecasting and climate change studies.

To accomplish the above said broad themes, following specific objectives have been set for the present research work.

1. Evaluating the uncertainties in the input forcing
   (a) DEMs: Error in the river network and basin area delineation, and
   (b) Satellite Rainfall: Error in the amount and frequency of satellite precipitation.

   Hypothesis: Uncertainties in the outputs of a hydrological model are due to quality of two major inputs viz. (a) DEMs (b) Rainfall.

2. Study of uncertainties arising due to change in the spatial input: DEM grid size.

   Hypothesis: The DEM grid size significantly affects the specific hydrological outputs and the results can be improved by using appropriate DEM grid size.

3. Performance evaluation of different modeling structure of SWAT model.

   Hypothesis: Selection of suitable model parameters and modeling routines appropriately divides the precipitated water into different hydrological components and thus, improves the hydrological water balance.

4. Assessing the suitability of satellite precipitation (TRMM) to simulate streamflow during extreme rain events considering uncertainties in the inputs and model's routine.

   Hypothesis: Uncertainty in the satellite precipitation product (TRMM) may have significant impact in the simulated discharge for various rainfall intensity classes.

1.3 Thesis organization

The research done in this project has been divided into seven segments/chapters. The first segment (Chapter 2) deals with the literature reviews pertaining to the various types of uncertainties, and the chorological advancement made to reduce it. The second segment (Chapter 3) describes the physical, topographical, and climatological overview of the study area in general.

The third segment (Chapter 4) is focused on assessing the qualitative and quantitative error in the two prime model inputs viz. available DEMs and satellite precipitation product TRMM 3B42 and CMORPH. In DEMs accuracy assessment, error in stream network and basin area delineation have been analyzed for three different DEMs, SRTM30, ASTER30m and SRTM 90m that has been published in *Journal of Geological society of India, Springer,* 89(1), pp-65-70. In order to derive stream and basin area delineation, flow direction have been computed using "D8 method" inbuilt in ArcGIS 10.2. Thereafter, digitally generated stream network is compared with the stream network manually digitized over Google Earth Imagery. The automatically generated basin area is compared with basin area map published by Ganga Flood Control Commission (GFCC), Gov. of India in year 2000. Secondly, the reliability of satellite precipitations products TRMM 3B42 and CMOPRPH have been validated for quantitative and qualitative measures using available rain gauge records in the study area. The measures for qualitative and quantitative assessments are visual verification, Yes/No dichotomous and Continuous variable verification methods. The validation of satellite precipitation for the study area is published in *Journal of Earth System Science, Springer,* 125 (5), pp-919-934.

In the next segment of the research work (Chapter 5), the suitable DEM grid size for various hydrological outputs in the SWAT model have been evaluatd. In this work, sixteen different DEM grid sizes ranging from 40-1000m are resampled with the three different methods; nearest neighborhood (N), bilinear (B) and cubic convolution (C). Thereafter, all the forty eight DEMs scenarios are used as input with the fixed parameters in the SWAT model. Then, all the DEM scenarios are evaluated for possible uncertainties into the topographical derivatives and SWAT outputs. The optimum grid size values have been highlighted for each SWAT output using statistical measures relative differences (RD) and test of significance statistics "*t-Test*". The work has been published in *Journal of Hydrological Engineering, ASCE, 22 (9)* pp-04017039.

Chapter 6 of research work is concentrated in the output uncertainty arising due to model structure. In the Himalayan region, it is very important to find out suitable modeling routine to simulate various hydrological processes. For this, the SWAT model has been evaluated for its three modeling routines viz. reference project, snow project and elevation band project. Thereafter, the best modeling routines with the suitable parameters have been found out for the partitioning of precipitated water into hydrological components. Spatial variation of snow dynamics between SWAT and satellite based MODIS snow cover product

has also been evaluated in this chapter. This work is under review with the *Journal of Hydrology, Elsevier*.

The last part of the research (Chapter 7) is basically to evaluate the feasibility of satellite precipitation product Tropical Rainfall Monitoring Mission (TRMM) to simulate the stream flow for extreme rain events over the study area. For this, the best SWAT model setup and parameters evaluated in the chapter 6 have been used during streamflow simulation with TRMM 3B42 V7 precipitation product. This work has been accepted in *Journal of Earth System Sciences, Springer* for the publication.

Chapter 8 cover the conclusions drawn from the each segment of the research work in general. Thereafter, the scope for the future work and whole bibliography have been listed in the reference section.

Chapter 2

Literature Review

2.1 Background

What do we mean by term uncertainty? The word uncertainty needs to be correctly mentioned in hydrology assessment [6]. It is hard to find out a unique definition of uncertainty in the literature. Zadeh 2005 [7] defined that uncertainty can be considered as an attribute of information. This can be a realistic definition for hydrology, where uncertainty is usually dealt with the use of probability theory. During any modeling attempt, a vigorous reckonable understanding of its each elements is required to reduce the total predictive uncertainty. A robust classification of the uncertainties is a major challenge for operational hydrological modeling. In general, there are three major sources of uncertainty in hydrological modeling:

(1) Input uncertainty: uncertainties in the input forcing viz. DEM (topographical inputs), Meteorology (Rainfall) etc.
(2) Structural or Model uncertainty: error due to simplified and lumped illustration of hydrological processes in the model that may be due to modified modeling processes or altered inputs or change in the model's routine.
(3) Parametric uncertainty: error due to incapability to identify exact values of model parameters resulting from limited length, uncertainties in the calibration data, model approximations and imperfect process understanding, etc.

Therefore, meaningful assessment of data and structural uncertainties in the hydrological modeling is a key scientific and engineering challenge [8].

To address the uncertainty in the hydrological simulations, there are following three separate approaches to be followed viz. understanding, quantification and way to reduce the

uncertainty. Understanding uncertainty is a part of its quantification and minimization. However to quantify uncertainty, many uncertainty analysis algorithms have been developed such as the Sequential Uncertainty Fitting algorithm (SUFI-2) methodology [9,10]. SUFI-2 algorithm can be implemented to better understand the parameters as well as to reduce uncertainty.

2.2 Input Uncertainty

Traditionally, researchers assume negligible error in data inputs that leads to bias in the parameterization and ultimately compromises with the model predictions. In response to this, a growing number of studies has been conducted to find out the error due to model inputs for example DEM [11–13], rainfall [14,15], land use[16], soil [17]. The land use and soil are relatively static than DEM and rainfall and therefore, DEM and rainfall may introduce significant error in the model prediction. In this study, two objectives have been focused for evaluation of error in the DEM and rainfall. The literature review for uncertainty due to error in DEMs and rainfall are presented here.

2.2.1 Digital Elevation Models (DEMs)

DEMs representing earth's surface digitally provides a base data for generation of topographic parameters used by various hydrological models. A significant research work has been done to address the uncertainty linked to error in DEMs and propagation of error for derived terrain parameters to modeling outputs [5]. A discussion on DEM uncertainty which affect the hydrological modeling can be divided into four broad areas viz. (1) error in DEM (2) topographic parameters derived from DEMs (3) influence of DEM grid size and resampling techniques on modeling outputs and (4) surface modification for hydrologic analyses.

2.2.1.1 Error in DEMs and Accuracy

DEM error at a given elevation is the relative $(\pm ve)$ departure from ground truth value. The different kinds of errors in DEMs have been compiled in the literature [18,19]. There are three basic category of DEM errors viz. systematic error, random error and blunders. Systematic error is due to procedural flaws during DEM generation that fallows a fixed pattern of bias. The blunders are vertical errors linked during the data collection processes and can be removed if known. The systematic error can be reduced or eliminated while

random error can't be eliminated and remains in the data. The error sources in the DEMs are (a) data error: due to age of data, lack in the density of spatial samples, (b) processing error: computational error like interpolation, classification and generalization error by computer (c) measurement errors: positioning error, fault during data entry or observation [18,20,21].

Various studies have been carried out to see the vertical accuracy of various open source DEMs. Petersen et al. 2009 [22] formed a field work on densely vegetated papyrus areas of southern Sudan and revealed that penetration depth of radar is 0.34m and a correction factor of 4.66m is needed between sensed and real surface. Mukherjee et al. 2013 [23] evaluated two open source DEMs in western part of Shivalik Himalayas using Cartosat DEM and Survey of India (SOI) height data and they found that the vertical accuracy has RMSE 12.62m and 17.76m for ASTER and SRTM DEMs respectively when compared with the Cartosat DEM. Muralikrishnan et al. 2013 [24] validated Indian DEM Cartosat-1 data for vertical accuracy and compared with the SRTM, ASTER and ICESat GLAS over flat and hilly areas. They concluded that the results of Carto DEM qualify for using operationally equivalent and better than open source DEMs like ASTER and SRTM. Djamel Athmania and Hammadi Achour, 2014 [25] evaluated the performance of SRTM v 4.1, ASTER GDEM2 and GMTED2010 in Tunisia and Algeria. They found that SRTM (3.6m, 8.3m) shows better vertical accuracy in terms of RMSE than ASTER (5.3m, 9.8m) and GMTED (4.5m, 9.6m) DEMs. Patel et al. 2016 [26] compared SRTM, ASTER and Cartosat DEMs with DGPS spot heights and concluded that Cartosat-1 DEM of 30m resolution is performing better than SRTM and ASTER in terms of lowest RMSE of 3.49m and ME of 2.49m without using any interpolation techniques, while Bilinear interpolation (BI) methods was found the best with less height deviation.

2.2.1.2 Error in Topographic Parameters Derived From DEMs

Topographic features are frequently derived from the DEMs that are used in hydrologic analyses. Erroneous DEMs may subsequently transfer the error to its derivative topographic features. It's not only error in DEM but GIS packages and algorithms to calculate these parameters have their own advantages and limitations. However, hydrologic community has not yet reached to a general consensus on suitable algorithms for certain topographic features viz. flow direction [5].

Raster grid structure (i.e. DEM) are used to calculate preliminary surface derivatives such as the slope, aspect and hill-shade that provide basis for the categorization of land forms. Routing of water flow is closely tied with the land forms. The calculation of flow direction is dependent on the slope and aspect of the area [27]. Drainage network, ridges and basin boundaries can be formed using flow direction and flow accumulation raster.

There are basically two types of method to calculate flow direction over the land surface. These are referred as single [28,29] or multiple path algorithms [30–32]. There have been numerous studies addressing error in topographical characteristics due to flow direction methods. Paz et al.2006 [33] mentioned the limitation in the COTAT algorithm of Reed 2003 [34] for coarser grid DEM along the meandering rivers. He modified this algorithm by considering minimum upstream flow path into the cell along with the area threshold. This new algorithm was being tested over rivers Tapajos and Grande in South America and results revealed that drainage network has been drastically improved, needing only a slight manual correction. Rampi et al. 2014 [35] compared single and multiple flow direction methods for compound topographic index (CTI) mapping of wetlands and revealed that multiple flow direction methods performs better than single flow direction methods.

2.2.1.3 Influence of DEM Grid Size and Resampling Techniques on Modeling Outputs

The DEM grid size commonly referred as grid cell indicates resolution of the DEM. Smaller grid cell indicates higher resolution and vise-versa. However, resampling methods are used to increase or decrease the DEM grid size. DEM accuracy decreases when it is being resampled to change the grid size [36]. High resolution data better represents the complex topography. This has led DEM user towards highest resolution, increasing cast and time for data acquisition and processing. Is higher resolution DEM necessarily better? To what extent is the grid cell of DEM a factor for propagation of error to derive terrain parameters? These question should be answered through proper research.

Wolock et al. 2000 [37] carried out a study to compare the topographical characteristics computed from 100m and 1000m grid size DEMs. They found that slope values are smaller for 1000m DEM than 100m DEM, however wetness index and specific catchment area are greater for the 1000-m DEMs compared to 100-m DEMs. Yang et al. 2001[38] investigated the sensitivity of width functions and area functions taken out from different resolution of DEMs over the fifteen Japanese catchment. They found that the river

networks generated from large threshold areas loses the detailed scaling information. Also the DEM resolution affects the runoff generation. Thereafter, a series of studies have been carried out in different climatic and topographic zones to ascertain the influence of DEM grid size in the modeling outputs [39–49].

2.2.1.4 Surface Reconditioning for Hydrologic Analyses

DEMs usually holds depression that lends as areas having no drainage, termed as pits or sinks. The depressions in the DEM disrupt the drainage surface and precludes routing of flow over the land surface. Therefore, to use DEMs to derive hydrological parameters such as flow direction, flow accumulation, upslope contributing area, sinks must be removed, as the "necessary evil" according to Burrough and McDonnell (1998) [50] and Rieger (1998) [51].

There are very few studies directly indicating effect of surface recondition methods on hydrology. Zhao et al. 2009 [52] compared two surface reconditioning methods viz. an agree procedure and shortest path method with and Xinanjiang model. They concluded that agree method provides better fit than shortest path method over hilly region, however, there was no significant difference in the modeled discharge between the two approaches.

2.2.2 Rainfall

It is important to characterize the uncertainty in the rainfall inputs for successful rainfall-runoff modeling. However, there is no physical or empirical model that can produce accurate runoff prediction if forced to an inaccurate rainfall data [53]. Erroneous rainfall inputs directly compromises with the model accuracy, reduces the scientific advancement as well as compromise with the consistency of operational applications. This is a major issue for hydrological modeling [54].

2.2.2.1 Sources of Error in Rainfall Inputs for Hydrological Modeling

The main source of uncertainty in the rain gauge data for hydrological modeling is due to the poor representation of discrete set of rain gauges over the entire basin [15,55,56] and the assumptions used to interpolate the rain rate between the gauging stations. The rain gauges like tipping bucket are themselves associated with the systematic and random error owing to mechanical limits, evaporation losses and wind effects [57–59]. While the satellite precipitation products have potential to providing integrated precipitation estimates over the

large spatial areas, although there are numerous challenges persist in the interpretation of the raw satellite data into quantitative precipitation intensities [15]. The number of satellite coverage has been significantly improved over the last few decades and therefore, provides the measurements at a very fine spatial and temporal resolution. Although, signal processing methods have been improved significantly [60,61], still there are many discrepancy in the quantitative precipitation estimates.

It has been recognized that the uncertainty in the rainfall estimates has a significant effect on the model predictions and efforts to develop scientific understanding through intervening model parameters and structure through incorrect assumptions on the quality of input rainfall used to predict the model outputs. Kavetski et al. 2006a [54], noted that regardless of advances in the data collection and modeling, high spatial and temporal variability of precipitation make it probable that the rainfall input uncertainty will remain a challenging issue in the near future. Reichert and Miele itner, 2009 [62] revealed that the consideration of time dependency in the rainfall bias correction has improved the model performance more than the inclusion of any other time dependent parameters. Recently some studies are carried out to describe the error propagation in the streamflow [63] as well as the byproducts streamflow like flood forecasting [64].

2.2.2.2 Quantification of Error in Satellite Precipitation Products

Last one decades, many studies have been carried out to understand the uncertainty in the satellite and forecasted precipitation products out of which legitimate reviews are presented in three sections namely validation, improvement (Bias adjustment) and Hydrological applications.

Validation

Din et al. 2008 [65] compared site specific precipitation between TRMM and rain gauge data over Kuwait, and showed that the bilinear interpolated satellite data are highly correlated with the rain gauge data, aspersions exist for overestimation caused due to the missing of particular rain events by satellite owing to its temporal variability. Elizabeth E. Ebert 2008 [66], proposed a fuzzy verification (which uses a spatial window or neighborhood surrounding the observed point using average, threshold or PDF depending upon the fuzzy method) to validate high-resolution precipitation forecast from the United Kingdom. Yu et al. 2009 [67] evaluated the ability of three satellite precipitation products

viz. TRMM 3B42 V6, CMORPH and GMS5-TBB for precipitation features during tropical cyclones over the main land of China. The results show that both the TRMM 3B42 and CMORPH underestimates the moderate and heavy rain fall and overestimates the low rainfall, while GMS5-TB performs better than 3B42 and CMORPH for heavy rainfall, therefore GMS5-TBB data could be useful for operational/research reference during tropical cyclones. Nair et al. 2009 [68] validated the TRMM 3B42 V6 data over the western state of India and found that the 3B42-V6 precipitation has potential to be used for intra-seasonal studies. Rahman et al. 2009 [69] investigated the variability in the Indian summer monsoon using daily data from satellite and gauge observations. They highlighted that the satellite data (TRMM and GPCP) are able to accurately depict the intra-seasonal variation but both underestimates mean and variability of rain.

Bias adjustment

Mitra and Bohra 2009 [70], presented an algorithm to merge TRMM TMPA satellite precipitation with Indian Meteorological Department (IMD) rain gauge data. The results demonstrate that the mean bias is smaller for merged gauge and satellite product (NMSG) than TMPA itself. Condom et al. 2011 [71] proposed additive and multiplicative correction model for TRMM 3B43 monthly precipitation estimates for the mountainous areas of the Peruvian Andes falling over 3000m. Then they verified the corrected monthly values with the gauge data and concluded that the correction models better approximates the TRMM rainfall at monthly and annual scale.

Hydrological applications

Harris et al. 2007 [72] tried to find out the answer of question *"what are the hydrologic implications of uncertainty of satellite rainfall data at the coarse scale"?* For this, they used TRMM's precipitation product 3B41RT which is availed in pseudo real time with a latency of 6-10 hours and concluded that a rational and regime based bias adjustment method is need to be investigated before using satellite precipitation data for the flood studies. Collischonn et al. 2008 [73] investigated the usefulness of daily TRMM precipitation data over an Amazon tributary- Tapajo´s river basin where convective precipitation is dominated. They found that TRMM-based simulated hydrographs are analogous with those obtained by the rain gauge data. Therefore, satellite precipitation can be a practical tool for identifying aberrant rain gauges at a basin scale. Yong el al. 2010 [74] validated standard TRMM precipitation products 3B42RT and 3B42V6 over the Laohahe

basin, China. The results shows that 3B42V6 data are able to capture spatial and temporal rainfall characteristics while 3B42RT product unrealistically overestimates throughout the year except for few months upon which it underestimates. Hydrological application with three layered variable invitation capacity model (VIC-3L) shows that model is not able to overcome the overestimating nature of 3B42RT product. However, It produces reasonable hydrological predictions with 3B42V6 data. They have also shown a significant geo-topography-dependent distribution pattern that is closely associated with latitude and elevation bands, signifying margins with TRMM-era algorithms at the mountainous areas in general. Moffitt et al. 2011 [75]carried out a research to see the acceptability of TRMM precipitation of flood detection system (FDS) over Ganges, Brahmaputra and Meghna Rivers in Bangladesh. They cautioned to verify FDS estimates during the monsoon period, although it provides high probability of detection for the flood events.

2.3 Structural or Model Uncertainty

Structural uncertainty is an intrinsic feature in the semi-distributed or conceptual models. The structural uncertainty coins during the model formulations where consequences of simplifying assumptions made to approximate the actual hydrological system with a series of mathematical formulations. In simple terms, the structural error of a model depends on the it's formulation (like number of layers and connective stores, options for constrictive functions etc.) for particular catchment and on the spatial and temporal scale of analysis. The structural uncertainty may vary from storm to storm or even for some specific time scale. Since it is not being considered well in past, stipulating a significant prior for structural uncertainty, indeed, even framing it mathematically, is indeed problematic.

In general, uncertainties in the calibration data (in terms of quality and finite length) inevitably translates uncertainties into the estimated model parameters and other secondary quantities (in a Bayesian perspective it is called as "posterior parameter uncertainty"). This can ensue even for an exact model, but can be predominantly prominent when the model is approximate. In Bayesian context, this "derived" parametric uncertainty decays as more data is included in the calibration. However, if the likelihood and/or priors are miss-specified, the posterior will be in error [76–80]. Despite being an asymptotic in behavior, parametric uncertainty should not be ignored, otherwise it may add a significant total predictive uncertainty.

The structural uncertainty broadly can be categorized in two different ways. In the first approach, model is treated as deterministic and structural error is represented by using an exogenous term that is usually additive in nature. There are several options to do this. In first approach (P1) modeler tries to get lumped output and structural errors into a single "residual" error term that is basically the difference between observed and simulated outputs, probably after a transformation. This approach can be executed in the systems that ignore input errors (e.g., the standard least squares calibration), and in the input error sensitive methodologies [81]. In second approach (P2), output and structural errors are represented by two terms e.g. difference between simulated and true output is termed as structural error, while the difference between true and observed outputs is the output error [82]. Though it needs a more specific error models and priors like assessment of stream flow uncertainty using independent gauge data and therefore specifying a significant prior for structural errors always persists problematic.

More current tactics has left the notion of model being deterministic owing to the stochastic nature of errors. The stochastic nature of errors are due to the spatial and temporal averaging of diverse and distributed model inputs and inner fluxes, which can't be avoided in the lumped models. There are several options to do this. The first tactic (S1) has been taken for state space approaches like Ensemble Kalman Filter (EnKf), termed as Stochastic perturbations of the internal model states [83]. In second method (S2), one or more model parameters varies stochastically through time. This tactic is used with the transfer function models that has been estimated with instrumental variables [84] or with general conceptual models within Bayesian total error analysis (BATEA) [54]. The third approach (S3) articulates the conceptual model itself as a combined probability density function [85].

In P1 and P2 tactics, model is deterministic and having given fixed inputs, initials and parameters, it generates the same output. However, in approaches S1-S3, the model is stochastic i.e. produces a random outputs even for fixed initials, inputs and model parameters. This is due to random disparity of internal states for S1 or stochastic parameters for S2 or due to probabilistic formulation within the model structure for S3. In result, for tactics P1 and P2, as posterior model uncertainty decays, the model predictions swiftly terms to deterministic and therefore total predictive uncertainty is led by the exogenous error term. On the other hand, in the tactics S1-S3, the model predictions are integrally stochastic even if the posterior parameters uncertainty are negligible. Also, it is obvious the approaches S1-

S3 implicitly or explicitly can be used to reveal all sources of uncertainty, rather than just showing inadequacies in the model structure.

The above list is not complete. The hypothesis of epistemic structural uncertainty (rather than strictly stochastic) ends the formal probabilistic framework, e.g., GLUE [86] and possiblistic methods [87] . Although structural errors are epistemic, it means arises due to lack of knowledge of basin dynamics, they may still behave stochastically. Therefore, they can be characterized by standard probability theory, in particular the Bayesian methods.

2.3.1 Uncertainty in SWAT Model

The SWAT model [88] has been proved an important tool to investigate alternative management strategies for hydrologic water quality response at the watershed scale. Significant information was provided to assist modellers to do sensitivity analysis, multisite calibration/validation and multivariable hydrological modelling using SWAT. White and Indrajeet 2005 [89] revealed that calibration and validation is vital factor to reduce the uncertainty and to increase the modellers assurance in SWAT model outcomes.

Alike other distributed models, SWAT is also affected with the equifinality of model parameters, because more than one set of parameters may produce the same outputs. Therefore, model sensitivity analysis is a crucial test which may decrease the model's uncertainty. In 2005, White and Indrajeet studied the influence of a set of parameters on flow, sediment, NO_3-N, NO_2-N and TP. The sensitivity analysis was carried out using relative sensitivity (Sr) and revealed that sensitivity of model parameter is proportional to the Sr value for each SWAT outputs. Also each considered output were first calibrated to ensure not to propagate the uncertainty to other output variables. In addition to that, uncertainty in the hydrological data was assumed to be less since the estimated flow was modelled from daily gauge.

Ömer and Serdar 2013 [90] applied SWAT model on a watershed and simulated the model for years 1978-2008, while calibrated the model for period 1998 to 2004. They found that few parameters are only valid on monthly basis, primarily those that have a direct effect on the watershed hydrology. These monthly parameters increases the uncertainty for daily simulations. The uncertainties in the volume of irrigation abstraction, results in poor model performance at the catchment outlet. The deficiency in the adequate number of gauge points on main channel and tributaries further deteriorated the modelling results. Furthermore,

Vishal et al. 2013 [91] highlighted that when considering all the uncertainties in the SWAT model, inputs and parameters, model predicts good at daily and monthly time steps for the Tungabhadra catchment.

2.4 Parametric Uncertainty

Semi-distributed hydrological models are highly parameterized and complex due to consideration of physical processes. For example, Y. Grusson et al. 2015 [92] started uncertainty analysis by taking 21 land parameters, 8 snow parameters and 2 elevation band parameters for simulation of stream flow and snow dynamics using SWAT model over the Garonne river basin, France. Therefore, more than one set of calibrated parameters maybe attained with equal streamflow simulations [93]. This means either model and/or measured data may not be feasible to signify the physical values. In addition to non-uniqueness and correlation in the sets of parameters, hydrologic models represents the simplified version of actual physical processes. Therefore, parameters of hydrological model itself produces uncertainty. Present method of hydrological modelling directs that parametric uncertainty is one of the most significant source of uncertainty [94–96]. Evaluation of parametric uncertainty is useful [97] to educate us on inability of a model to accurately depict the real world; imparts the knowledge on information reported; categorise the most and least important parameters; effort to identify place to put more effort to enhance the model output; re-build model; calculate statistical indicators of a model output; realize model strength and limitations.

The parameters for a hydrological model can be divided in two groups viz. conceptual and physical [98]. The conceptual parameters like CN2 in SWAT model are defined due to conceptualization of an un-definable physical process and that can be fixed by model calibration. Conversely, physical parameters (slope, river length, basin area etc.) can be measured or estimated based on the physical characteristics of watershed [99]. Due to spatial heterogeneity in the catchments and lack of experimental data, the physical parameters are usually fixed by model calibration against the measured hydrological data like discharge [100]. However, when number of considered parameters are large due to various sub-processes in the model structure, the calibration processes becomes complex and results uncertainty issue in the modelling [101]. It has been noticed that parametric uncertainty is unavoidable in hydrological modelling. Therefore, an uncertainty assessment should be conducted before prediction being used for decision making. A series of studies

have been conducted for parametric uncertainty analysis in the area of streamflow forecasting [91,102], soil loss assessment [103], integrated watershed modelling [104], effect of land use change on water resources analysis [105,106], climate change[107,108], nutrient flux analysis[109] and others. Nevertheless, identification of model parameters is a very complex and involves non-linearity. Numerous solutions can be obtained for the same project by the optimization algorithms [99] and thus, single set of parameters identification is not an easy task.

Several uncertainty analysis algorithms are developed in the past to take care of the uncertainty from hydrological models and derive significant uncertainty bounds for the modelling. These uncertainty optimization algorithms may be developed using either analytical and approximation methods [110], Monte Carlo (MC)[111,112], Bayesian sampling based methods [86,113], methods depend on the analysis of model errors [114–116] or uncertainty analysis methods based on the fuzzy set theory [117]. Majority of these methods consider model uncertainty from single source i.e. parametric uncertainty, considering correct model structure and input data free of impurities. However, recently few techniques have the capability to explicitly consider two or more sources of uncertainties [81,118–123]

To account for the parametric uncertainty, many uncertainty analysis algorithms have been developed. These uncertainty algorithms are applied to the hydrological models for uncertainty analysis, for example SWAT-CUP [10] for swat model, in which there are four parameterization and uncertainty analysis programmers, namely Sequential Uncertainty Fitting version-2 (SUFI-2), Generalized Likelihood Uncertainty Estimation (GLUE), Markov chain Monte Carlo (MCMC), Parameter Solution (ParaSol) and Particle Swarm Optimization (PSO). Many researchers have used these algorithms for SWAT model optimization worldwide; Rostamian et al. 2008 [124] used SUFI-2 algorithm to parameterize and calibrate the model for streamflow and sediment analysis in the Beheshtabad and Vanak river catchments in the central Iran; van Griensven et al. 2008 [125] used ParaSol method to approximate the parameters for Honey Creek watershed in Ohio, USA; Shen et al. 2012 [96] applied GLUE method to estimate the parameter uncertainty for streamflow and sediment modeling in the Daning River Basin, China; Samadi and Meadows 2014 [126] used PSO algorithm to explore uncertainty analysis in the SWAT model for the Waccamaw watershed, USA.

Apart from this, a few studies have compared different uncertainty analysis algorithms to establish their specific usefulness. Yang et al. 2008 [127] compared five uncertainty analysis algorithms viz. GLUE, ParaSol, MCMC, SUFI-2 and Importance Sampling (IS). Apart from this, they compared the results based on the posterior distributions, uncertainty in the prediction, conceptual base. The performances of the best estimates, computational efficiency and difficulties in the implementation illustrated that the Bayesian-based approaches is most suitable and has sound conceptual basis. Vishal Singh 2013 [91] compared SUFI-2 and GLUE methods over Tungabhadra catchment, India and found excellent agreement between observed and simulated streamflow at monthly level however, daily results exhibits good agreement for both the algorithms. Wu and Chen (2015) [128] carried out uncertainty analysis for distributed hydrological model over the Wenjing watershed, China using SUFI-2, ParaSol and GLUE methods. They found that the SUFI-2 algorithm better approximates the simulated results than the other two methods. Uniyal et al. 2015 [129] conducted the study for an eastern Indian catchment and reported that both SUFI-2 and GLUE are good in uncertainty analysis and expressed a need to conduct such types of studies in different catchments under varying agro-climatic conditions for assessing their generic capability.

In this study, the focus is particularly at input, structural or model and parametric uncertainties for hydrological modeling over the alpine Himalayas. In this chapter, the advancement in the understanding of different kind of uncertainties and possible rectification methods have been cited. The chronological reviews regarding specific knowledge gap for each objectives are being illustrated in the introduction section of each chapter.

Chapter 3

Description of the Study Area

In this chapter a brief description of study area has been provided. The chapter illustrates topography, climate, ecosystem, and man-made features present in the study site.

3.1 Topography

The primary sub-basins of the Ganges are Yamuna, Betawa, Chambal, Sone, Ram Ganga, Karnali, Gandak, Bagmati, and Kosi. The Gandak River Basin (GRB), taken as the study area for the present research work, is a trans-boundary river basin which drains water from China (Tibet), Nepal and India. It originates at an altitude of 7620m to the north- east of Dhaulagiri near the Nepal and China (Tibet) border at geographical location of 29.3^{o}N and 83.97^{o}E; however it confluences with the Ganga river near Patna, Bihar (India). After originating from a high altitude mountain range of the great Himalaya, it enters the plains at Triveni in the Champaran district of Bihar (India). The GRB covers a large geographical area of 44797 km^2 between 25.6^{o}- 29.4 ^{o} N and 82.8 ^{o}-85.82 ^{o} E of which 7620 km^2 falls in India and the rest in Nepal and Tibet. The location of the study area is shown in Figure (3.1). SRTM 90m derived DEM map (Figure 3.2) shows the altitude variation from lowest 33m in the plains to as high as 8143m toward the mountainous range of Tibet-Nepal.

The basin is also affected by human intervention, mainly due to the presence of dams at Kaligandaki-25 and Marsandi-28 sub-basins (Figure 3.1). These reservoirs support hydropower generation and do not store water during monsoons but marginally affects the flow regime during low flow period [130].

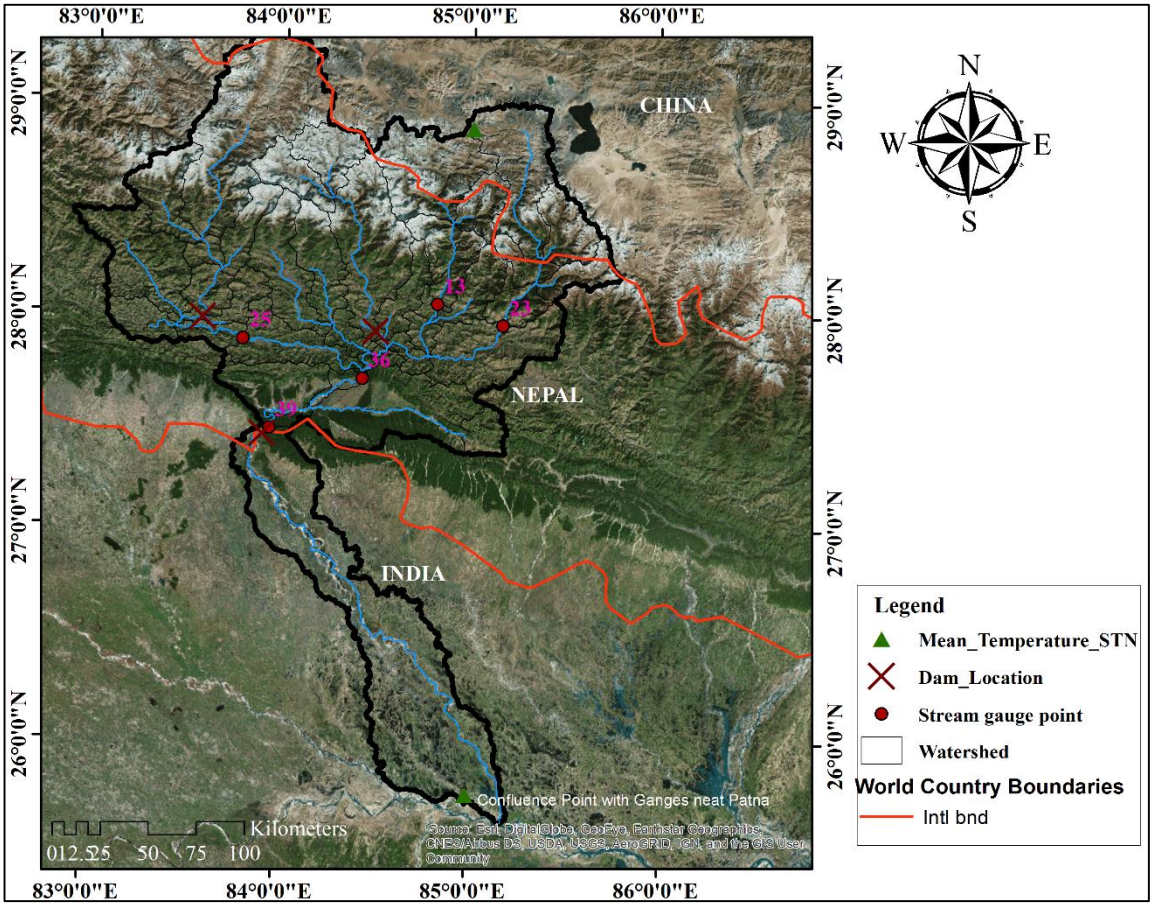

Figure 3.1: Location map of the study area

3.2 Ecosystem and Climate

The GRB contains a variety of ecosystems and biodiversities. It ranges from the alpine arid rain shadow areas in the Tibetan Plateau through the steep topography of the high mountains, including some of the world's highest points, Shivalik hills, Dhaulagiri (~8100m from MSL), down to the flat plains (33m from MSL) towards its confluence with the River Ganga at Patna. The Gandak River flows about 380 km in Nepal and Tibet and 260 km in India before reaching its confluence point.

Also, GRB has been divided into six major sub-catchments namely the Kali Gandak, Seti, Marshandi, Budhi Gadak, Trisuli and Rapti. Out of the six, five arise in the highly elevated areas of the Himalaya. Part of the basin basically Himalayan range falls in the dry alpine climate with the little precipitation. The southern part, which spreads from the mid-hills to the flat area, has a humid climate with relatively high precipitation. Based on the GlobeLand30 [131] land cover information 2010, GRB contains 33.1% forest, 22.04 agricultural land, 20.78% grassland, 10.24% ice/snow cover, 9.4 % barren land, and only 0.16 % urban land (Figure 3.2). According to the FAO soil classification (2003), the basins comprises of ten different types of soils dominated by various kinds of Cambisols (48%), Lithosols (29%), Fluvisols (9%), Glaciers (8.4%), Dystric Regosols (5%) and rest are rorthic Luvisols (Figure 3.2).

The climate of Gandak River Basin varies from the subtropical zone in the South to Tundra in the higher Himalayan regions. Based on the Climate Forecast System Reanalysis (CFSR) temperature data (1970-2013), mean daily maximum temperature range within the basin is 43.03 to -9.42^{o}C, while mean daily minimum temperature range is 29.37 to -27.22^{o}C. Temperature variability is dependent on the altitude. For example, daily mean maximum temperature in June for the stations 258850 (47m) and 289850 (5190m) (Figure 3.1) are 43.05^{o}C and 5.5^{o}C, respectively. High rain events exceeding intensity >124.4mm in 24- hour, frequently occur in the mid-hills over the Nepal portion of the GRB [132,133], bringing massive detachment of soil particles creating the muddy flows in Bihar, India.

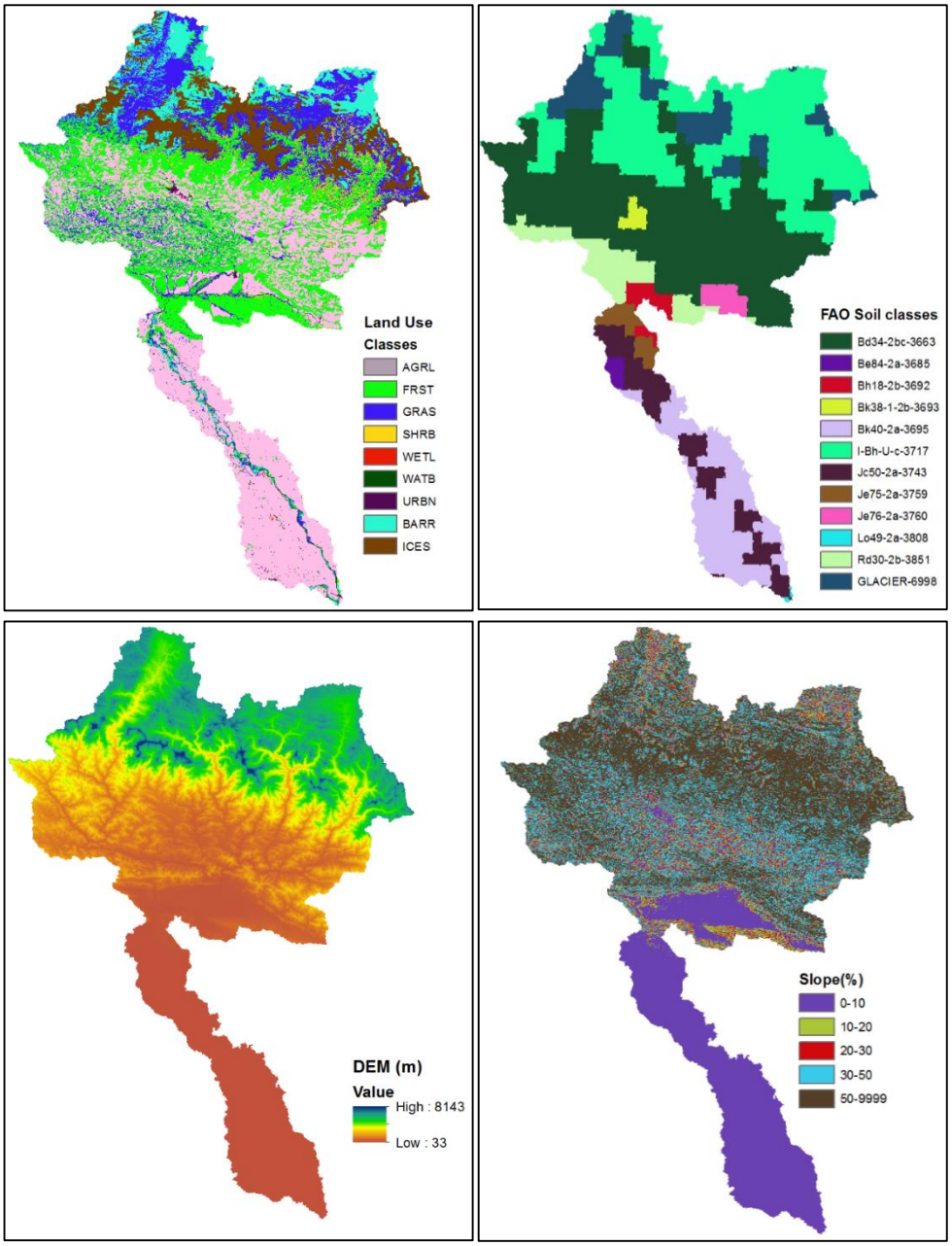

Figure 3.2: Land use map, Soil map, Digital Elevation Model (DEM) map, and Slope map of the study area

Chapter 4

Uncertainty in the Inputs

A watershed that has not been modelled effectively is not necessarily a monster. Indeed, if there are any monsters, one should first look for them in the realm of hydrological science [134]. The phrase "*garbage in, garbage out* (GIGO)" has been applied worldwide. In the developing nations, it is very difficult to rectify "*garbage in"* issue due to lack of quality inputs. Precipitation estimate and DEMs are the two major spatial inputs from remote sensors for distributed hydrological modelling. Therefore, in this chapter, the error in the by-products of DEM i.e. river network and basin area delineation as well as error in the amount and frequencies of satellite precipitation products such as the TRMM 3B42 V7 and CMROPH have been analysed.

4.1 DEMs: Error in Basin Morphology

4.1.1 Introduction

The fundamental topographic inputs used in distributed hydrological modeling are length, area and slope. Erroneous slope results incorrect estimation of velocities while errors in river reach length lead to incorrect dissemination time and false offsetting of flood waves. In the large basins, researchers are interested/or forced to reproduce the hydrological process with limited data. Advances in remote sensing (RS) and geographical information system (GIS) techniques has opened a new field for researchers in hydrological and hydraulic modeling using digital elevation models (DEMs) for extracting topographic information. Shuttle Radar Topographic Mission (SRTM) derived DEMs have been used in many river basins for hydrological process simulation worldwide [135–140].

The SRTM DEM data has been retrieved using radar imageries collected from NASA's shuttle. Two antennas receive the reflected radar pulses at the same time, one antenna located in the shuttle's cargo bay and other at the tip of a 60-m-long mast. This arrangement allows single pass radar interferometry and produces a very precise global elevation model with a vertical correctness of 6 m and a horizontal pixel spacing of 30m.

The data coverage is worldwide (latitudes 60N –60S) for three arc-second resolution, which can be retrieved freely from public domain website of the consultative group for international agriculture research (CGIAR) (http://srtm.csi.cgiar.org).

DEMs can be used to get several watershed characteristics required for hydrological simulation viz. area, slope, aspect, river length [141], but the assessment of the DEM accuracy is essential for the determination of correct watershed characteristics and to ensure accuracy in the further analysis. Many studies are carried out to assess the relevance of the obtained watershed characteristics using these DEMs. Han and Hammond 2006 [142], conducted a study on Brue catchment, Somerset, situated in the southwest of the England. The study was mainly oriented towards the effect of the different resolution of DEMs on the basin area delineation and concluded that the computer generated catchment area is not delineating correctly. It is mainly due to the weakness of computer to pick man-made features, in addition to data quality and algorithm problem. The study also revealed the fact that up to certain limit poor resolution data correctly delineate the catchment boundary than the high-resolution data.

Alarcon and O' Hara 2006 [143], carried out the research work to show the reliability of interferometric synthetic aperture radar, national elevation data (NED), United States Geographical services digital elevation model (USGS-DEM) and SRTM 30m DEM data. They found that 30m SRTM DEM delivers optimum delineation for basin area and perimeter as compared to NED elevation data.

Paz et al. 2008 [13] applied an automatic river length mining method in the Uruguay River Basin in Southern Brazil for eight river reaches. They concluded that the comparative inaccuracies can be higher than 30% in level regions with relatively low DEM resolution, but the stream burning operation significantly improves the results. Rahman et al. 2010 [11], conducted a study on flat deltas terrains of Bangladesh to evaluate the limitation of SRTM 90m DEM in river network delineation and the results reveal that error is proportional to flatness.

These above studies carried out using a well-known D8 method introduced by O'Callaghan and Mark 1984 [29] concludes that the DEMs have many abrupt changes in elevation (termed as "Sinks or Voids") in neighboring cells which pronounces errors in the computation of flow direction. In this study 'sink' has been filed before computing flow direction. ArcGIS uses a sink fill algorithm developed by Jensen and Domingue 1988 [144].

Since the beginning, researchers have been arguing on D8 method and its weakness in flat terrains. In the year 1991, Moore and Grayson [145] noted that D8 method permits flow movement over a two-dimensional pixel which is treated as a point, and it is projected down the slope of a one-dimensional line. Once again in 1991, Fairfield and Leymarie [146] indicated the limitation arising from the discretization of flow using D8 method and said that it is due to consideration of flow into only one of eight possible directions, separated by 45°. After that, many flow direction computation methods are invented in the past [30–32,147,148], but each one is rejected due to serious practical concerns except D8 method.

Thus, it is realized that the researchers tried to advance the D8 method, but due to the failure of other methods, it is continuously being used in ESRI GIS as well as in Arc Hydro [149]. Therefore, the present study is carried out with this conventional method to predict uncertainty in river network alignment, basin area delineation and their relation to DEM resolution and morphological characteristics.

4.1.2 Data Used and Methodology

4.1.2.1 Data Used

Details of the dataset used in the study are presented in Table 4.1. The river network digitized over Google Earth has been termed as Google Earth River network while, catchment boundary digitized from the Ganga flood control commission (GFCC) map, the government of India 02/04/2012 is termed as GFCC boundary. Both Google Earth River network and GFCC boundary have been used as referenced data in this study. The general location of the study site, Digital Elevation Model (DEM) along with stream network and sub-basins are given in the Figure 4.1.

Table 4.1: Description of data used in the study

Name of Data	**Type**	**Source**
SRTM DEM 90 m	Raster	CGIAR
SRTM DEM 30 m	Raster	USGS
ASTER DEM 30 m	Raster	http://demex.cr.usgs.gov/DEMEX/
Reference River network	Vector	Digitized from Google Earth Imagery (Referenced river network)
Reference catchment area	Vector	Digitized basin area from map prepared by the Ganga flood control commission (Government of India 02/04/2012)

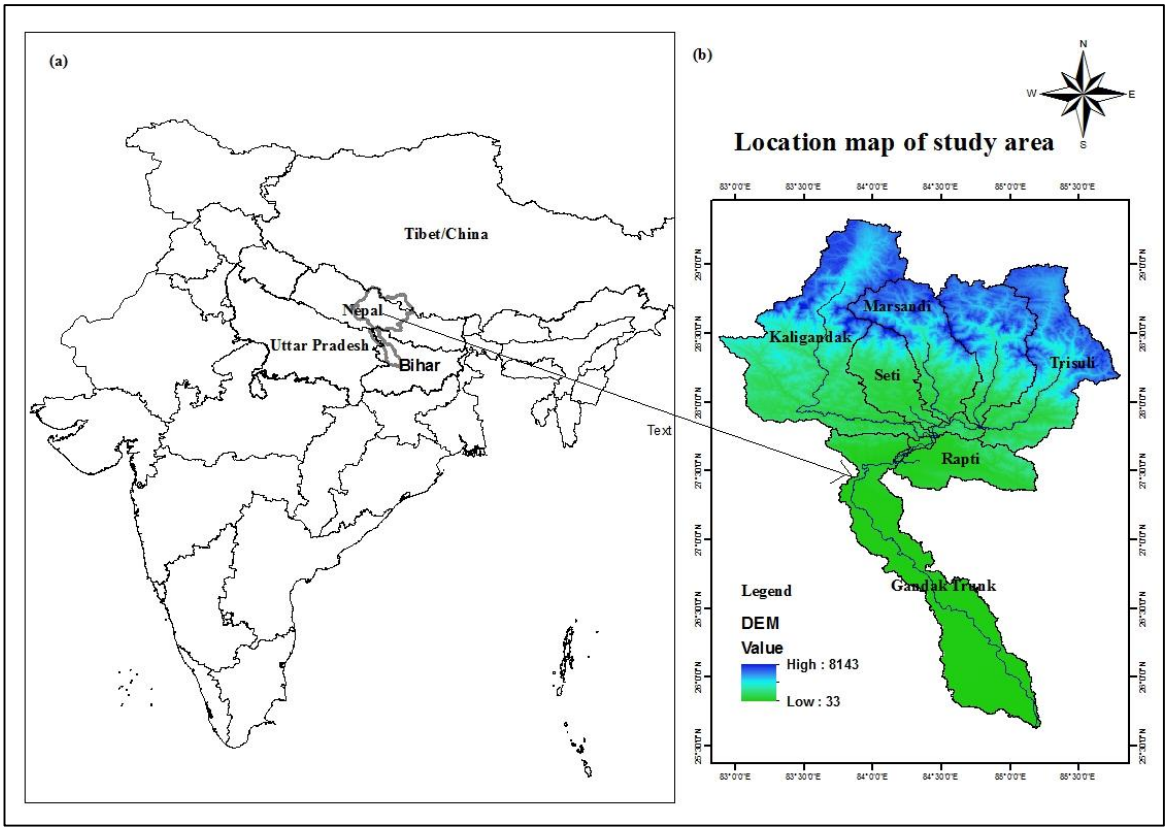

Figure 4.1(a): Location map (b) Digital Elevation Model (DEM) map and sub-basin map of trans-boundary Gandak River basin

4.1.2.2 Methodology

In this study, two different error types are examined.

(a) Error in basin area delineation using automatic delineation with DEMs and
(b) Error in River network alignment using automatic delineation and their relation to morphological characteristics of the basin.

The assessment of (a) is evaluated with three parameters viz. overestimated area, underestimated area and total error (sum of overestimate and underestimate). The GFCC boundary area is compared with the automatically digitized boundary area from SRTM 90m, SRTM 30m, and ASTER 30m. The overestimated area is that lying outside the GFCC boundary, whereas underestimated area is the area which shortfall within the GFCC boundary.

If P is the catchment that is to be assessed (catchment area automatically derived with SRTM90m, SRTM 30m, and ASTER 30m) and Q is the referenced catchment (GFCC boundary area), then the overestimated and underestimated area can be calculated using equation (4.1) and equation (4.2) respectively as:

$$\text{The overestimated area} = P - P \cap Q \tag{4.1}$$

$$\text{The underestimated area} = Q - P \cap Q \tag{4.2}$$

Where $P \cap Q$ is the intersection of catchment area under assessment (P) and referenced catchment area (Q). The overestimated and underestimated area can be summed to provide the total error which is the absolute error in the automatic catchment area delineation. This method allows us to differentiate between two catchment boundaries that encircle equal areas having different shapes and positions by estimating overestimate and underestimate area.

In the assessment of error in river network alignment (b), the two statistical parameters: mean absolute error (MAE) and standard deviation (SD) are used. The stream network for each sub-catchment and all the three DEMs SRTM 90m, SRTM 30m and ASTER 30m are delineated using hydrology tool inbuilt in Spatial Analyst extension of ArcGIS 10.2. The steps are mosaicking of different tiles, masking, sinks fill and finding flow direction, estimation of flow accumulation raster, watershed delineation and then streamline extraction. The downloaded DEM tiles had been mosaicked to a single tile.

Unnecessary area hampers processing time, therefore, mosaicked tile are masked to reduce the area up to the approximate basin area. All the DEMs have some sink (cell having no data) which may cause an error in the analysis. The sink cell values are filled with the sink fill operation by taking the average pixel value of neighboring cells. The adjacent cell towards which water moves after falling over the terrain is the flow direction, whereas the flow accumulation is the accumulated flow weight of all heading towards each downslope cell in the output raster.

The flow direction cell is calculated by using the traditional D8 method which selects single flow direction among eight neighboring cells and is the most popular method for deriving contributing areas, although it is not able to simulate the flow dispersion. The D8 method sums the accumulated area of the neighbor cell with the highest distance weight drop. This neighbor is called the cell downstream of the center cell. The D8 method identifies a neighboring cell based on the steepest gradient for assigning flow direction for that particular cell [144]. More explicitly, it usually assigns to each DEM point, one of eight principal directions (N, NE, E, SE, S, SW, W and NW). In these directions, the method selects one downstream cell called cell downstream of the Centre cell based on the highest distance weight drop i.e. steepest slope. This cell downstream of the Centre cell indicates the direction of flow. If there are no downstream neighbor and the point is not on the edge of the DEM, it gives a value indicating a sink. The ESRI flow direction grid (D8) is an integer raster, where values shown in Figure 4.2 represent the flow direction from the center cell.

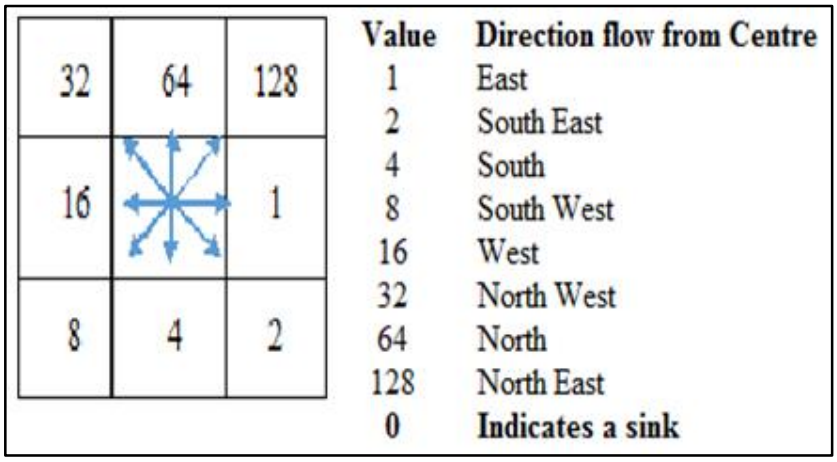

Value	Direction flow from Centre
1	East
2	South East
4	South
8	South West
16	West
32	North West
64	North
128	North East
0	**Indicates a sink**

Figure 4.2: Raster values represent flow direction from the center

.

Flow accumulation is calculated as highest flow accumulated in the cell from neighboring cells [150]. The Stream order is defined using Strahler's classification [151]. The flow diagram of the steps involved in the drainage network delineation is shown in Figure 4.3.

The automatically delineated drainage network from the three types of DEMs is then compared with the referenced drainage network. The study also evaluates the effect of catchment parameters like slope, bifurcation ratio and drainage density on error parameters. Their description are presented in Table 4.2. The distance between automatically delineated river network and the Google Earth river network is measured in some equal intervals of 1 Km using the measure tool of ArcGIS 10.2.1 in all sub-catchments.

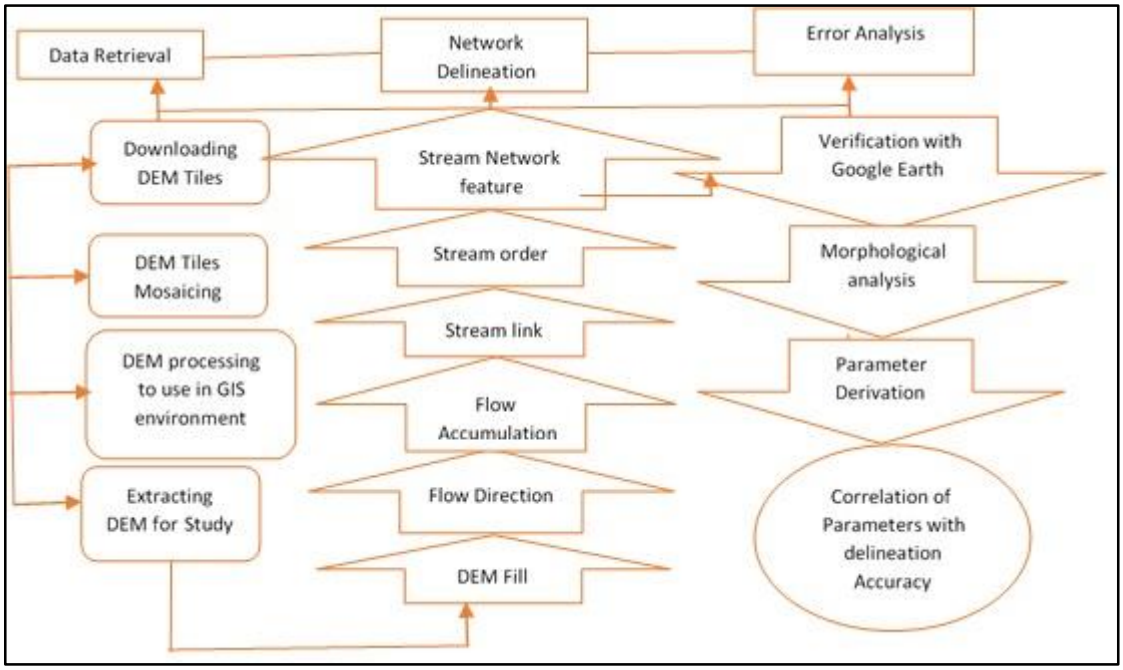

Figure 4.3: Flow chart of the methodology adopted for delineation of Stream Network using different DEMs

Table 4.2: Description of the morphological parameters

Parameter	Description	Remark
Slope (S)	$S = \frac{\text{Drop}(\Delta h)}{\text{Main strean lenght } L_m}$ Δh = Elevation of remote pixel minus elevation of outlet pixel.	The average slope of the main channel for each sub-basin, where the length of the main channel has been considered >= 8 order.
Bifurcation Ratio (R_b)	$R_b = \frac{N_u}{N_{u+1}}$ Where, N_u = Number of streams of order u. N_{u+1}= Number of stream of higher order.	Bifurcation ratio for all order stream had been calculated and then average of was used as Basin's Bifurcation ratio.
Drainage density (D_d)	$D_d = \frac{\sum_{i=1}^{w}\sum_{j=1}^{N} L_{ij}}{A}$ Where, i = 1,w is the number of stream orders. $\sum_{j=1}^{N} L_{ij}$ = sum of streams of order i A= drainage area of the basin N=stream order	D_d has been calculated for each sub-basin.

The measured distance between automatically delineated river network and referenced river network is the alignment error. It may be either positive or negative depending upon whether the automatically delineated river network is on the right side or left the side of the referenced river network when moving from outlet to remote point. The mean absolute error (MAE) and standard deviation (SD) are computed for the calculation of the quantitative error in network alignment. MAE is preferred because absolute error measures are less dominated by a small number of large errors (Rahman et al., 2010), and thus, it is a more reliable indicator for the typical error magnitudes. MAE and SD are calculated using equation (4.3) and equation (4.4) respectively as:

$$MAE = \sum | O(x_i y_i) - D(x_i y_i) | \tag{4.3}$$

$$SD = \sqrt{\frac{\sum_{i}^{n} \left(O(x_i y_i) - \overline{O(x_i y_i)} \right)^2}{n}} \tag{4.4}$$

where,

$O(x_i, y_i)$ is the location of the Google Earth River network alignment at the rate of i^{th} interval, $D(x_i, y_i)$ the location of automatically delineated river alignment at the rate of i^{th} interval and n is the total number of intervals.

4.1.3 Results and Discussion

Figure 4.4 clearly shows that the automatically delineated basin boundaries are unable to pick the GFCC boundary area perfectly. Although, it is not possible to repeat the basin boundary perfectly for different DEMs using automatic delineation. Nevertheless, the error should not be high that may hamper further hydrological and hydraulic analysis. Delineation error for the higher resolution DEMs SRTM 30m and ASTER 30m is significant than lower resolution DEM SRTM 90m. It means higher resolution DEMs fail to calculate the flow accumulated areas correctly. The error is pronounced in flat areas for higher resolution DEM than the low-resolution DEMs. The Higher resolution DEMs are overestimating the boundary area in the flat regions. The lower resolution DEM SRTM 90m delineates the boundary closer to the referenced GFCC boundary. In the high altitudes automatically delineated basin boundary tries to underestimate for all the three DEMs. Among the all three

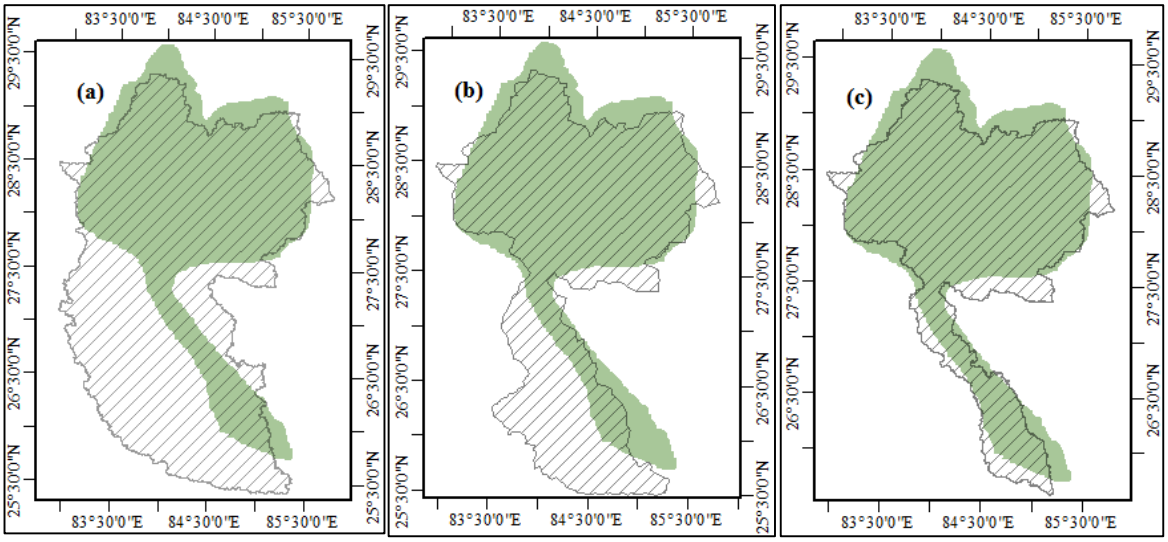

Figure 4.4: The delineation error between automatically extracted area from DEMs (a) ASTER 30m, (b) SRTM 30m and (c) SRTM 90m with the area digitized from Ganga Flood Control Commission (GFCC-green color) map

DEMs, SRTM 90m derived basin boundary is in good agreement with the referenced GFCC basin boundary.

Results presented in Table 4.3 show the maximum overestimated boundary area for ASTER 30m DEM that is 33053.33 km^2. Therefore during quantification of discharge, it may pretend high volume of the basin flow. The maximum underestimated basin area of 9272.44 km^2 is noticed in SRTM 30m DEM and therefore, it may pretend less amount of basin flow. The highest total error in basin area delineation is observed in ASTER 30m i.e. 39137.20 km^2.

Drainage networks are the essential hydrological input, which is being used in various distributed hydrological models like MGB-IPH [an acronym from the Portuguese MGB (Large basin Model) and IPH (Institute of Hydraulic Research)] [138]. Therefore, it is vital to highlight the error in digital network delineation due to different resolution DEMs. Rahman et.al. 2010 [11] has described the limitation of SRTM90m on flat areas of the Ganges. The method for alignment error analysis described in methodology section has been adopted to evaluate the performance of SRTM 90m, SRTM 30m and ASTER 30m in the Gandak River basin. The drainage networks for all the DEMs are automatically delineated through the commonly used D8 method which has been used in different distributed hydrology model such as SWAT, PIHM and MGB-IPH. All the automatically delineated river networks are then overlaid with referenced Google Earth River network as shown in Figure 4.5. It shows a significant deviation between automatically delineated river networks and referenced Google Earth River network. The range of variation is less on steep catchment region than the flat one.

Table 4.3: Results for error in basin area delineation

Delineation method	Total Area (km^2)	Overestimate (km^2)	Underestimate (km^2)	Total error (km^2)
Manually Digitized From GFCC (Referenced basin boundary area)	47146.94	0.00	0.00	0.00
Automatic From SRTM90 m	44796.78	5445.03	7794.25	13239.28
Automatic from SRTM30 m	55208.36	17334.80	9272.44	26607.24
Automatic from ASTER30 m	74115.46	33053.33	6083.87	39137.20

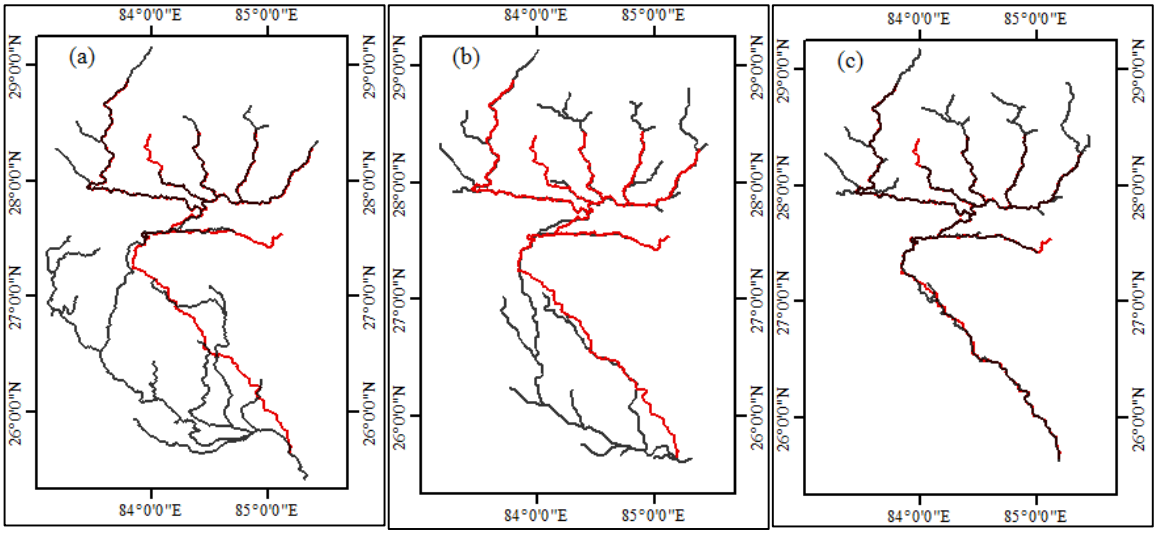

Figure 4.5: Comparison of delineated river network (a) ASTER 30m, (b) SRTM 30m and (c) SRTM 90m with Google Earth image extracted River network (red color)

The morphological parameters, namely the bifurcation ratio (Rb), drainage density (Dd) and channel slope (S) are extracted for each six sub-catchment and the results are presented in Table 4.4. The morphological parameters are the only basis for basin shape and the river network. Therefore, a comprehensive analysis has been carried out to assess the relation between these parameters and the stream network deviation. The slope is calculated by the head difference between the remote pixel and the outlet pixel divided by the length of river run. Among the all six sub-catchments of the Gandak River basin, Budhi Gandak has the steepest channel slope (1:41 mm^{-1}), whereas the GTR is found to be most flat (1:3632 mm^{-1}). The bifurcation ratio for all sub- basins varies from 3 to 5 whereas the drainage density was found between 0.78 to 1.03 km km^{-2}. High drainage density denotes quick peaked and highly eroded basin. Since the Seti sub-catchment has maximum drainage density, its level may rise quickly with mud during the monsoon. Among these morphological parameters, slope shows a definite relationship between the error parameters MAE and SD. The relation of the slope with MAE and SD have been presented in Figure 4.6.

Table 4.4: Morphological parameters of the sub- basins

Sub-Basin/ River Name	**Drainage Area (Sq.Km)**	**Reach Length of SO*@>=8 (m)**	**Elevation (m)**		**Av. Slope of Main River Stream SO* @>=8 (mm^{-1})**	**Drainage density, Dd (Km Km^{-2})**	**Bifurcation ratio Rd**
			Max.	Min.			
Kali Gandak#	11884.517	243000	8143	188	1:69	0.80	2.03
Seti	3133.565	119200	7921	208	1:141	0.78	2.00
Marsandi#	5085.698	139400	8049	233	1:46	0.89	2.16
Budhi Gandak	5000.248	134200	8042	325	1:41	0.83	2.04
Trisuli	6596.503	196400	7362	322	1:51	0.81	2.36
Rapti	3299.220	108600	2577	136	1:375	1.03	2.13
Gandak River # (Trunk, India)	9797.033	352300	1856	33	1:3632	0.87	2.50

*SO Stand for Stream order and #indicates River with dam constructed on it.

Comparison of SD, MAE and slope for all the sub-catchments and for all the three DEMs are presented in Figure 4.6. It reveals that the SD and MAE for SRTM 90m DEM increase with decrease in the steepness of the sub-catchments. This implies that the relative stream alignment deviation increases as the slope decreases. Budhi Gandak has steep slopes and therefore, it has the minimum MAE of 53.21m and SD as 53.01m. GTR has a minimal slope of 1:3090 but it has a maximum deviation of MAE as 993.94m and SD as 1902.129m. In other sub-catchments (Marsandi, Trisuli, Kali, Seti and Rapti) MAE and SD increases with increase in flatness of slope. In the case of another two DEMs; SRTM 30m and ASTER 30m, the effect of slope on the variation of MAE and SD has a random effect. The calculation of SD and MAE is not possible for GTR for the two high-resolution DEMs; SRTM 30m and ASTER 30m due to linear deviation of stream networks more than 9000m. Therefore, the use of these two high-resolution DEMs will not provide the right hydrological results on flat terrains like GTR sub-catchment where the head drop is almost negligible (1m for each 3 km river run).

SD and MAE for the same sub-catchments show a lot of differences between all the three DEMs. This implies that apart from slope, DEM resolution also affects the automatic river network delineation accuracy. The MAE and SD for the ASTER 30m are better than the SRTM 30m and SRTM 90m in the steep slope basins (slope > 1:140) but it does not give good results for flat basins. MAE and SD intercomparison indicates that the river network delineated with higher resolution DEMs has more deviation than lower resolution DEM. A linear trend line between error parameters MAE, SD and slope have been fitted to see the dependency of the delineation error on the gradient of the sub-catchments. The correlation coefficient (R^2) for the linear fit between SD and slope is 0.17, 0.45 and 0.65 for

SRTM 30m, ASTER 30m and SRTM 90m respectively. The higher R^2 value for SRTM 90m DEM indicates the scope to remove the alignment error using a suitable statistical correction algorithm. ASTER 30m DEM shows weaker linear relationship than SRTM 90m as its value is poor and moderate respectively. Therefore, SRTM 30m and ASTER 30m DEMs have less possibility to remove the alignment error using statistical correction algorithms. On the other hand, R^2 for MAE are in quite similar fashion to SD and its values are 0.66, 0.16 and 0.43 for SRTM 90m, SRTM 30m and ASTER 30m respectively

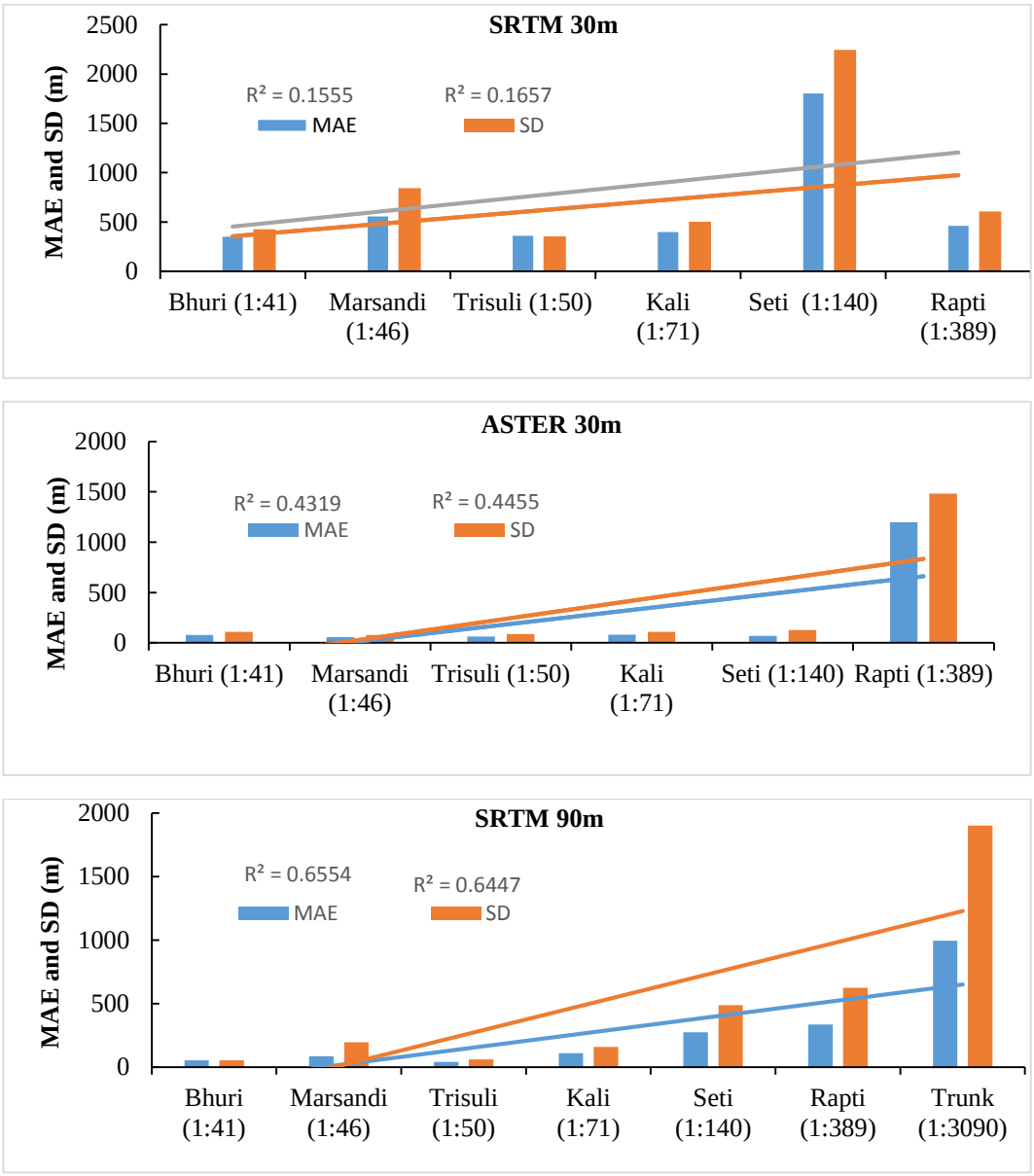

Figure 4.6: Behavior of MAE and SD on the change in slope for three different DEMs

4.1.4 Summary

The study is conducted for seven sub-catchments of Gandak River Basin to evaluate the performance of different DEMs to delineate river networks and basin boundary area. The drainage network and basin area are extracted using the hydrology tool of Spatial Analyst extension in ArcGIS 10.2.1. It is summarized that the flat sub-catchments are having more delineation error for both the stream network and basin boundary area delineation than the steep sub-catchments. Another important point is that automatically delineated boundary has a tendency to overestimate the basin area on the flat regions, whereas it underestimates on the steep slope areas. The work is a way forward because many times people are biased to use high-resolution DEM. The high-resolution DEM is costly than low-resolution DEM and it also takes more computation time, leading to poorer results similar to Han and Hammond 2006 [141].

4.2 Satellite Precipitation: Error in Amount and Frequency

4.2.1 Introduction

Hydrological modelling of watersheds requires continuous and long-term meteorological data. The time series of input data should be at least at a daily time step for climate change and extreme events: flood and drought modelling [152,153]. Precipitation is perhaps the most important input data for these studies. Obtaining reliable input data is a challenge, particularly in developing countries and trans-boundary basins. Currently, the data sharing is quite limited across national boundaries due to economic and national security barriers [154,155]. In this regard, satellite precipitation products can be very useful particularly in trans-boundary basins, where the exchange of precipitation data from rain gauge data does not happen in near real time.

The necessity of reliable satellite precipitation records for extreme events (flood and drought) and climate change has been investigated in numerous error analysis studies worldwide [156–158]. Rain gauge records are the most reliable source of precipitation estimate. However, the spatial distributions of rain gauges and the consistency in the record have certain limitations. High-resolution satellite precipitation products such as TRMM (Tropical Rainfall Measuring Mission) and CMORPH (Climate Prediction Center Morphing Technique) provide considerable improvements in the spatial and temporal variability of the rainfall dataset. Satellite precipitation products are derived using different retrieval algorithms and some products are biased compared to the rain gauge datasets [159]. Therefore, satellite precipitation products must be validated with rain gauge data to estimate their accuracy. The previous assessment of the satellite products has shown considerable agreement against rain gauge precipitation in different parts of the world [160–164].

The Gandak River Basin has very sparse rain gauge station network and rain gauge records have gap in the time series. It may cause difficulty in the simulation of floods in the Gandak River basin. The precipitation pattern is highly variable in space and time in this basin, and almost 90% rainfall occurs during the South Asian Monsoon (June – September). The average annual rainfall varies from 2030 mm in the northern mountainous area to 1100 mm in the southern plains region of the basin (GFCC, 2004)[132].

In the recent past, several studies have been carried out to validate precipitation data from TRMM and other satellite products in the Indian sub-continent. Detailed literature review for validation of satellite rainfall over Indian sub-continent has been presented in Table 4.5. The table shows continuous effort made by researchers to validate the various satellite rainfall products over different zones of the Indian sub-continent such as Nair *et al*. 2009 [68] TRMM 3B42 V6 over western states of India, Bharti and Singh 2015 [165] used TRMM 3B42 V7 over Northern Himalaya, Rahman *et al.* 2012 [161] used TRMM 3B42 V6 and ERA40 in east over Bangladesh, Kneis *et al.* 2014 [158] used TRMM 3B42 and TRMM 3B42RT in Central India over the Mahanadi river basin, Muller and Thompson 2013 [166] used TRMM 3B42 V6 over Nepal, Wu Lu and Zhai Panmao 2012 [162] used TRMM 3B42 V7 and CMORPH over Tibetan Plateau and China, to name a few. The Table 4.5 explicitly highlights the gap in the validation of TRMM 3B42 V7 and CMORPH satellite product over the Southern Himalayas.

This work is an attempt to validate one gauge adjusted satellite precipitation product TRMM 3B42 V7 and one exclusive satellite-based precipitation product CMORPH to see their usefulness for extreme events analysis over Southern Himalayan Gandak River basin. The TRMM 3B42V7 gauge adjusted satellite precipitation has been preferred over other such as PERSIAN or GsMaP because TRMM 3B42V7 algorithm takes special care for mountainous regions using SRTM 30m DEM as an auxiliary data [167]. The PERSIAN and GsMaP retrieval algorithm use meteorological data from ground observations while CMORPH is exclusively satellite-based precipitation product [168–170].

The Gandak River Basin is a trans-boundary basin – the basin area falls in India, China and Nepal (Figure 4.7). The basin consists of some of the highest and most complex terrains having elevations that range from 33 m in the southern plains to the maximum 8143 m in the northern part towards Himalayan Mountains. Rainfall data were collected from 30 rain gauge stations maintained by the Department of Hydrology and Meteorology, Nepal and Indian Meteorological Department (IMD). All 30 rain gauge stations data have analyzed for their consistency using double mass curve method and only six rain gauge stations have been found reliable following this evaluation. The example consistency check (double mass curve graph for Marsharakh) is presented in Figure 4.8. Widely used satellite precipitation products TRMM 3B42 V7 and CMORPH are quantitatively evaluated with rain gauge precipitation at these six rain gauge stations.

Table 4.5: Review for validation of satellite precipitation over the Indian sub-continent

Authors	**Data**	**Region/Country**	**Key findings**
Bharti and Singh, 2015[165]	TRMM 3B42V7	Northern Himalaya, India	*Product does well up to 2000m altitude. *Critical altitude was found at 3100m. *The product has a high magnitude bias at 99.99 percentile That means the product is not good for high rain events
Prakash *et al.* 2015[164]	TRMM 3B42V7 and CPC_RFE 2.0	Whole India	*TRMM product overestimates over the eastern India while underestimates along the west coast. *RFE 2.0 Underestimates over the entire country except eastern India.
Guo *et al.* 2014[171]	CMORPH	Tibet, China	*CMROPH is failing to capture morning peak. *Diurnal cycle in rainfall frequency is basically due to the topography.
Kneis *et al.* 2014[158]	TRMM 3B42 and TRMM 3B42RT	Mahanadi basin, India	*Discrepancies between rain gauge precipitation and TRMM precipitation for higher intensities. *Significant negative bias in TRMM 3B42RT data.
Xue *et al.* 2013[172]	TRMM 3B42 V7 and TRMM 3B42 V6	Wangchu Basin, Bhutan	*3B42 V7 product has improved upon 3B42 V6's underestimation for the entire basin. *A significant improvement in the discharge simulation using 3B43 V7 compared to TRMM3B42 V6.
Muller and Thompson 2013[166]	TRMM3B42 V6	Nepal	*Reported error in the TRMM 3B42 V6 product and proposed a frequency-domain based bias correction.
Krakauer *et al.* 2013[173]	TRMM 3B43, GSMaP, CMORPH, and PERSIANN	Nepal	*Monthly evaluation of these satellite products indicates that TRMM B43 precipitation is promising on others for water resources planning.
Wu Lu and Zhai Panmao 2012 [162]	TRMM 3B42 V7 and CMORPH	Tibetan plateau, China	*The ability to accurately detect rainfall for both the products depends on topography. * TRMM and CMORPH underestimates and overestimates the frequency of lighter rain events, respectively.
Duo *et al.* 2011[174]	CPC_RFE 2.0	Tibet, China	*product performs well with mean CC 0.74, POD 73% and FAR between 1 to 12% except few aspersion towards Himalayan range. *They concluded that the product can be used for flood related studies.
Shrestha *et al.* 2011[175]	CPC_RFE 2.0	Narayani, Himalaya, Nepal	*The product underestimates rain events. *The simulated discharge with CPC_RFE2.0 rainfall underestimated runoff peak by 50%, while, after application of three ratios based bias adjustment, it shows considerable improvement.
Rahman *et al.* 2012[161]	ERA40, TRMM 3B42 V7	Bangladesh	*Three verification methods proposed by Murphy (1993) indicates that both the products perform well and can be used for design flood estimation studies.
Islam *et al.* 2010 [176]	TRMM 3B42 V6	Nepal	*TRMM trends are similar to rain gauge data. *TRMM underestimates the amount with few exception of overestimation.
Nair *et al.* 2009 [68]	TRMM 3B42 V6	Maharashtra, India	* TRMM 3B42 V.6 product found able detect dry and wet monsoon. * Moreover, the timing of Ground-based rain events coincides with the satellite rain events.

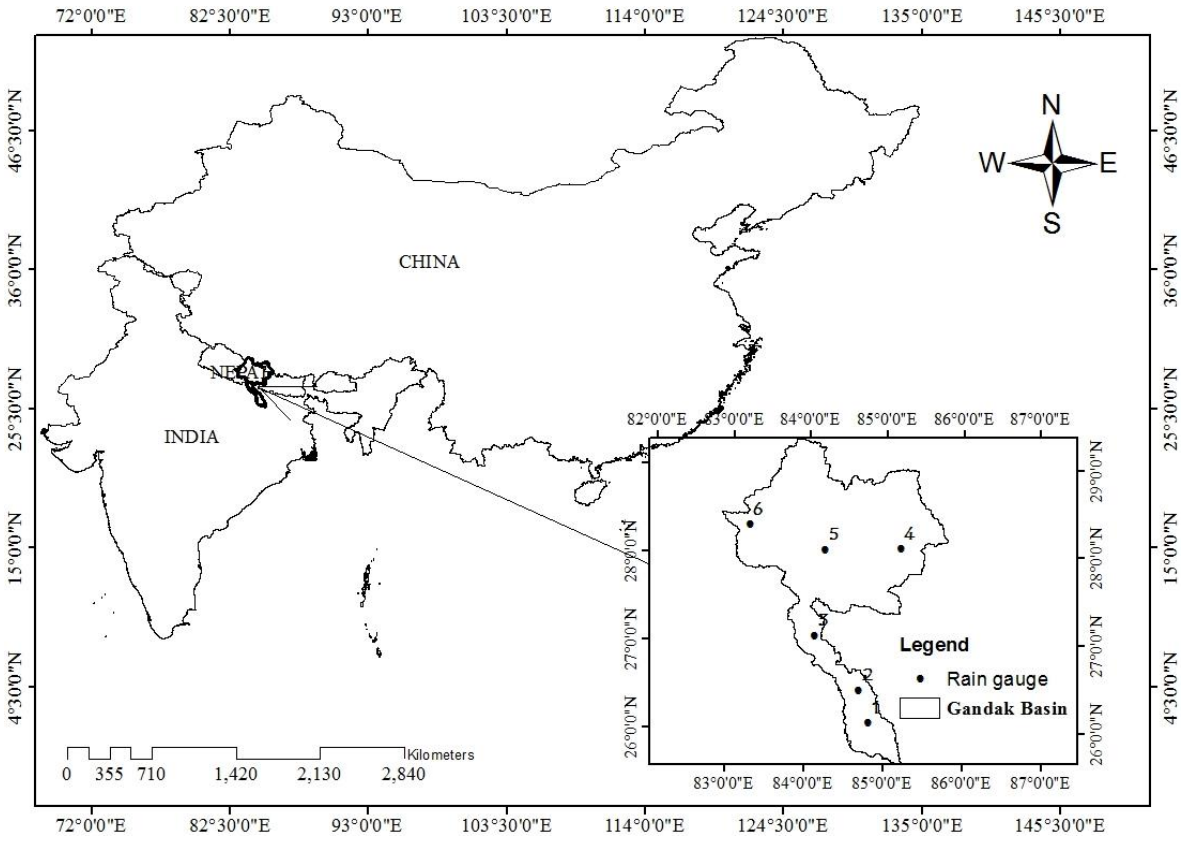

Figure 4.7: Location map of the study area and rain gauge points

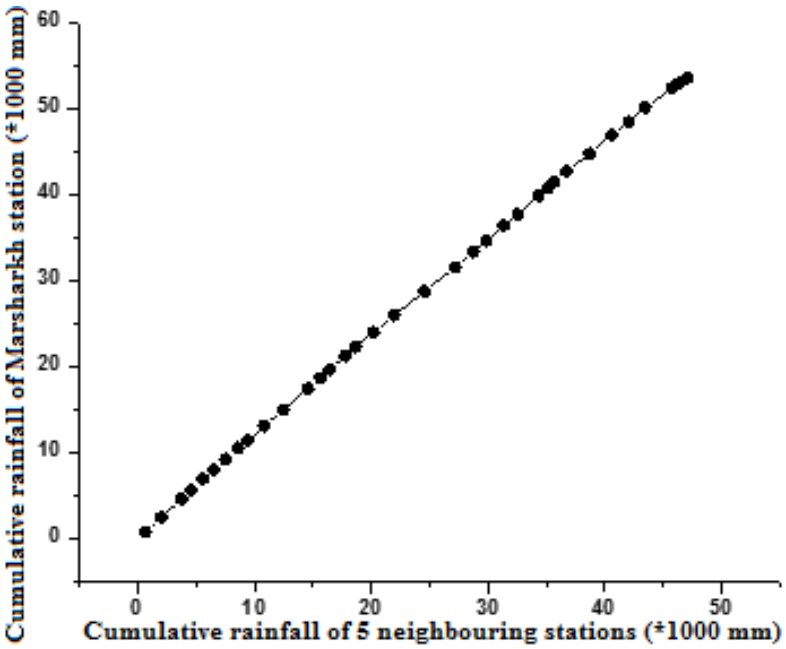

Figure 4.8: Double mass curve of Marsharakh gauge site

The results provide insights into the capability of the satellite precipitation products to detect the frequencies and the amount of precipitation in the complex topography of Gandak river basin. This study may provide the foundation for bias correction in the satellite products over the Southern Himalayan basins.

4.2.2 Data and Methods

4.2.2.1 Satellite Data

TRMM 3B42 V7 and CMORPH precipitation products have been analyzed. The TRMM 3B42 data are available from 1998 to present while CMORPH from 2002 to present. The web address (http://gdata1.sci.gsfc.nasa.gov/daacbin/G3/gui.cgi?instance_id=TRMM_3-Hourly) can be used to download the TRMM data while CMOROPH precipitation data can be downloaded from ftp site (ftp://ftp.cpc.ncep.noaa.gov/precip/global CMORPH/3-hourly 025 deg.).

The TRMM B42 V6 processing algorithm is described in Huffman *et al.* 2007 [177] while changes made in the processing algorithm of TRMM 3B42 V7 are described in Huffman *et al.* 2010 [178] and are summarized here. TRMM 3B42 V7 has a new processing algorithm, Goddard profiling algorithm (GPROF) 2010 for the passive microwave (PMW) based estimation. It uses existing TRMM storm profile records, PMW based brightness

temperature, and precipitation rates and it replaces a reference database created using a cloud model in version 6. Additionally, version 7 also incorporates satellite data from Microwave Humidity Sounder (HMS), Special Sensor Microwave Imager (SSMI) and it also has the capability to ingest new satellite data in the future. A new infrared brightness temperature data is introduced for the period of Climate Prediction Centre (CPC), 4km global IR data (i.e., Januray 1998 to February 2000). Furthermore, a single reprocessed Advanced Microwave Sounding Unit-B (AMSU-B) satellite dataset replaces the previous version for which two dissimilar calibration periods are used, and this removes some of the internal discrepancy existing in TRMM Multi-satellite Precipitation Analysis (TMPA) Version 6. The algorithm also implements a monthly scale gauge bias correction, which uses a reanalysis data (version 6.0) from the Global Precipitation Climatology Centre (GPCC) that includes anomalies instead of amounts and a denser rain gauge network.

TRMM precipitation radar (TPR) estimate is corrected globally and regionally over the mountainous regions that are described in a technical document (TRMM Precipitation Radar Team 2011) [167] and key findings are summarized here. In Version 6, the algorithm is found to be inaccurate over the mountainous regions and is affected by a high level of surface cluster for rain echo. It has also been seen to miss-locate surface echoes because of erroneous elevation data and cover-up by strong signals from intense rainfall. TRMM 3B42 V7 algorithm accounts for elevation data for mountains like the Himalayas and Andes from Shuttle Radar Topography Mission (SRTM 30m). Furthermore, TRMM 3B42 V7 algorithm uses a repeat search algorithm for the surface echo that advances its detection and thus, it determines cluster free rain regions in the entire storm profile.

CMORPH algorithm produces a very high temporal and spatial resolution precipitation data with near total global coverage. This technique uses rainfall estimates *exclusively* derived from low orbit satellite microwave observations [170] and whose features are transported using spatial propagation information that is obtained entirely from geostationary satellite infrared (IR) sensors. At present CMORPH incorporates precipitation estimates derived from passive microwave sensors onboard 14 and 15 (SSMI), 16, 17 and 18 (AMSU-B), NOAA-15, DMSP 13, AMSR-E and TMI aboard NASA Aqua and TRMM spacecraft. The technique is extremely flexible to incorporate precipitation estimates from any microwave satellite sensors.

Infrared (IR) sensors data are used as a medium to propagate the microwave-derived precipitation features when microwave data are not available at a particular spatial location. Propagation vector matrices are produced by computing spatial lag correlations between successive images from geostationary satellite IR and this is used to propagate the microwave-derived precipitation estimates. This process governs the movement of the precipitation features only. At a particular location, the shape, and intensity of the precipitation features in the following half-hour periods between microwave scans are acquired by executing a time-weighting interpolation between microwave-derived features that have been propagated forward in time from the preceding microwave observation and those have been propagated backward in time from the succeeding microwave scan. This is referred to this second step as "morphing" of the features. The essential details of the dataset used in this work are presented in Table 4.6.

Table 4.6: Detail description of the precipitation datasets used in this study

Dataset		Temporal Resolution	Spatial Resolution	Description of the data	Comment
Rain Gauge data	IMD	Daily	Irregular	Ground-based 15 station rain gauge data provided by Indian Meteorological Department (IMD) Gov. of India. Strict data acquisition quality. Data is available from 2000-2012.	Data gaps and Inconsistent
	DHM	Daily	Irregular	Ground-based 15 station rain gauge data provided by Department of Hydrology and Meteorology (DHM) Gov. of Nepal. Strict data acquisition quality. Data is available from 2000-2012.	Data gaps and Inconsistent
TRMM 3B42		3 h	Gridded (0.25×0.25)	TRMM 3B42 V7 were derived by algorithm 3B42 (Huffman et al. 2007) and provided by the NASA Goddard Space Flight Center. The data coverage is 50^0S-50^0N and 180^0W-180^0E.	Continuous and Consistent
CMROPH		3 h	Gridded (0.25×0.25)	The data has produced using NOAA's CMROPH, which uses rainfall estimates exclusively derived from low orbit satellite microwave observations (Joyce et al. 2004). The data coverage is 60^0S-60^0N and 180^0W-180^0E	Continuous and Consistent

In this study, Giovani interactive visualization and analysis tool are used that generates daily precipitation from 3 hourly TRMM 3B42 product. The 3-hourly accumulated satellite precipitation estimates of TRMM 3B42 and CMORPH are summed from 6.00 UTC on the previous day to 3.00 UTC of current day to get gauge equivalent daily satellite precipitation corresponding to local time 8:30 AM. An example to derive daily

accumulated satellite precipitation data at a local time from 3 hours accumulated satellite precipitation data are given in Table 4.7.

Table 4.7: Example to create daily accumulated satellite data (in mm) at local time 8:30 AM for 07/06/2005 at Marsharakh

Time(UTC)	**6**	**9**	**12**	**15**	**18**	**21**	**0**	**3**	**Total**
Local time	8:30AM-11:30AM	11:30AM-2:30PM	2:30PM-5:30PM	5:30PM-8:30PM	8:30PM-11:30PM	11:30PM-2:30AM	2:30AM-5:30AM	5:30AM-8:30AM	
CMORPH	0	0	4.87	2.43	0.14	0	0	0	7.44
TRMM	0	0	9.40	5.06	6.90	0.45	0	0	21.81
Rain gauge	-	-	-	-	-	-	-	-	23.2

Gridded TRMM 3B42 and CMORPH daily precipitation are resampled using bilinear weighted interpolation to get the data at specific point locations [65,179]. The algorithm averages four adjacent grids to a point of interest [180]. An illustration for weighted bilinear interpolation is shown in Figure 4.9. In a 2×2 grid, to calculate the interpolated value at position (X, Y), the closer grid will have greater weight. The method not only considers the distance from the pixel, but it also considers a spatially weighted approach dependent on the spatial location [181]. The expression for weighted bilinear interpolation is given as [182].

$$X = S_x X_1 + (1 - S_x) X_2 \tag{4.5}$$

$$S_x = \frac{X - X_1}{X_2 - X_1} \tag{4.6}$$

$$Y = S_y Y_1 + (1 - S_y) Y_2 \tag{4.7}$$

$$S_y = \frac{Y - Y_1}{Y_2 - Y_1} \tag{4.8}$$

Where $0 \leq S \leq 1$, $X_1 \leq X \leq X_2$.

From above, the weight for any arbitrary point (X, Y) in a two dimensional space can be calculated as described by Arnold et al., 2002 [182]

$$\begin{aligned} I(X, Y) = {} & (1 - S_x)(1 - S_y) I(X_1 Y_1) + \\ & S_x (1 - S_y) I(X_2 Y_1) + (1 - S_x) S_y I(X_1 Y_2) + S_x S_y I(X_2 Y_2) \end{aligned} \tag{4.9}$$

where I is the actual pixel value.

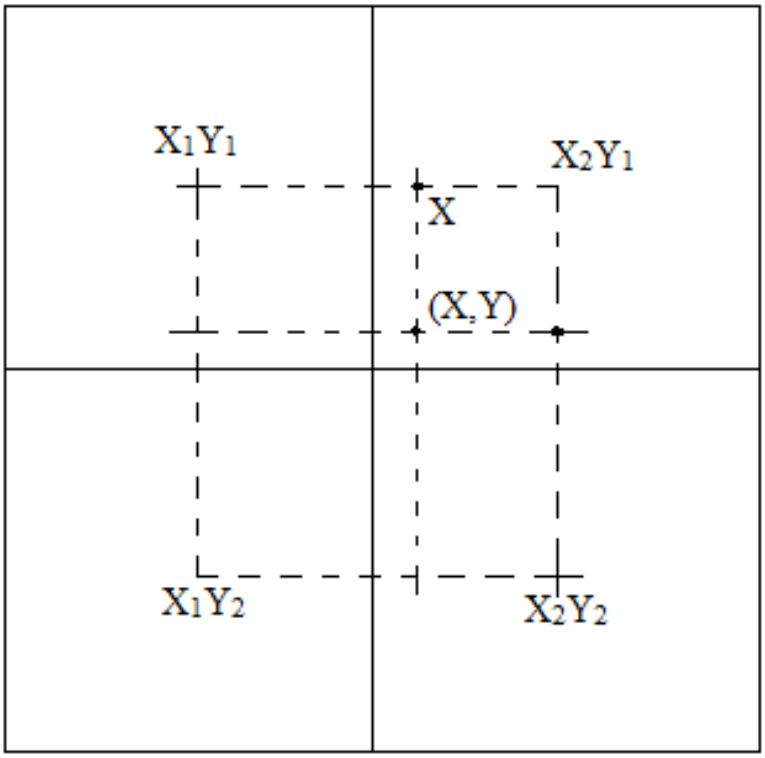

Figure 4.9: A graphical representation of weight estimation on 2×2 grid for bilinear interpolation

4.2.2.2 Gauge Data

Ground-based rain gauge data are available on a daily basis (accumulated over 24 hour period) and, collected/reported at 8.30 AM local time. Thirty gauge station data have been collected from two countries Nepal and India. In which, 15 rain gauge stations are maintained by the Department of Hydrology and Meteorology (DHM), Government of Nepal and other 15 rain gauge stations by the Indian Meteorological Department (IMD), Government of India in the Indian portion of the Gandak River basin.

Rain gauge data collected from IMD and DHM are having numerous gaps. There are many methods to estimate missing precipitation data viz. simple average, normal ratio, linear or multi-regression, inverse distance weighting methods, the coefficient of correlation weighting method (*CCWM*) to name a few. Ramesh *et al.* 2005 concluded that *CCWM* is superior to other methods, and it can provide a better deterministic estimation of missing data in any climate region. *CCWM* (Equation 4.10 and 4.11) are used to estimate the missing data in the time series.

$$P_m = \frac{\sum_{i=1}^{n} P_i \left(r_{mi}\right)^K}{\sum_{i}^{n} \left(r_{mi}\right)^K} \tag{4.10}$$

$$r_{mi} = \frac{Cov(P_i P_m)}{\sigma_{P_i} \sigma_{P_m}} \tag{4.11}$$

where, P_m is the missing precipitation at station m, P_i the precipitation at the i^{th} station, r_{mi} the correlation coefficient between station m and i and K the exponent that can be optimized for the particular case.

A thorough study has been conducted to check the consistency and continuity of the dataset from each station. The consistency check was done with double mass curve method while the length of missing data at each site was considered for the continuity test. An example to verify the consistency of time series for a station namely Marsharakh is given in Figure 4.8. After a detailed study, I found only six rain gauge stations are consistent in the study area. These rain gauges are shown in Figure 4.7 and are: 1.Marsharakh (India), 2.Chatiya (India), 3.Bagaha (India), 4.Kuncha (Nepal), 5.Thamachit (Nepal) and 6.Baghara (Nepal).

4.2.2.3 Validation Methods

In this study, TRMM 3B42 and CMORPH precipitation data for monsoon season, J-June, J-July, A-August and S-September (JJAS) from 2005-2010 are evaluated with daily rain gauge data.

Murphy (1993) [183] described three types of "goodness" to verify satellite precipitation estimates viz. consistency, quality and value. Wilks (2006, 2011))[184,185] defined a partial list of scalar attributes of forecast qualities: accuracy, bias, reliability, resolution, discrimination and sharpness. Stanski *et al.* 1989 [186] divided verification of forecast into visual, dichotomous (categorical variable verification), and continuous variable verification categories. I used forecast/satellite verification categories proposed by Stanski *et al.* 1989 [186] to verify TRMM and CMORPH satellite precipitation estimate in this study.

Visual Verification

In visual verification, I examine the difference between the satellite estimates and observed rain gauge values. Visual verification is an instantaneous judgement to distinguish the error between the satellite estimates and rain gauge precipitation. Peoples have often used exploratory graph techniques such as time series plot, histogram, and Cumulative Distribution Function (CDF) referring to the use of visual verification.

Yes/ no-Dichotomous

The yes/no dichotomous verification (categorical variable verification) is based on the statistic to quantify the scalar attribute of the forecast [185]. In this method, 'yes' describes that an event will happen and 'no', the event will not happen. A threshold may be set to distinguish 'yes' and 'no' event in the rainfall (1, 2, 5, 10, 20, 50 mm d^{-1}) as per the time scale of the dataset WMO/TD-No.1485 (2008). Wu Lu *et al.* 2012 [162] described a threshold 0.1mm day^{-1} i.e. equivalent to the minimum rain gauge observation. This is a low threshold and will be able to distinguish the 'yes' and 'no' event of light rain. In this study, a threshold of 0.1mm day^{-1} have also been applied to distinguish the rain events. Brown *et al.* 1997 [187] provided a contingency table for the query of 'yes' and 'no' estimation and it is presented in Table 4.8.

Table 4.8: Contingency table for yes/ no dichotomous between daily Gauge and satellite precipitation

		Gauge estimate (G)		
		Yes	No	Total
Satellite estimate(S)	Yes	a Hit	b False Alarm	a+b Satellite observed Yes
	No	c Miss	d Correct negative	c+d Satellite observed No
Total		a+c Gauge observed Yes	b+d Gauge observed No	N Total

From the contingency table, four combinations of chance can be possible between rain gauge and satellite observations. These are listed below.

(i) Hit: both gauge and satellite event occur

(ii) Miss: Gauge event occurs, but satellite event does not occur

(iii) False Alarm: Gauge event does not occur, but satellite event occurs

(iv) Null or Correct Negative: both events do not occur

Based on these dichotomous a variety of statistics are developed by Wilks (2006) [185] and WMO/TD-No.1485[188] for validation of satellite observations. The statistical parameters used in this study are described below (meaning of notations a, b, c and d are given in Table 4.8).

Bias Score:

$$B = \frac{a+b}{a+c} = \frac{\text{Satellite observed events}}{\text{Gauge observed events}} \tag{4.12}$$

The Bias score depends on marginal only, it does not measure correspondence. B =1, indicate unbiased estimation whereas B<1 and B>1 indicates under estimation and over estimation respectively.

Probability of detection (Hit rate):

$$POD_{rain} = \frac{a}{a+c} = \frac{\text{Hits}}{\text{Gauge observed events}} \tag{4.13}$$

$$POD_{no\ rain} = \frac{d}{b+d} = \frac{\text{Correct negative}}{\text{Non Gauge observed events}} \tag{4.14}$$

It measures the fraction of all gauge events correctly observed by the satellite events. The best *POD* score is 1, but the occurrence of the best *POD* score does not mean that satellite precipitation is equivalent to gauge precipitation.

False alarm Ratio:

$$FAR_{rain} = \frac{b}{a+b} = \frac{\text{False alarms}}{\text{Satellite observed events}} \tag{4.15}$$

$$FAR_{no\ rain} = \frac{c}{c+d} = \frac{\text{Miss}}{\text{Non Satellite observed events}} \tag{4.16}$$

False alarm ratio is the fraction between false alarms to the total number of satellite observed events. The value varies from $0 \leq FAR \leq 1$. The best score is zero, but the best score of *FAR* does not mean perfect satellite observation.

Probability of false alarm detection (false alarm rate):

$$\mathrm{POFD} = \frac{\mathrm{b}}{\mathrm{b}+\mathrm{d}} = \frac{\text{False alarms}}{\text{Non Gauge observed events}} \tag{4.17}$$

This is the ratio between the False alarms to the Non gauge observed events. The value varies from $0 \leq POFD \leq 1$ and the best score is *POFD* equals to zero.

Accuracy (fraction correct):

$$\mathrm{ACC} = \frac{\mathrm{a}+\mathrm{d}}{\mathrm{N}} = \frac{\text{Correct satellite events}}{\text{All satellite events}} \tag{4.18}$$

This is the fraction of all satellite events that are correct. The *ACC* value ranges from $0 \leq ACC \leq 1$ and the best score is 1. The best score of *ACC* means a perfect match of gauge precipitation by satellite precipitation.

Threat score (Critical Success Index):

$$\mathrm{TS} = \mathrm{CSI} = \frac{\text{Hits}}{\text{All satellite or Gauge events}} \tag{4.19}$$

TS or CSI is the fraction between hits to all satellite or Gauge events. The value varies from $0 \leq TS \leq 1$ and the best score is 1. The best score indicates perfect detection.

Skill score:

$$\mathrm{SS} = \frac{\mathrm{A} - \mathrm{A}_{\mathrm{ref}}}{\mathrm{A}_{\mathrm{perf}} - \mathrm{A}_{\mathrm{ref}}} \tag{4.20}$$

where, *A* is accuracy score, e.g., *ACC* or *TS*, $\mathrm{A}_{\mathrm{perf}}$ accuracy of perfect forecast i.e. 1. A_{ref} accuracy of reference forecast and that can be calculated as

$$\mathrm{A}_{\mathrm{ref}} = \left(\frac{(\mathrm{a}+\mathrm{b})}{\mathrm{N}}\right) * \left(\frac{(\mathrm{a}+\mathrm{c})}{\mathrm{N}}\right) + \left(\frac{(\mathrm{d}+\mathrm{c})}{\mathrm{N}}\right) * \left(\frac{(\mathrm{d}+\mathrm{b})}{\mathrm{N}}\right) \tag{4.21}$$

SS=1 indicates perfect detection of Gauge precipitation by satellite precipitation. *SS*>0 indicates skillful, better than reference, whereas *SS*<0 indicates less skillful lower than reference detection.

Continuous variable verification

The verification of continuous variables measures how the value of satellite estimates differs with the value of gauge observations. This can be done by various summary scores described below

Bias (mean error, systematic error):

There can be two types of bias viz. 1) Mean error (additive bias), which describes the error between the mean of satellite ($\overline{S}$) and mean of rain gauge estimate ($\overline{G}$). The mean error may be (-Ve) or (+Ve) based on the underestimation and overestimation of records. And 2) Systematic error (multiplicative bias) is the ratio between $\overline{S}$ and $\overline{G}$. The best score of systematic error is one. The equation is given as:

$$B_{add} = \left(\overline{S} - \overline{G}\right), B_{mult} = \frac{\overline{S}}{\overline{G}} \tag{4.22}$$

Mean absolute error:

Mean absolute error measures the absolute deviation of satellite precipitation from gauge precipitation. The formula is given as:

$$MAE = \frac{1}{N}\sum_{i}\left|S_i - G_i\right| \tag{4.23}$$

Mean squared error (MSE), root MSE (RMSE):

$$MSE = \frac{1}{N}\sum_{i}\left(S_i - G_i\right)^2, RMSE = \sqrt{MSE} \tag{4.24}$$

This statistical parameter is sensitive to outlier and favors satellite estimates to avoid large deviation from the mean.

Correlation coefficient:

This statistics measures the random error (scatter around the best fit) and can be formulated as below

$$CC = \frac{Cov\left(S_i, G_i\right)}{\sigma_S \sigma_G} \tag{4.25}$$

where $Cov(S_i, G_i)$ is the co- variation between Gauge and satellite data and σ_S, σ_G are the variance of satellite and gauge data respectively. The range varies from $-1 \leq CC \leq 1$ and the best score is 1.

4.2.3 Result and Discussions

Three satellite data verification methods described by Stanski *et al.* 1989 [186] viz. visual verification, dichotomous verification, and continuous variable verification have been discussed in section 4.2.2.3. These methods are applied to analyze the satellite products at six rain gauge locations from 2005-2010 for monsoon months (JJAS). The results are discussed in this section.

4.2.3.1 Visual Verification

Figure 4.10 shows the scatter plot comparison between six-year daily average satellite and rain gauge rainfall at the six stations. The stations are given here in ascending order of elevation from mean sea level (a) Marsharakh 62m, (b) Chatiya 70m, (c) Bagaha 93m, (d) Kuncha 725m, (e) Thamachit 1942m, and (f) Baghara 2659m. TRMM daily average precipitation overestimates the amount (Duncan and Biggs 2012, Bharti and Singh 2015) for low rain events (intensities $\leq$ 7 mm d^{-1}) at all stations. Furthermore, for medium rain events (7 mm $d^{-1} \geq$ event intensity $\leq$15 mm d^{-1}), either it is close to the rain gauge data or overestimates the amount at the first four stations (elevation $\leq$ 2000m) but for rest two stations (elevation $\geq$2000m) it underestimates amount apparently. TRMM underestimates the amount for high rainfall events (intensities $\geq$ 15 mm d^{-1}) at all stations. On the other hand, CMORPH is reliable only for very low rain events (intensities $\leq$ 5 mm d^{-1}) and in the plain areas (elevation $\leq$ 1000m). CMORPH underestimates amount whose intensities are $\geq$ 5 mm d^{-1} at all rain gauge stations.

Figure 4.11 is the bar diagram representation of monthly satellite and rain gauge precipitation. It shows that the monthly precipitation value of CMORPH is much lower than the gauge rainfall for all stations. On the other hand, TRMM rainfall is comparable to the gauge rainfall for first four rain gauge stations (elevation $\leq$ 2000m) whereas, for rest two, it underestimates.

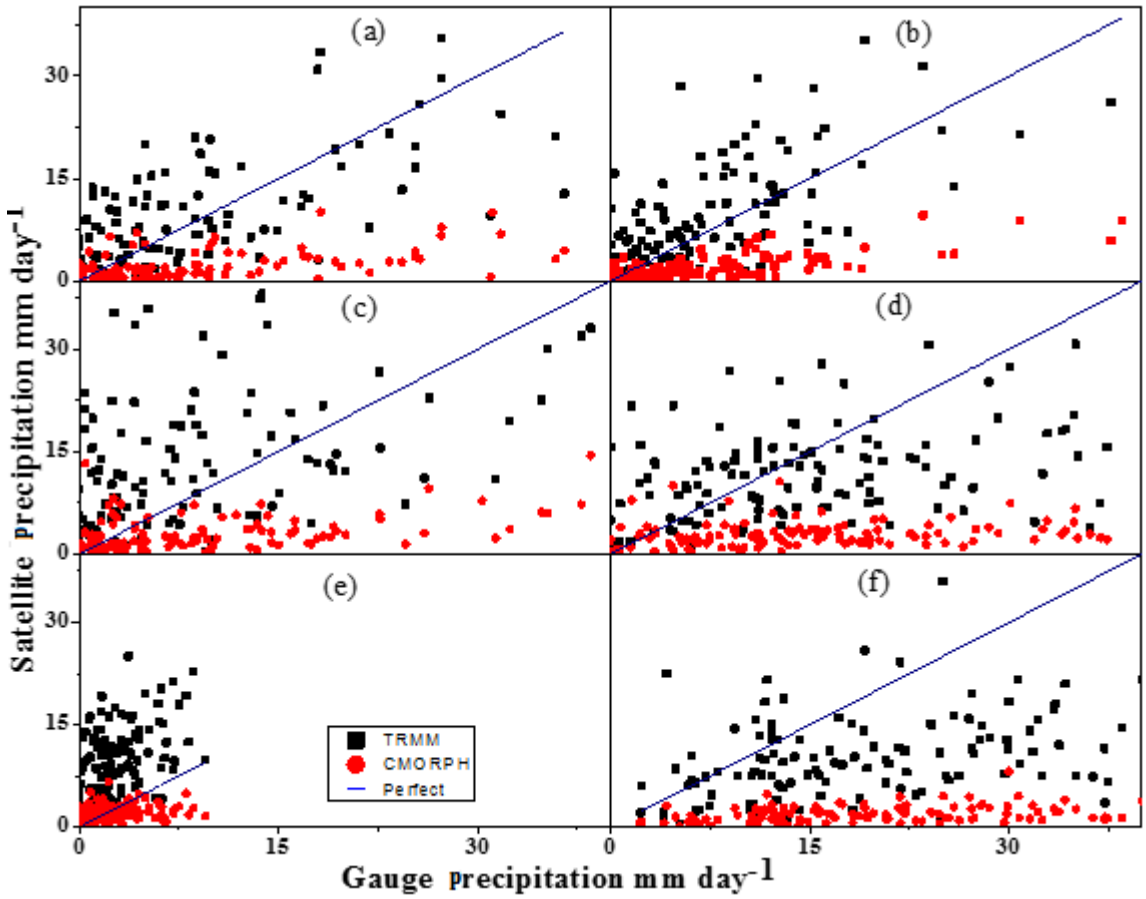

Figure 4.10: Scatter plot of the TRMM and CMOROH with daily Gauge data at various rain gauge sites

The precipitation intensities can be categorized either by fixed quantity of precipitation which occurs in a 24hour period or by the percentile of daily precipitation amounts. Here, in Figure 4.12, grouped satellite precipitation along with the gauge precipitation in various intensity classes to construct a histogram of relative frequency. This figure shows that almost 75% rain events are in class 0-10 mm day^{-1} that means only 25% rain events have rain intensity ≥ 10 mm d^{-1}. In the frequency class 0-10 mm day^{-1}, TRMM reproduces the rain events better with little underestimation whereas, CMORPH overestimates the relative frequency in this class that means CMORPH may have high false alarms for low-intensity rain events. Furthermore, in the class intervals ≥ 10 mm d^{-1} TRMM overestimates the relative frequency for first three plain stations (elevation ≤ 1000m) and for the rest three (elevation ≥ 1000m) it underestimates the rainfall relative frequency. It means TRMM may produce a false alarm of the high-intensity rain events in the plain areas whereas it may miss at high altitudes. On the other hand, CMORPH is completely failing to capture the relative frequency in the class intervals having intensity ≥ 10 mm d^{-1} for all stations.

Figure 4.13 shows the Cumulative Distribution Function (CDF) plot between the satellite and rain gauge data. CDF shape of TRMM estimates nearly matches to rain gauge CDF for first three stations (elevation ≤ 1000m) but it estimates lower for the rest three stations (elevation ≥ 1000m). This implies that TRMM underestimates the probability of occurrence of rain events for high altitudes i.e. TRMM may miss high-intensity rainfall events. On the other hand, CDF plot of CMORPH is above to CDF plot of rain gauge data. It means CMORPH has a greater probability of producing a false alarm for all rainfall events at all stations.

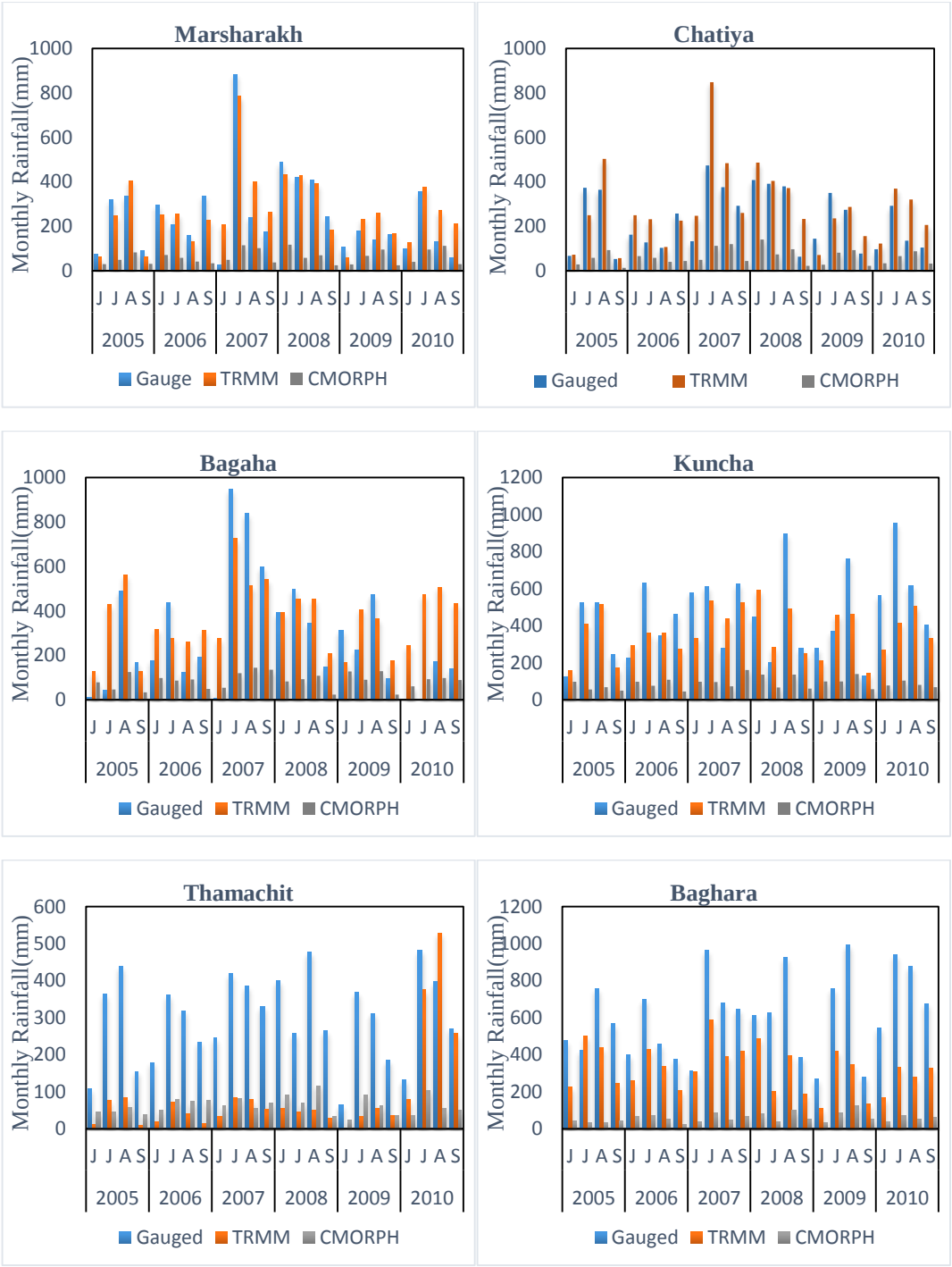

Figure 4.11: Monthly time series plot of TRMM, CMORPH and Gauge data for monsoon months (JJAS, 2005-2010)

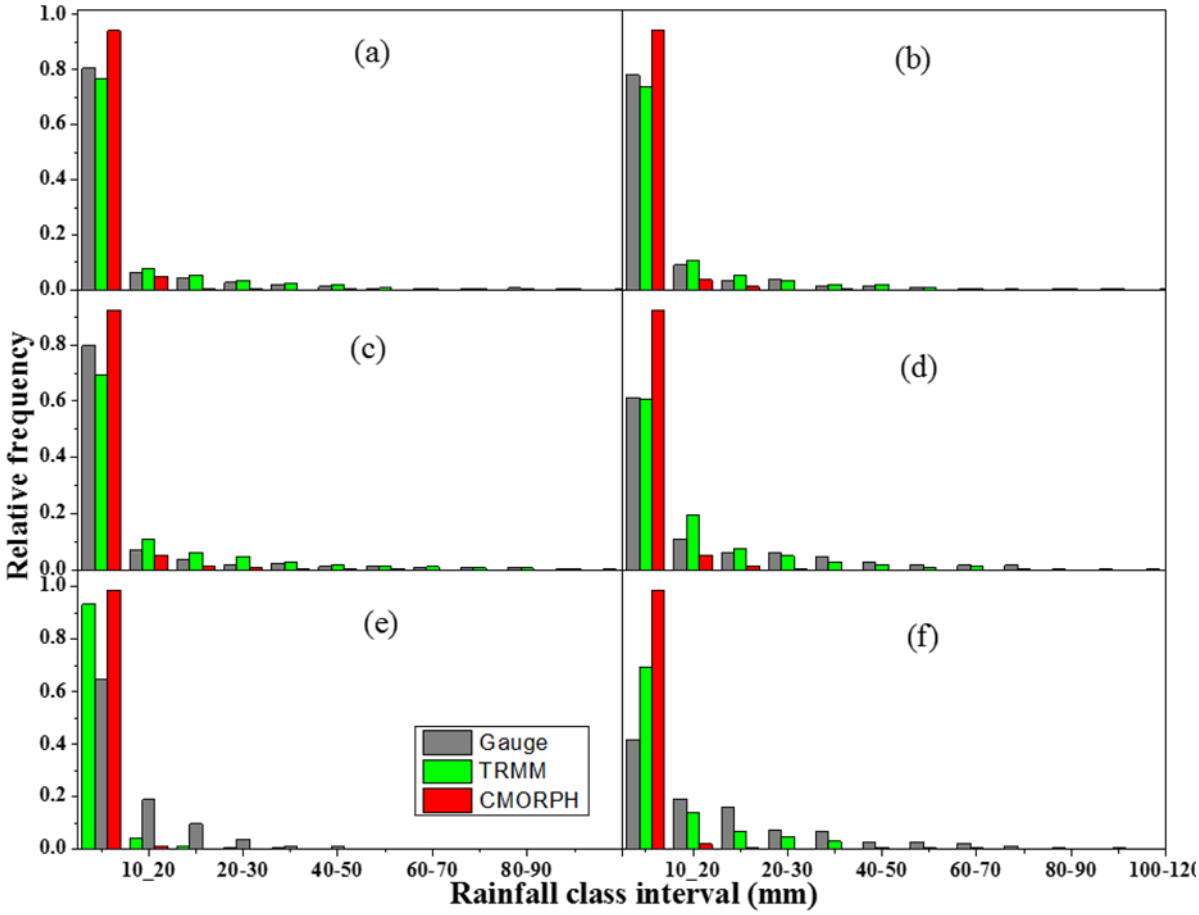

Figure 4.12: Histogram of relative frequency of daily TRMM, CMORPH and Gauge data (for JJAS, 2005-2010) at different rain gauge stations

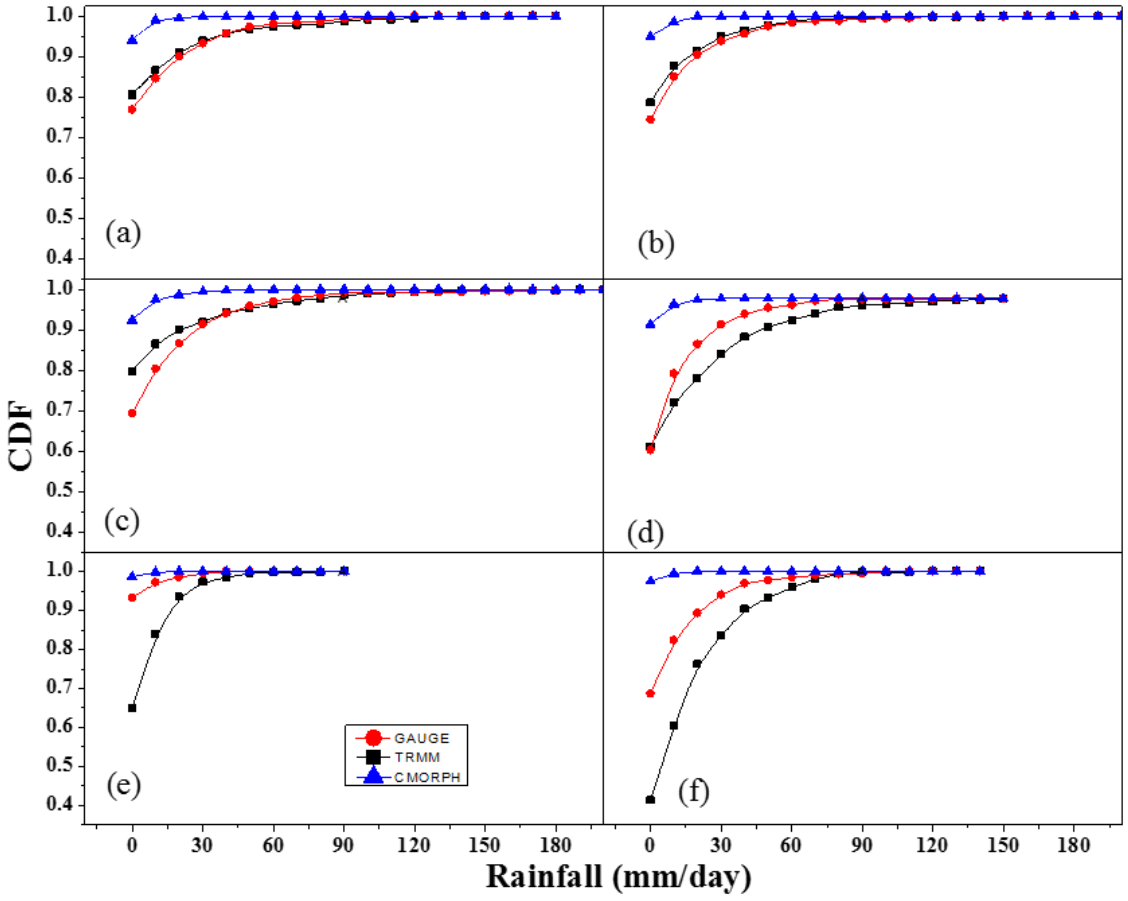

Figure 4.13: Cumulative distribution functions (CDFs) between daily TRMM, CMORPH and Gauge data at different rain gauge stations

4.2.3.2 Yes/ no-Dichotomous

Yes/No-dichotomous statistics described in Section 4.2.2.3, determines how well the satellite estimates can detect rain events and their frequencies. The results presented in Table 4.9, exhibit that the reliability of satellite-based precipitation is strongly dependent on topography.

Table 4.9: Yes/no dichotomous validation statistics of daily satellite precipitation products relative to gauge data

STN	Data	yes/no dichotomous								
		Bias	PODrain	PODno rain	FARrain	FARno rain	POFD	Acc.	TS	SS
Marsharakh	TRMM	1.66	0.80	0.62	0.5	0.11	0.38	0.69	0.45	0.38
	CMORPH	1.72	0.85	0.61	0.5	0.1	0.39	0.68	0.46	0.38
Chatiya	TRMM	1.34	0.84	0.63	0.37	0.16	0.37	0.73	0.56	0.46
	CMORPH	1.34	0.83	0.61	0.38	0.18	0.39	0.7	0.55	0.42
Bagaha	TRMM	1.59	0.9	0.59	0.43	0.09	0.41	0.71	0.53	0.44
	CMORPH	1.62	0.9	0.57	0.44	0.1	0.43	0.69	0.52	0.45
Kuncha	TRMM	1.8	0.95	0.23	0.47	0.17	0.77	0.60	0.51	0.20
	CMORPH	1.75	0.93	0.26	0.47	0.2	0.74	0.58	0.51	0.18
Thamachit	TRMM	1.5	0.95	0.16	0.37	0.32	0.84	0.64	0.61	0.2
	CMROPH	1.55	0.94	0.07	0.39	0.54	0.93	0.6	0.59	0.02
Baghara	TRMM	0.99	0.88	0.47	0.11	0.55	0.53	0.81	0.79	0.35
	CMROPH	0.93	0.82	0.45	0.12	0.66	0.55	0.76	0.74	0.24

Bias score is ≥1 at all stations for both the satellite estimates, except at Baghara rain gauge where it is 0.93 and 0.99 for CMORPH and TRMM respectively. This implies that both satellites measures overestimate the number of rain events. POD_{rain} is more than 0.80 always; it indicates that both the satellite product can probably detect the rainy events more than 80% cases at all stations. The $POD_{no\ rain}$ is considerable (almost 60%) for both satellites in the plain stations (elevation ≤ 1000m) but it falls to 16% for stations in the zone of elevation≥1000m from the M.S.L. It means both satellite products are poor in detection of no rain events at the higher altitudes that may result in false alarms in these areas. FAR_{rain} for both satellites ranges between 0.11-0.50. TRMM and CMORPH both show higher false alarm ratio towards the plain areas. On the other hand, $FAR_{no\ rain}$ results are opposite to FAR_{rain}. $FAR_{no\ rain}$ is maximum 0.66 for CMORPH at most elevated place Baghara, whereas minimum 0.10 at low elevated place Marsharakh. TRMM has relative better $FAR_{no\ rain}$ 0.55 that means TRMM better reveals the no rain events towards high elevated areas.

The POFD analysis shows that TRMM estimates are better than CMORPH in plains but poorly performs in elevated stations. The minimum PODF is 0.37 for TRMM at Chatiya

while maximum 0.93 for CMORPH at Thamachit. The Accuracy of TRMM ranges from 0.81 to 0.60 whereas for CMORPH it is 0.76 to 0.59 (a perfect accuracy score is 1). Thus, both satellite estimates have a minimum 0.19 in accuracy. The lower value of TS score towards plains shows more asymmetry between rain events and non-rain events. The SS score is more than 0 for both satellites at all stations which indicates skilful detection by both the satellite products. The SS score range for TRMM estimates is 0.47 to 0.2 while for CMORPH it is 0.45 to 0.02 which means that CMORPH does not perform well.

4.2.3.3 Continuous Variable Verification

The continuous variable verification statistics is basically to quantify the differences in the amount of satellite and rain gauge precipitation. These statistics are the mean absolute error (MAE); root mean square error (RMSE), correlation coefficient (CC), bias additive (Mean error) and bias multiplicative (Systematic error). Results of the continuous variable verification are presented in Table 4.10

Table 4.10: Continuous variable verification method statistics of daily satellite precipitation products relative to Gauge data

STN	**Data**	**Continuous Variable Verification method**				
		MAE (mm)	RMSE (mm)	CC	Mean error	Systematic error
Marsharakh	TRMM	8.16	17.79	0.72	0.82	1.1
	CMROPH	7.45	19.87	0.41	-5.99	0.25
Chatiya	TRMM	7.63	15.97	0.71	1.75	1.23
	CMROPH	6.66	16.06	0.58	-5.49	0.27
Bagaha	TRMM	10.84	22.59	0.75	2.63	1.28
	CMROPH	8.56	22.21	0.56	-6.48	0.3
Kuncha	TRMM	15.07	25.35	0.55	-3.14	0.79
	CMROPH	14.74	27.53	0.29	-12.2	0.19
Thamachit	TRMM	8.67	13.98	0.25	-6.87	3.38
	CMROPH	3.18	16.17	0.1	-0.84	0.71
Baghara	TRMM	16.21	24.35	0.5	-9.43	0.53
	CMROPH	18.43	27.11	0.33	-18.08	0.1

.

MAE value ranges from 7.63-16.21 for TRMM whereas it vary from 6.66-18.43 for CMORPH. TRMM and CMORPH both has minimum MAE 6.63 and 6.66 respectively, at Chatiya, in the plain area. On the other hand, TRMM and CMORPH both shows maximum MAE of 16.21 and 18.43 respectively at Baghara in the elevated area. RMSE values indicate quite a similar perception as MAE. It ranges from 13.98-27.11 for TRMM and 16.06-27.53 for CMORPH. The CC values are in the range of 0.25-0.75 and 0.10-0.58 for TRMM and CMORPH respectively. TRMM indicates +ve mean error of 0.82, 1.75, 2.63, at first three plain stations (Elevation $\leq$ 1000m), whereas –ve of -3.14, -6.87, -9.43 for rest three elevated

stations (elevation ≥1000m). On the other hand, CMORPH indicates –ve for mean error at all the rain gauge stations. The +ve of mean error indicates an overestimation of rainfall amount by satellite estimates whereas –ve an underestimation. The systematic error indicates >1 and <1 values for TRMM, at first three plain stations and another three elevated stations respectively whereas <1 for CMORPH for all stations. The systematic error value >1 and <1 indicates overestimation and underestimation of rain amount respectively. Thus, the results of mean error and systematic error indicate that TRMM overestimates the rain amount in the plain areas whereas underestimates towards mountains. On the other hand, both systematic error and mean error indicates that CMORPH clearly underestimates the rain amount either in plain or in mountain. The statistics of continuous variable verification, RMSE, MAE, CC and two types of error mean and systematic indicate that CMORPH is associated with more quantitative error compared to TRMM.

Figure 4.14 shows that the CC between satellite and gauge data is sensitive to the elevation. Correlation coefficient follows the decreasing trend with an increase in elevation. The gradient of a decreasing trend for both the satellite TRMM and CMORPH is same as 0.0001 but it differs in intercept as 0.67 and 0.45 for TRMM and CMORPH respectively. To examine the significance of decreasing trend of correlation coefficient with elevation, a hypothesis testing method t-test is performed. The t-test statistics of TRMM shows that $\mathbf{t}_{calculated}$ (-ve, 5.439) > $t_{critical}$ (1.792) at 95 % level of significance. On the other hand, CMORPH has $\mathbf{t}_{calculated}$ (-ve, 4.1545)> $t_{critical}$ (1.792) at 95% level of significance. This implies that the correlation coefficient is negatively significant with elevation at 95% level of significance for both CMORPH and TRMM. R^2 value for TRMM is 0.61 and 0.49 for CMORPH. The higher value of R^2 for TRMM indicates better linear fit and thus it can be more easily bias adjusted than CMORPH. Figure 4.15 compares the spatial variation of the correlation coefficient of TRMM and CMORPH with elevation. It clearly shows the more error in the mountains as indicated by lower CC. When two CC map have been compare one by one, it shows that TRMM and CMORPH have maximum CC of 0.75 and 0.58 and minimum 0.25 and 0.10 respectively. Thus, spatial correlation coefficient map show better prediction of rain amount by TRMM than CMORPH over the entire basin.

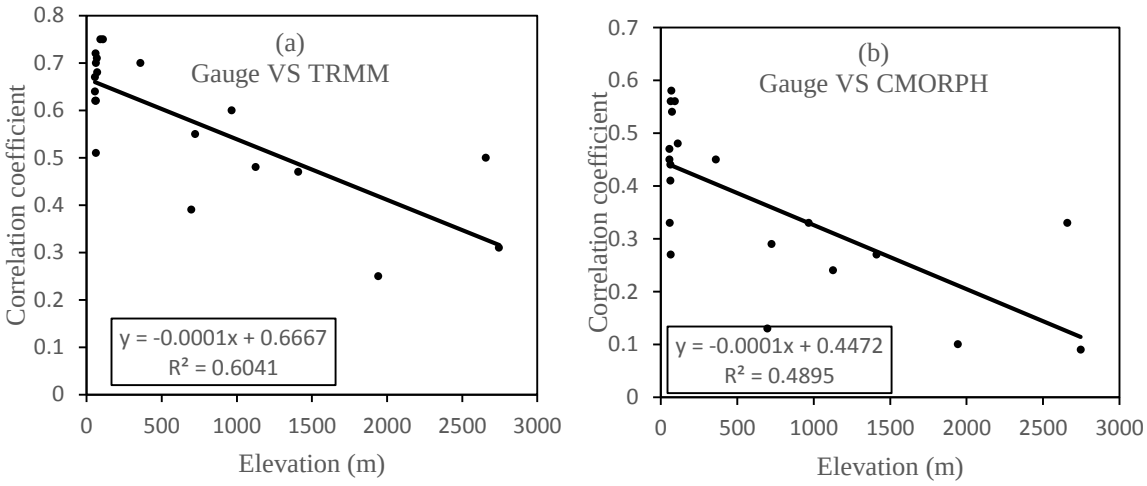

Figure 4.14: Elevation versus correlation coefficient (CC) diagram between (a) daily gauge versus TRMM (b) daily Gauge versus CMORPH for all the rain gauge stations

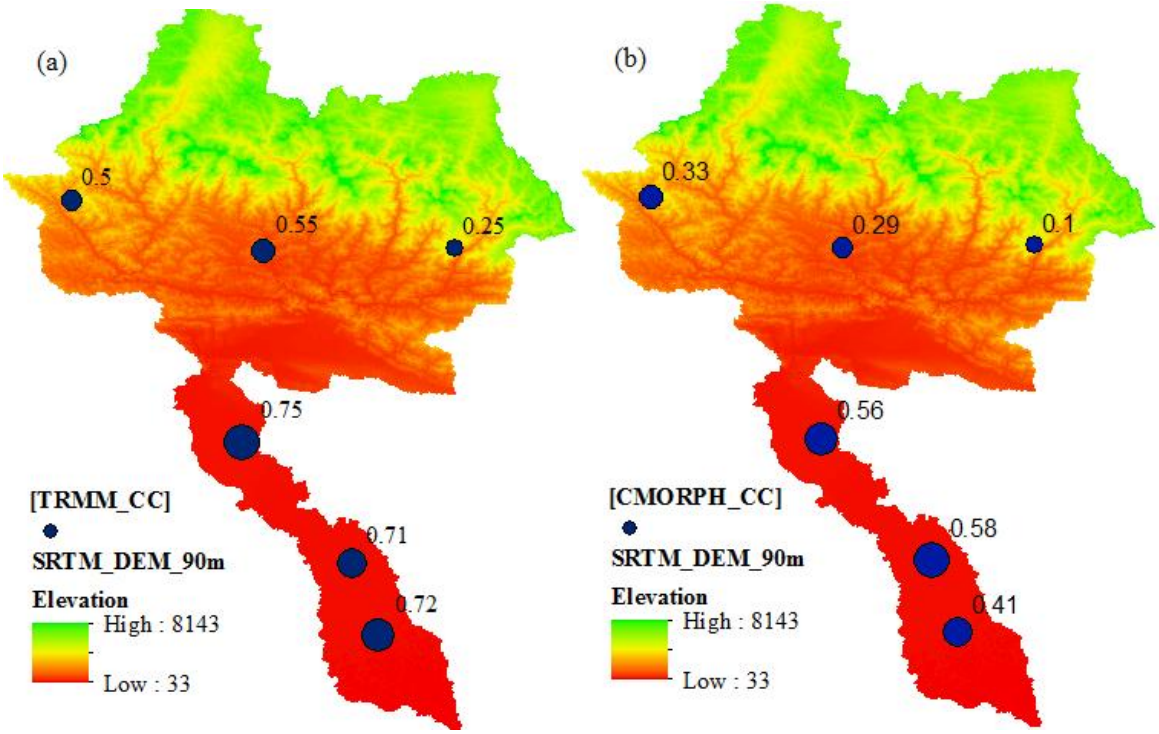

Figure 4.15: Graduated bubble map of correlation coefficient (CC) between daily Gauge data and (a) TRMM (b) CMORPH over the DEM of study area for all six rain gauge stations

4.2.4 Summary

Management of extreme events (flood and drought) are critical to reduce the vulnerability. Accurate rainfall is the key to predict the streamflow for extreme events using hydrological models. Availability of station based gauge rainfall data is limited due to the trans-boundary problem, complexity in climate and topography within the study area. Two satellite precipitation products viz. TRMM 3B42 V7 and CMORPH are validated with the available six rain gauge station data. The validation period is from 2005-2010 for Monsoon period (JJAS). Based on the statistical discussion, following points has been summarized-

- The reliability of daily satellite precipitation products is dependent on the topography of the basin. Both the products were able to differentiate days with precipitation and days without precipitation but gauge adjusted TRMM 3B42 V7 product is found more accurate than exclusively satellite-based precipitation product CMORPH.
- TRMM daily average precipitation overestimates the rain amount for low rain intensities over the entire area, whereas it underestimates the rain amount for high rain intensities over the high altitude mountainous areas. CMORPH does well for low-intensity rain events but it underestimates the rain amount for high rain intensities over the entire area.
- TRMM captures the frequency of rain events for low-intensity while CMORPH overestimates the frequency of low intense rain events. On the other hand, TRMM overestimates the frequency of high intensity rain events over the plain area and underestimates over mountains.
- Satellite estimates generally overestimate the rain events. TRMM and CMORPH are found to be reliable to detect “rainy events” with more than 80% accuracy for plain area while it does detect “no rain days” in the mountainous areas.
- The correlation coefficient between rain gauge and satellite precipitation decreases with increase in altitude and it is found that it is negatively significant for *t*-test hypothesis testing method at 95% level of significance.

- The error between satellite and rain gauge precipitation strongly depends on the change in elevation, so it is recommended to incorporate it as a parameter in bias adjustment.

It has been summarized that the satellite precipitation products should be used after the bias adjustment over the high altitudes. The gauge adjusted TRMM 3B42V7 product can be used for extreme event analysis such as flood frequency analysis and drought monitoring in mountainous Himalayan basins with caution.

Chapter 5

Uncertainty due to Change in Spatial Inputs

Digital Elevation Model (DEM) is a key spatial input in distributed hydrological modeling. At times, the grid size of DEM needs to be altered for hydrological simulation in large basins and this may induce uncertainty in the model outputs. In this study an attempt has been made to analyze the impact of different DEM resolution (grid size) and resampling methods on the SWAT outputs.

5.1 Introduction

The greater Himalayan region known as the "roof of the world" is significantly impacted by human-induced anthropogenesis [189,190]. It is the most critical issue in this region, threatening human health [191,192], food supply and natural ecosystem [193–196]. Therefore, Himalayas should be protected from climate change and human activities [197]. Simulation of Hydrology and Nonpoint Sources Pollutants (H/NPSP) is an occurrence with various possibilities in this direction and therefore, it has become a prime field of research worldwide. Physically based models are very useful to estimate H/NPSP [40,46,49] in a watershed and have been effectively used in environmental risk management [44,47,198].

To better manage the risk, the uncertainties causing errors in the model results should be understood [199,200]. In the recent past, considerable progress has been made to measure and model uncertainty [200,201]. The efficiency of physically based models significantly depends on the input data to predict H/NPSP [39,41,44,202]. Therefore, it should be selected with caution [203]. Although higher resolution spatial input data improves the simulated outputs, results should be interpreted with caution to ascertain optimum input resolution. [204]. Researchers have also pointed out that the higher resolution spatial input data may not be able to improve the performance of hydrological modeling spatially in larger catchments [205,206].

For the large basins, researchers are interested in quickening the hydrological simulations and at times, hydrological models use specific grid size input data. In such conditions, researchers need to alter the grid size of spatial inputs using resampling methods. Digital Elevation Model (DEM) is one such key spatial input for the hydrological models. Hydrological models like Soil and Water Assessment Tool (SWAT) use DEM as the basic input to derive various topographic and watershed characteristics viz. watershed and sub-watershed boundary, slope, channel network, flow direction, flow accumulation and many others [38,46,48]. The flow geometry charateristics are dependent on DEM resolution. For example, the coarser-resolution DEM may result in the decrease in the slope, which directly impacts the delineation of the stream network, the sub-basin and ultimately the number of the Hydrological Response Units (HRUs) [206,207].

Himalayan River basins are covered with snow throughout the year. Therefore, Himalayan Rivers receive an ample amount of snowmelt in the flow volume. The elevation effect has been seen in the physical characteristics of the snow, like snow distribution [208], snow depth [209], and snow cover dynamics [210] in this area. The temperature and the pressure change with the altitude, which affect the freezing and melting of snow. However it also influences the formation of the stable isotope for the precipitated water over the mountains [211]. There are basically two types of the snowmelt model: 1) Energy balance based snowmelt model like Utah Energy Balance (UEB) [212] and 2) Conceptual Temperature index or degree-day method based models like SWAT [213]. Snowmelt models use DEM elevation data in the computation of snowmelt and snowpack formation processes. Therefore, appropriate DEM resolution is very crucial for the snowmelt models [212].

Missing *in-situ* snow cover information for the Himalayas hamper energy balance based runoff studies [214]. Temperature index or degree-day models have outperformed energy balance models on a catchment scale [215,216]. However, limitations have been highlighted for decreasing accuracy with increase in the temporal resolution and incompetence to model spatial variability due to topographic effects [215]. In some extent, Temperature index model with elevation bands [217,218] has overcome the later said limitation. Moreover, the topographic variables have an apparent effect on climatic controls in the Himalayas [219,220]. Simple temperature index snow-melt model uses degree-day factor for ice and snow, gradient of air temperature and precipitation. These are varying

significantly with elevation for the complex Himalayan terrain [221–227]. Therefore, a suitable DEM grid size needs to be investigated for hydrological simulations in this region.

Table 5.1: The chronological review report of the uncertainties in SWAT model outputs with DEM source, grid size and resampling methods

n	Publication	Country	Area km^2	Altitude range (m)	Source and input scenarios	Key findings
1.	[39]	USA (IA)	21.8	264-312	12 DEMs scenarios from 20 to 500m based on the topographic survey by USDA.	-The upper limit of DEM size to simulate watershed loads is 50m. -Coarse grid size DEM does not affects runoff simulation but significantly affects nutrients and sediment at annual time step.
2.	[40]	USA (AR)	18.9	<30	7 DEMs scenarios from 30 to 1000m based on 1:2400 scale map of USGS.	-The DEM grid size ranges 100-200m achieve <10% error in the SWAT outputs at annual time step. -Coarse grid size DEMs have decreased flow and NO_3, but it is not always valid for P
3.	[41]	USA (FL)	855	4-51	9 DEMs scenarios based on source (30m, 90m, 300m) and their resampled DEM.	-Flow is sensitive to both DEM resolution and resampling and therefore it can't be ignored for the distributed watershed models.
4.	[198]	China	4426	200-2605	4 DEMs scenarios from 30 to 200m based on bilinear resampled ASTER GDEM.	-The study revealed that a level of threshold for GIS data exists and that should be determined to get optimum model results.
5.	[44]	China	81.7	713.4±235.5	11 DEMs scenarios from 5 to 140m based on bilinear interpolated SRTM and ASTER DEM.	-SWAT prediction for nitrogen and phosphorous decreases significantly with coarser resampled resolution. -SRTM performs better than ASTER for annual SWAT simulations.
6.	[46]	China	2995	110-3088	17 DEMs scenarios from 30 to 1000m resampled from 30m ASTER DEM using nearest neighbor interpolation.	-The optimal DEM resolution for flow is 30-200m, for sediment 30-100m, for TN 30-150m, for TP 30-100m, NH_4–N 30-70m and for dissolved oxygen and NO_3-N 30-300m.
7.	[49]	Malaysia	1652	6-989	22 DEMs scenario created from 20 to 1500m using ASTER, SRTM, EarthENV and GMTED DEMs and four resampling methods	-Relative error (RE) is less than 7% from 20 to 50m and from 100 to 800m. -RE is lowest for ASTER flowed by SRTM, EarthENV, and GMTED.

In the recent past, a continuous effort has been made by many researchers to demonstrate the influence of DEM grid size, source, and resampling methods on the model outputs in a variety of topographic and climatic regions [46,49,198]. A chronological review report related to uncertainties in the SWAT model outputs due to DEM source, grid size and resampling methods is given in the Table 5.1. The chronological review report (Table 5.1) shows that in all previous studies to ascertain the uncertainties, SWAT model outputs are carried out for small and low relief watersheds. To the best of our knowledge, no study has been conducted in the large mountainous glacier river basins like Himalayan River basins [228]. Neither has there been research conducted with the high-resolution temporal outputs [46]. So, it is legitimate to carry out the DEMs based uncertainty analysis of H/ NPSP with special emphasis on river basins having snowmelt contribution in the flow.

5.2 Data and Methodology

5.2.1 Data Used

The input spatial data used for this study are DEM (SRTM 90m v4.1), soil map (FAO) and land use map (GlobeLand30). The meteorological data are collected from Climate Forecast System Reanalysis (CFSR) [229] and precipitation from APHRODITE (Asian Precipitation High-Resolution Observational Data Integrated Towards Evaluation) [230]. The land use data (for the year 2010) has been collected from China's global land cover mapping (GlobeLand30). CFSR meteorological data include minimum and maximum temperature, relative humidity, wind speed and sunshine hours. Thirteen years of observed discharge data (2000-2012) at the Triveni site have been obtained from the Central Water Commission (CWC) government of India. The other details regarding the input data are presented in Table 5.2. The general location of selected stream gauge point and Digital Elevation Map (DEM) for the study site is given in the Figure 5.1

The SRTM 90m [231] is a joint project between the United States National Aeronautics and Space Administration (NASA), National Imagery and Mapping Agency (NIMA), and the German and Italian space agency. The SRTM mission (February 2000) covers almost 80% of the globe between 60N to 56S. To study the impact of DEM grid size and the resampling methods, the forty-eight scenarios [sixteen DEMs of grid size (between 40m to 1000m) each with the resample method; nearest neighbor (N), bilinear (B) and cubic convolution (C)] have been resampled from original SRTM 90m v4.1. ArcGIS desktop10.2

(ESRIInc., Redlands, CA) has been employed to do all the resampling. The symbolized names of all the forty-eight scenarios are listed in Table 5.3.

Table 5.2: Sources of input data and temporal availability in study area

Data	**Source**	**Spatial/Temporal resolution**
Soil	http://swat.tamu.edu/docs/swat/india-dataset/2012/soil_HWSD_FAO.7z	7225 m
Land use	http://www.globallandcover.com/GLC30Download/index.aspx	30 m (2010)
Climatology	http://rda.ucar.edu/pub/cfsr.html. Daily data for temperature, wind speed, relative humidity, and solar radiation from Climate forecast system re-analysis (CFSR)	~0.2º(1979-2014)
Rainfall	Daily rainfall data from APHRODITE (http://www.chikyu.ac.jp/precip/)	0.25º(1957-2007)
Discharge	Daily discharge from Central Water Commission, Gov. of India	(2000-2012)
DEM	SRTM DEM V4.1 (http://srtm.csi.cgiar.org/SELECTION/inputCoord.asp)	90 m (Latest, 19th April 2008)

Table 5.3: Symbolized representative names of different DEM scenarios (N stands for nearest neighborhood, B for bilinear and C for cubic convolution)

DEM (m)	**40**	**50**	**60**	**70**	**80**	**90**	**100**	**150**	**200**	**300**	**400**	**500**	**600**	**700**	**800**	**1000**
N	40N	50N	60N	70N	80N	90N	100N	150N	200N	300N	400N	500N	600N	700N	800N	1000N
B	40B	50B	60B	70B	80B	90B	100B	150B	200B	300B	400B	500B	600B	700B	800B	1000B
C	40C	50C	60C	70C	80C	90C	100C	150C	200C	300C	400C	500C	600C	700C	800C	1000C

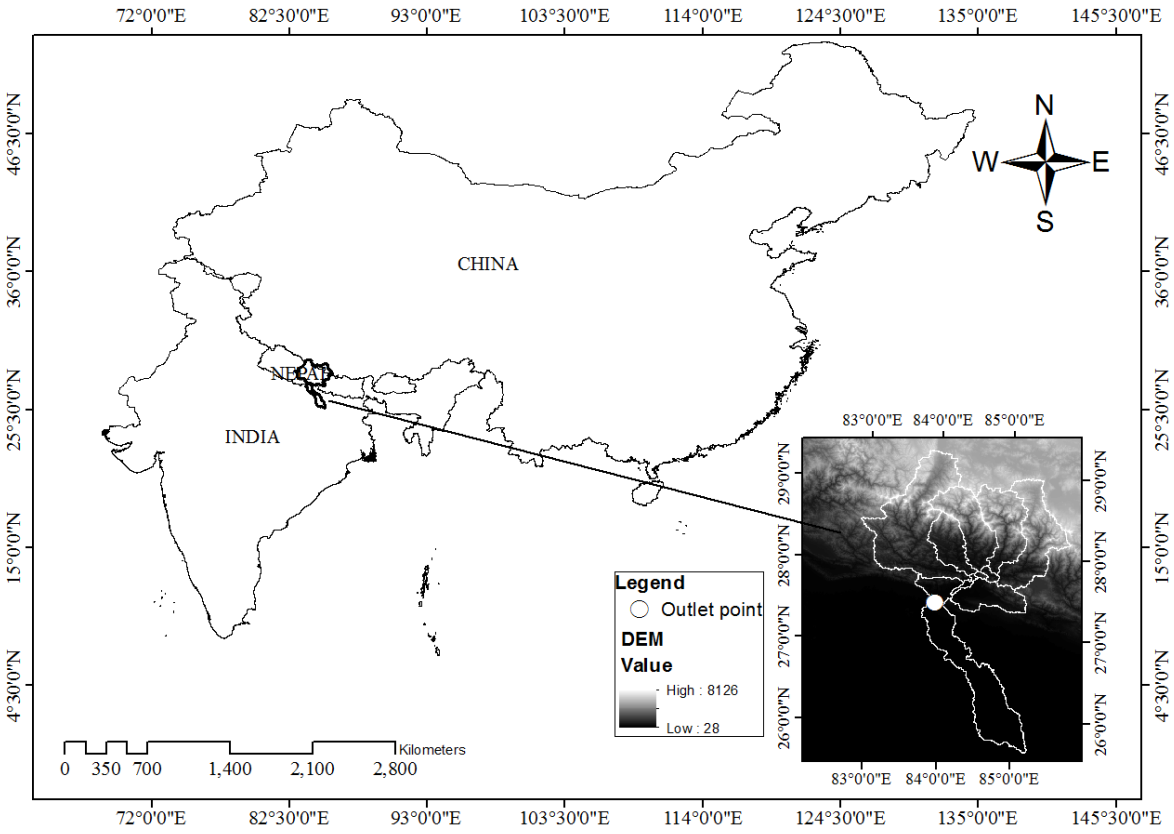

Figure 5.1: Location of study site along with stream gauge (outlet point) and DEM map

5.2.2 SWAT Model and Uncertainty Analysis

SWAT model [213] is a semi-distributed hydrological model which is developed by the United States Department of Agriculture, Agricultural Research Service (USDA ARS). It can predict the flow, sediment and nutrients load reasonably for large ungauged basins [88,232]. SWAT simulates runoff based on the United States Department of Agriculture, Soil Conservation Services- Curve Number Method, 1972 (USDA, SCS-CN) while it manages snowmelt simulation with the Temperature Index Snowmelt Model (TISM) using ten elevation bands [88,215]. To estimate sediment load, SWAT uses Modified Universal Soil Loss Equation (MUSLE) [233] while it estimates the nutrients load by tracing the improvements and transformations. Soluble nitrogen and phosphorus loads have been assessed with the water volume and average concentrations of these in the soil layers [44]. The mathematical formulations to calculate carriage of phosphorous and nitrogen loads have been established by McElroy et al. 1976 [234] and modified by Williams and Hann 1978 [235].

SWAT2012 (http://swat.tamu.edu/) has been used in this study. It divides the watershed into sub-basins and then into Hydrological Response Units (HRUs) based on land use, soil and slope group. Each sub-basin holds the flow paths, channels, slope, and the boundary that are required for routing of the flow, sediments and nutrients load. The computation of all these rely on the input DEM, whose grid size majorly influences the flow and nutrients load modeling through the topographic attributes [40]. Thus, during the evaluation of uncertainty in the SWAT model outputs owing to DEM grid size and resampling methods, it is required to examine the uncertainties in the watershed topographic inputs. Therefore, the topographic characteristics from basin: number of HRUs and sub-basins, area, mean basin slope, mean basin altitude, and perimeter; from sub-basin: field slope and longest path; from reach: mean slope, mean reach depth and width have been examined. Because of more than one sub-basins and reach in the study area, all the considered topographic characteristics have been averaged to simplify the assessment.

It is worth mentioning that the model outputs (flow, sediment, and nutrients load) are affected due to changes in DEM resolution and resampling methods due to the representation of the topographic characteristics and model parameters. SWAT model resamples the grid size of the spatial inputs viz. soil and land use as per the input DEM grid size. This implies that the interception, infiltration, and ultimately runoff generation process

may be altered due to the changed soil and land cover parameters. Furthermore, elevation band based TISM uses precipitation and temperature lapse rate parameters which depend on DEM [215,232]. Thus, the change in the temperature and precipitation lapse rate owing to altered DEM resolution and resampling method may affect the snowpack formation and snowmelt processes. Therefore, measured uncertainty is the overall uncertainty in the whole complicated model.

Initially, SWAT model was run on a daily basis with all input data mentioned in Table 5.2. Then, it was calibrated with the observed flow (for eight years 2000-2008, considering both runoff and snowmelt). SUFI-2 optimization algorithm inbuilt in SWAT-Cup has been used to automatically calibrate the SWAT model considering Nash–Sutcliffe efficiency (NSE) as the objective function. During calibration, parameters have been replaced using "V" method (existing parameter value to be replaced by true value) and "R" method (exiting parameter value to be replaced with relative multiple value) for the different simulations. The model performance is considered satisfactory if NSE $\geq$0.5, $R^2 \geq 0.5$ and PBIAS =$\pm$ 25%. The following equations are used to calculate R^2, NSE and PBIAS-

$$R^2 = \left(\frac{\sum_{i=0}^{n} (O - \overline{O})(P - \overline{P})}{\left[\sum_{i=1}^{n} (O - \overline{O})^2 \sum_{i=0}^{n} (P - \overline{P})^2 \right]^{0.5}} \right)^2 \tag{5.1}$$

$$NSE = 1 - \frac{\sum_{i=1}^{n} (O - P)^2}{\sum_{i=1}^{n} (O - \overline{O})^2} \tag{5.2}$$

$$PBIAS = \frac{\sum |O - P|}{\sum O} * 100 \tag{5.3}$$

In the Himalayan region, snow accumulation takes place in the areas having elevation greater than 3000 m [236,237]. Thus, TISM with five elevation bands has only been used for the sub-basins having altitude greater than 3000m. These sub-basins are sub-basin 1, sub-basin 3, sub-basin 4, sub-basin 6 and sub-basin 7 (Figure 3.1). The calibrated parameters are found to be above the satisfactory limit when evaluated in terms of objective function NSE. The statistical indicators NSE= 0.956, R^2 0.925 and PBIAS =19.2% show excellent agreement of calibrated flow with the observed flow (Figure 5.2). The calibrated parameters for flow are given in Table 5.4.

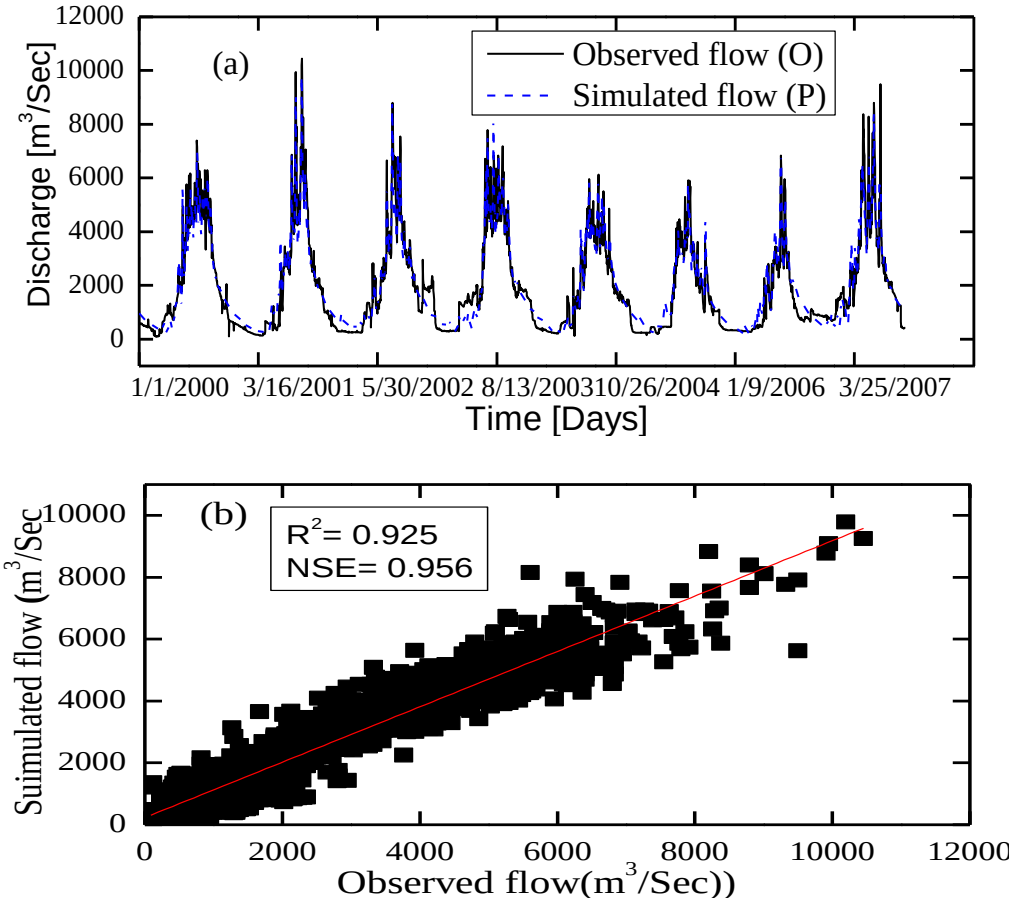

Figure 5.2: Comparison of simulated and observed daily discharge (a) time series plot (b) scatter plot for the Triveni Ghat site of the GRB

Table 5.4: SWAT parameters description, range, method adopted to fit and fitted value

Sl. No.	Parameter. File	Description	Method	Range		Fitted value
				Min	Max	
1	CN2.mgt	Initial SCS II value	R	-0.2	0.07	-0.078
2	ALPHABF.gw	Base flow alpha factor (days)	V	0.45	1.35	1.17
3	GW_DELAY.gw	Ground water delay (days)	V	30	252	80.06
4	GWQMN.gw	Threshold water level in shallow aquifer for base flow (mm H_2O)	V	1006	3668	1851
5	CANMX.hru	Maximum Canopy storage	V	31	95	70.97
6	CHN2.rte	Manning's "n" value for the main channel	V	0.14	0.4	0.232
7	CH_K2.rte	Effective hydraulic conductivity of channel (mm/hr)	V	148	446	170.5
8	EPCO.bsn	Plant uptake compensation factor	V	0.18	0.73	0.21
9	ESCO.bsn	Soil evaporation compensation factor	V	0.37	1	0.73
10	GW_REVAP.gw	Revap coefficient	V	0.01	0.26	0.16
11	REVAPMN.gw	Threshold water level in shallow aquifer for revap (mm H_2O)	V	242	500	335.26
12	SLSUBBSN.hru	Slope length (m)	R	-0.5	0.17	-0.29
13	SOL_ALB.sol	Moist soil albedo	R	-0.6	0.13	0.057
14	SOL_AWC.sol	Available water capacity	R	-0.32	0.23	-0.24
15	SOL_K.sol	Saturated hydraulic conductivity of first layer(mm/hr)	R	-0.12	0.5	0.46
16	SOL_Z.sol	Depth from soil surface to bottom of layer (mm)	R	0.025	0.5	0.15
17	SURLAG.bsn	Surface runoff lag coefficient	V	0.05	12	9.48
18	HRU_SLP.hru	Average slope steepness (%)	V	0.03	0.68	0.20
19	BIOMIX.mgt	Biological mixing efficiency	V	0.44	1	0.81
20	SFTMP.bsn	Mean air temperature at which precipitation is equally likely to be rain as snow/freezing rain (^oC)	V	-2.6	2.45	-0.078
21	SMTMP.bsn	Threshold temperature for snow melt (^oC)	V	-2.8	20	19.35
22	SMFMX.bsn	Snow melt factor on June 21 (mm H_2O/ day-^oC)	V	7.8	20	9.62
23	SMFMN.bsn	Snow melt factor on December 21 (mm H2O/^oC-day)	V	4	15	6.54
24	TIMP.bsn	Snow temperature lag factor	V	0	0.58	0.40
25	SNO50COV.bsn	Snow water equivalent to 50% of snow cover	V	0	0.56	0.15
26	SNOCOVMX.bsn	Minimum snow water content corresponding to 100% snow cover	V	141	425	278
27	PLAPS.sub	Precipitation laps rate (mm/Km)	V	-478	564	150.85
28	TLAPS.sub	Temperature lapse rate (^oC/Km)	V	-10	2	-5.57

V and R are replace and relative change methods for parameter value during simulation.

Then, the SWAT model is used for all the scenarios (Table 5.3) on a daily basis using the calibrated parameter of flow (Table 5.4) and keeping other parameters and conditions constant. These conditions are (1) the same such as meteorological data, land use, soil, reservoirs and ponds and land management practices; (2) default minimum upslope drainage area for stream network extraction; (3) the same HRUs definition threshold viz. land cover (10%), soil (15%) and slope (15%); (4) five elevation bands for each sub-basins having elevation greater than 3000m. The SWAT outputs flow, sediment, total nitrogen (TN), total phosphorous (TP) are the model output of interest [44] to analyze the uncertainty in this study.

It is important to address here that transferring calibrated parameters to the different scenarios (Table 5.3) may better address the uncertainties arising due to DEM grid size and resampling methods. In previous studies [44,46] researchers kept all the default SWAT parameters but in an area like ours, it becomes idle where the snow phase of modeling strongly depends on the altitude. Secondly, SWAT calculates TN and TP with the water volume and average concentrations of these in the soil layers [44,233]. Thus, error in the flow volume due to the default snow module parameters may also affect the TN and TP for the different scenarios.

The SWAT model outputs uncertainty have been calculated using statistical indicators relative difference (RD) [39,44,46] as:

$$\mathrm{RD} = \frac{\mathrm{P_{x\_R}} - \mathrm{P_{90B}}}{\mathrm{P_{90B}}} \tag{5.4}$$

where P_{x_R} is the monthly predicted SWAT outputs at DEM grid size (x) and resampling technique (R) and P_{90B} is the monthly SWAT outputs at 90m bilinear resampled DEM. Monthly P_{90B} SWAT outputs have been assumed to be the best and therefore they have been considered as the base data for the comparison. The results and discussion section of this manuscript uses RD as an uncertainty measure (RD of +ve i.e. the overestimation and RD of –ve i.e. the underestimation).

5.3 Results

5.3.1 Topographical Characteristics of Basin, Sub-basin and Reach

Topographic characteristics of the basin, sub-basin, and reach based on the different scenarios have been studied to understand the effect on SWAT outputs besides the altitude itself (Figure 5. 3 and Figure 5.4). The RD of the mean basin altitude [Figure 5.3(a)] is not sensitive to the scenarios for <500m for grid size while beyond 500m of grid size, RD is positive with the maximum for 1000C. The RD of the mean basin slope [Figure 5.3(b)] is positive for the scenarios <60m of grid size and between 60-100m of grid size it is almost zero. Thereafter, for the scenarios >100m of grid size, it is consistently decreasing with negative as the grid size increases. The maximum negative value of RD for the mean basin slope is found for 1000C, perhaps due to the topographic loss caused by the averaging of sixteen adjacent pixels. The B scenarios show relative less RD for the mean slope at the <100m of grid size than N and C. The RD for the mean basin area [Figure 5.3(c)] is almost zero till 500m of grid size for all scenarios but beyond 500m of grid size, it is negative for B and positive for C.

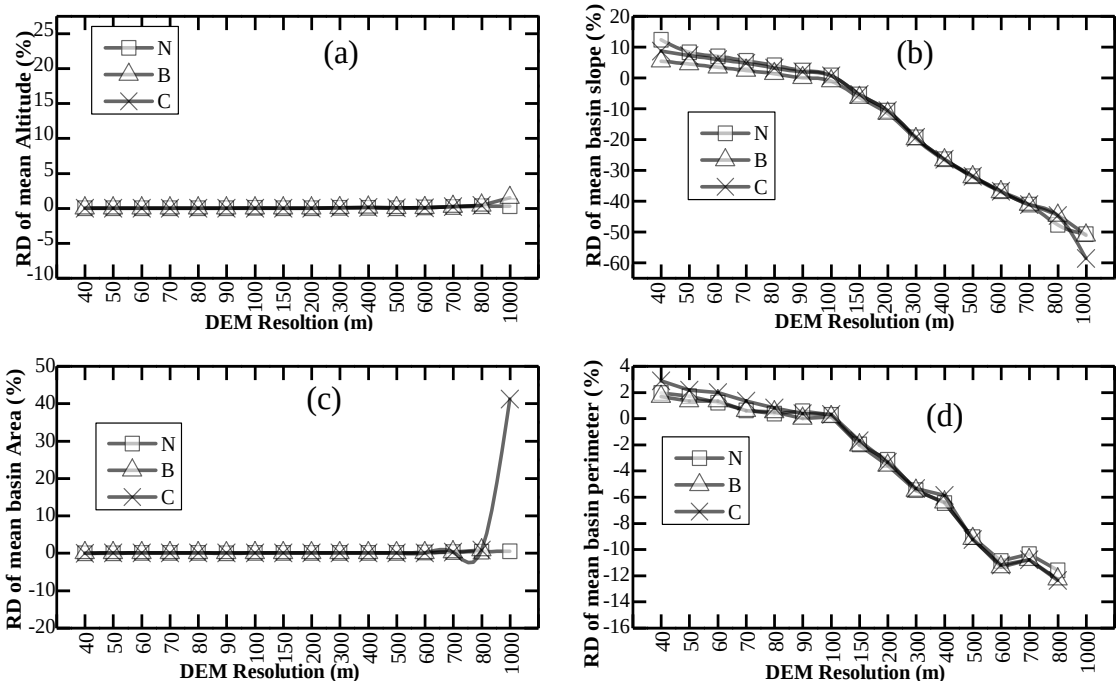

Figure 5.3: Basin level topographic characteristics derived from varying DEM resolution and resampling methods

The RD for the mean basin slope deviates between 12% to -50% for N, 5% to -51% for B, and 8% to -58% for C due to the subsequent change in the DEM grid size range from 40 to 1000m. It means, the basin slope is sensitive to change in the DEM grid size. This is similar to Lin et al.[44] where the slope is found decreasing with increase in the coarser grid size of DEMs. The B scenarios indicate small range of RD than N and C that implies B is better than the other two. The change in the sign of RD (from positive to negative) for the mean basin slope indicates an increase in the steepness or flattening for the surfaces. Similar to the basin slope, the basin perimeter [Figure 5.3(d)] is also changing with DEM grid size. This implies that basin shape features may change owing to the DEM scenarios.

The watershed delineation shows that the number of sub-basins does not change for 40-300m of grid size scenarios [Figure 5.4 (a)]. After 300m of grid size, the number of sub-basins gets decreased for N, while for B and C the pattern is random. On the other hand, the number of HRU increase significantly beyond 100m of grid size. That is due to a decrease in the shape features of the watershed and which portray the shape features to reach easily to the threshold limit for driving an HRU.

The RD for the field slope length [Figure 5.4(b)] is almost zero up to 100m of grid size owing to relatively small RD for the counterpart slope up to this limit. Beyond 100m of grid size, the RD for the field slope length increases and reaches more than 50% for 1000C. The reach slope and the longest path [Figure 5.4(c) and (d)] vary substantially, but no noticeable trend has been found for them. The reach widths [Figure 5.4(e)] and reach depths [Figure 5.4(f)] are the function of the rainfall-accumulated areas, and thus, they should not be sensitive to DEM grid size and resampling methods. But they differ for the DEMs <300m of grid size. This may be due to the massive elevation loss in DEMs caused by resampling to a coarser grid size.

5.3.2 Impact of DEM Uncertainties on H/NPSP Estimates

For flow [Figure 5.5(a)], the RD is $\pm$10% and most of the time near to zero for scenarios falling within $\leq$300 m of grid size; however 60N and 90N are the two aspersions where it is found >10%. The RD for flow is positive for the DEMs grid size >300 to <700m and negative for >700m of DEMs grid size. The maximum RD for the flow has been found to be 34.7% at 600B. The comparison for RD of flow for N, B and C, B scenarios show small RD for the DEMs below 300m of grid size. Figure 5.5(a) also explores the variation of RD

within a season. In the summer/monsoon period (April to July), the RD is almost bell shape and peak increases with coarser DEMs grid size. The summer/monsoon season also shows relatively mild peaks for RD at ≤300m of grid size.

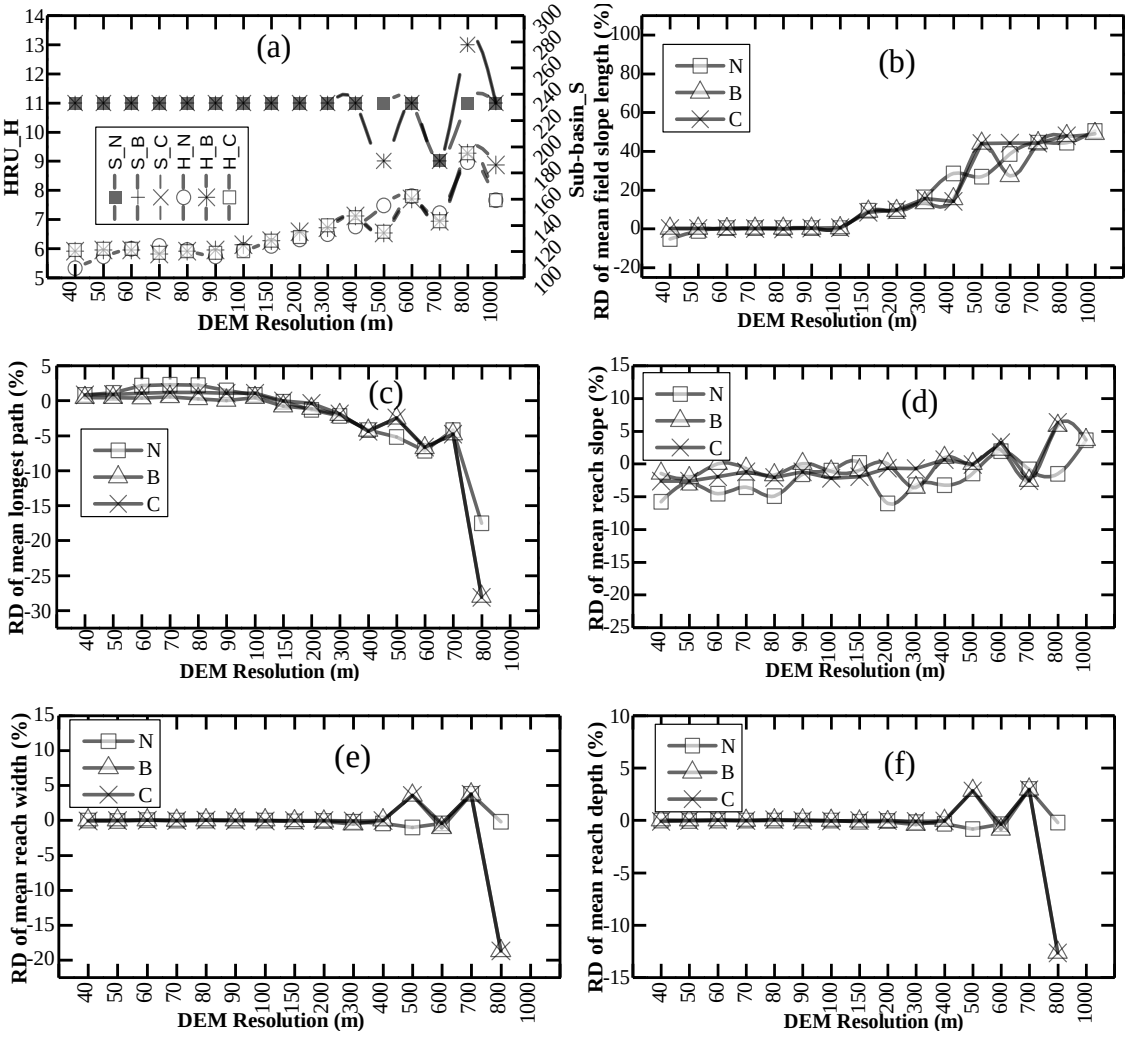

Figure 5.4: Sub-basin level topographic and reach characterizes derived from varying DEM resolution and resampling techniques

The RD for sediment [Figure 5.5(b)] has been found between -5 to 5% for most of the scenarios falling within ≤150m of grid size. After 150m of grid size, N scenarios have been found to be positive. However, B and C exhibit positive trends for the DEMs >150m and ≤700 m of grid size and beyond that, both have negative trends. The seasonality effect has been found similar to the flow for the sediment loads during the monsoon period. For sediment loads, B scenarios show small RD rather than N and C for the DEMs ≤150m of grid size.

The Figures of RD for TN and TP are similar to each other, except the differences in the magnitude [Figure 5.5(c) and 5.5(d)]. The RD for both is between -5 to 10%, up to 150 m of grid size, except for 60N and 90N. For both, the variation in the peaks of RD has been found similar to the flow [Figure 5.5(a)]. The maximum RD variation for TP and TN is for 1000N, which is almost 200% and 300% respectively. Among N, B and C scenarios, B exhibits small RD for TN and TP for all DEMs grid size.

It is vital to see the significance in the change between base outputs (90B) and the various scenarios at different temporal scale viz. yearly/monthly. The T-test statistics have been used to evaluate the change if any exists between them. Figure 5.6(a) shows that flow, TN and TP are not changing significantly at a yearly time step for the DEMs ≥500m of grid size except aspersion at 60N and 90N. Sediment is found more susceptible than flow, TN and TP at yearly time step that has been shown by significant t-test results for grid size ≥200m. No any significant change in the flow, TN and TP have been observed due to the DEMs grid size for all resampling methods on a monthly scale [Figure 5.6(b)], while, t- test statistics have been found significant for sediment load for DEMs >600m in this temporal resolution. Also, Figure 5.6 exhibit that SWAT outputs manifest similar pattern significance plot varying with magnitude. Among N, B, and C scenario SWAT outputs, C shows inconsistent t-test results for different DEM grid size while B is found most consistent. The results also demonstrate that the uncertainties increases with increase in temporal resolution and decreases with increase in spatial resolution.

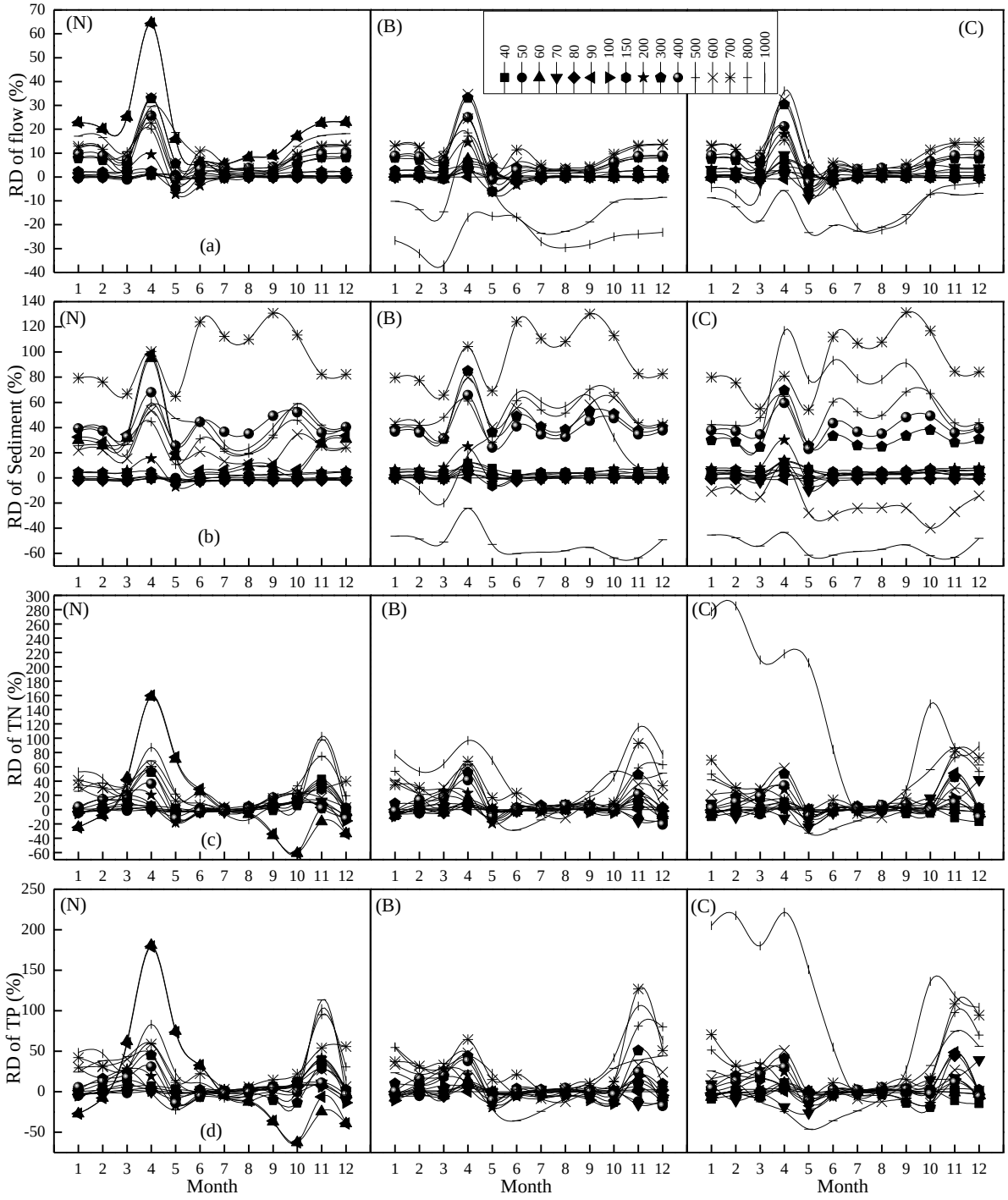

Figure 5.5: The temporal sensitivity of average monthly SWAT outputs (period 1983-2007) at the different months varying with different DEM resolution and resampling techniques

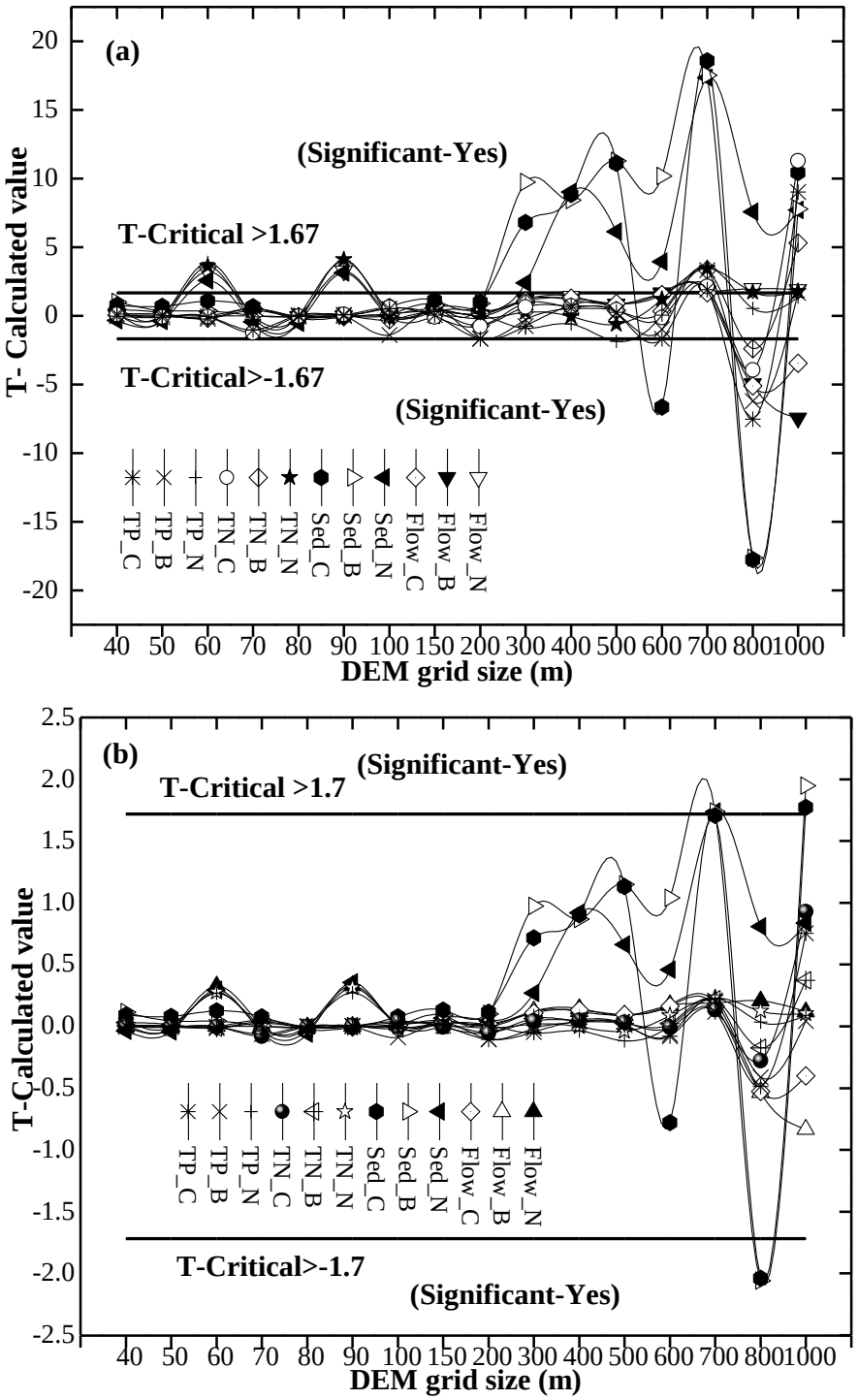

Figure 5.6: Results of significance test (a) yearly (b) monthly time steps. SWAT outputs are not significant with in T-Critical band (T-Critical bands are ±1.7 and ±1.67 at the monthly and yearly time steps respectively)

5.4 Discussion

It is always desirable to compute the various hydrological elements in a large basin in a very short time. Also, at times hydrological models use particular grid sizes for the input. The resampling methods have been used to fulfill the above-said needs for the last few decades. The modeler should be aware of the effect of resampled inputs grid size on the model outputs because resampled grid size is not a real. The resampled grid size for a spatial data is the nominal representation based on resampling methods. Here, various uncertainties in the SWAT model outputs due to the resampled DEMs grid size have been discussed.

5.4.1 Flow

The river flow is the combined effect of runoff from the land and melted water from snow and glaciers. Runoff and snowmelt can be simulated simultaneously in the SWAT model. SWAT2012 uses SCS-CN method to calculate the surface runoff (Q_{surf}, mm).

$$Q_{surf} = (R_{day} - I_a)^2 / (R_{day} - I_a + S) \tag{5.5}$$

where R_{day} is the rainfall for the day (mm), I_a the initial abstraction losses (mm) and S the soil retention parameter (mm) that is a function of the curve number (CN) value for the day.

In the snow module of SWAT2012, snowpack and snowmelt depend on the mean daily air temperature (T_B) and the mean precipitation (P_B) of a particular elevation band [88,215,238]. It has been described as elevation bands based TISM which is given as:

$$T_B = T + (Z_B - Z) * dT / dZ \tag{5.6}$$

$$P_B = P + (Z_B - Z) * dP / dZ \tag{5.7}$$

where T_B is the mean temperature for a particular elevation band (^{O}C), T the measured temperature (^{O}C) at the weather station, Z_B band's midpoint elevation (m), Z the elevation of weather station (m), P_B the band's mean precipitation (mm), P the precipitation measured at the weather station (mm), dT / dZ the temperature lapse rate (mm/km) and dP / dZ the precipitation lapse rate (^{O}C/km).

SWAT2012 does not adjust CN for slope (Equation 5.5) and this is the reason that runoff does not change with the change in the mean basin slope for DEMs <600m of grid

size, except a tiny deviation during snowmelt season. The consistent trend in the runoff and perimeter variation for different resampled DEMs grid sizes have been observed. Secondly, the flow and mean altitude exhibits a comparable variation for the DEMs grid size >600m and beyond 600m of DEMs grid size, the flow variation is random. This is only due to change in the temperature and precipitation lapse rate (Equation 5.6 and 5.7). The temperature and precipitation lapse rate depend on the elevation. Therefore, the mean elevation of an elevation band may alter due to change in the terrain elevation owing to resampling of DEMs grid size. That ultimately affects the snowpack and snowmelt and finally resultant flow. Figure 5.3, show a significant change in elevation for resolutions >700m for B and C, that explains the significant change in the flow for the counterpart scenarios (Figure 5.5). The overestimation nature of the flow (positive RD) for DEMs >300 to <700 m of grid size is mainly attributed due to changes the in water accumulation areas [44].

5.4.2 Sediment

SWAT2012 uses MUSLE [233] to predict the erosion (sed_{surf}) caused by rainfall and runoff which is given as:

$$sed_{surf} = (Q_{surf} q_{peak} area_{hru})^{0.56} * K * L * S * C * P * CFRG \quad (5.8)$$

where q_{peak} is the peak runoff rate (m^3/s), $area_{hru}$ the area of the HRU (ha), K the soil erodibility factor, C the cover and management factor, P the support practice factor, L the slope length factor, S the slope factor, and CFRG the coarse fragment factor. In this study, the sediments did not change as much as the mean reach slopes and field slope lengths because the SWAT sediment output is the combined effect of erosion on the field and their transport by the channel network. The sediment transport process in the channel network is the function of degradation and sedimentation. Thus sometimes, it may show less sediment in the downstream reach due to the deposition of sediment in the upstream reach.

From Equation 5.8, Sed_{surf} is directly proportional to the L and S. This implies that if L and S increase then Sed_{surf} should increase and vice-versa. The field slope length [Figure 5.4(b)], shows almost ± 10 RD for DEMs <150m grid size and after that the RD exhibits overestimating nature except for few coarser grid size. This may be one reason for the overestimation of Sed_{surf} for coarser DEMs. From Figure 5.4(d), the slope factor S shows

consistent increments with coarser DEMs that may also be affecting Sed_{surf} in the overestimating nature. Sed_{surf} is also directly proportional to the Q_{surf} (RD of flow, Figure 5.5) and that explains the similar peaks and patterns for the sediment and the flow.

5.4.3 TN and TP

SWAT model simulates the soluble N and P in the flow as a product of the volume of water and the average concentration of N and P in the soil layers; however they are not directly sensitive to the DEM grid size. T and P may increase due to the detachment of more sediment in the field. The RD of TN and TP (Figure 5.5), increases and decreases in a similar pattern like RD of flow (i.e. volume of water). In this study, the variation for TN and TP have been found similar to the reach slope [Figure 5.4(d)]. This indicates that TN and TP are being affected by DEM grid size via reach slope. For a few scenarios, estimated nutrients load have not been found in the conventional pattern like volume of flow and reach slope for which no any reasonable justification has been found.

5.5 Summary

Spatially variable digital elevation is the principal source of uncertainty in hydrological modeling. In hydrological modeling, coarser grid size of inputs are needed to speed up the simulation. Also, sometimes a specific grid size of model inputs are desired for the particular hydrological models. In such cases, we need to resample the grid size of model inputs. In this study, the SWAT model uncertainties have been studied due to DEM grid size and resampling methods on H/NPSP modeling. Based on the discussion, following points have been summarized -

- The watershed and reach characteristics do not vary significantly for scenarios <150 m of grid size; however for coarser scenarios (DEMs grid size >150 m), they vary significantly. Similarly, the number of sub-basins and HRUs change very little for DEMs <300m of grid size but after 300m of grid size, they vary substantially.
- At a yearly time step, t-test statistics have been found to be considerable for the coarser scenarios (DEMs >500m of grid size). That means they are differing significantly from each other at a yearly time step. Whereas, t-test statistics shows no significant change in the outputs for all scenarios at a monthly time step, except for sediment at the DEMs >600m of grid size.

- If the flow is desired output and the permissible RD limit is ±10%, then we may choose DEMs grid size ≤ 300m. On the other hand, if sediment and nutrients (TN and TP) are the focused outputs and the permissible RD limit is -5 to 10% then DEMs ≤150m of grid size can be picked.
- Among Nearest neighborhood (N), Bilinear (B) and Cubic convolution (C) resampling methods, Bilinear (B) resampled DEMs have been found with small RD in the SWAT outputs.
- The change in the terrain elevation due to resampled DEMs also affects the snow-melt parameters in the SWAT model and finally the SWAT outputs.
- Uncertainties in the model outputs increase with increase in temporal resolution and decreases with increases in spatial resolution.

The watershed characteristics are crucial for physically-based hydrological models. These characteristics change with varying DEM grid size and resampling methods, which is why they cause significant changes in the model outputs. To reduce the uncertainties, the optimum DEMs grid size, and resampling method should be understood for the specific watershed and focused SWAT output. The modeled results for the fine grid size of DEM scenarios exhibit no significant differences in the SWAT outputs. The finer grid size DEM resampled with Bilinear resampling method could avoid the uncertainties in the model results.

Chapter 6

Uncertainty due to Different SWAT Setups

Models are the simplified representation of real system. In distributed modeling, modelers try to reach towards realism. For that, distributed models are governed by various equations for each processes involved in the system that can be solved using various inputs and model parameters. Sometimes, modeler breaks the traditional way of setting the distributed model to manage with limited data and parameters, thus introduces uncertainties in the modelled results. In this chapter, uncertainties in the results arising due to SWAT structures owing to different model setups and input parameters have been discussed.

6.1 Introduction

Himalayan River basins are covered with ice and snow throughout the year. Upstream ice and snow reserves of these basins are vital in sustaining seasonal water availability for most of the Southeast Asian Rivers. Seasonal snowmelt water carried by these rivers are the primary source of supply for over 1 billion peoples living in the region specifically during spring at the onset of the growing season [239,240]. Glacier and snowmelt are critical hydrologic processes in these areas [241,242]. Therefore, hydrological modeling approaches need to incorporate snowmelt to simulate stream flow and snow cover dynamics [92,218].

There are basically two types of the snowmelt models: 1) Conceptual Temperature index or degree-day based models such as SWAT and Snowmelt Runoff Model (SRM) [213,243] and 2) Energy balance based snowmelt models such as Utah Energy Balance (UEB) model [212]. Missing *in-situ* snow cover information for the Himalayan region hampers the latter modeling studies [214]. Temperature index or degree-day models have outperformed energy balance models on a catchment scale [215,216]. However, there are limitations and decreasing accuracy with an increase in the temporal resolution and spatial variability due to topographic effects [215]. In some extent, Temperature index model with

elevation bands [216,217] has overcome some of these limitations. Omani et al. [244] has shown that SWAT distributed algorithm can be used to simulate mass balance (MB) and Equilibrium Line Altitude (ELA) of glaciers. Moreover, the topographic variables have an effect on climatic controls in the Himalayas [219,220]. Simple temperature index snowmelt models use degree-day factor for ice and snow, the gradient of air temperature and precipitation. These vary significantly with elevation for the complex Himalayan terrain [221–227]. Therefore, a suitable snowmelt routine needs to be developed and used for operational hydrological simulations in this region.

Several studies have shown the impact of snow when evaluating streamflow and climate change impact over Himalayan River Basins [241,244–248]. Couple of studies [212,244] have been reported using energy balance snowmelt modeling approach while others are with simple degree-day formulation based temperature index model [108,245,249]. In the operational framework of snowmelt routine within a hydrological model one can adopt among two approaches. In the first approach, snowmelt routine considers snowpack reservoir only to improve the streamflow simulation without authentication of snowpack simulation for water content, spatial and temporal evolution [218,245]. The second approach simulates snowpack in terms of "snow water storage" during hydrological modeling [92,250]. The later modeling approach is constrained by the unavailability of in-situ snow data. In this context, satellite driven remote sensing products are providing an independent source of critical observations to validate modeled results [3]. For example, Moderate Resolution Imaging Spectro-radiometer (MODIS) is very popular remote-sensed snow data source that has been used for hydrological and climate change studies in this region [214,236,241,246,251].

There are numerous studies related to the stream flow modeling in conjunction with simulation of spatiotemporal snow cover in the Himalayan region, and a review of critical studies are presented here. Satellite remote sensing has proved to be a good observational tool for estimation of soil moisture [252], water balance in ungagged basins [253], groundwater as well as the hydrological cycle [254]. Various remote sensing products have been reported for estimation of snow cover area [255] and out of them, several products are being used for hydrological studies in past. Immerzeel et al. (2009) [241] used MODIS snow product MOD10C2 to examine the spatiotemporal snow cover and runoff simulation. They used temperature index based Snowmelt Runoff Model (SRM) to simulate runoff for a

single gauge station which shows a good agreement in terms of PBIAS (2%) and Pearson correlation coefficient of 0.88 between observed and simulated streamflow. They also demonstrated that the MODIS data is able to detect spatiotemporal pattern in the Himalayan region. Shrestha et al. (2012) [246] applied a three layered energy balance snowmelt model named WEB-DHM-S (Water and Energy Budget–based Distributed Hydrological Model) at daily time step and 1km of spatial resolution over the Dudhkoshi Himalayan River Basin. They found that the WEB-DHM-S generated snow cover agreed well with MODIS product MOD10A2 with an average accuracy of 90% for comparison of snow free and no-snow grids. Siderius et al. (2013) [251] applied four hydrological models namely VIC, JUES, LPJmL and SWAT over the Ganges River Basin. These models were coupled with regional climate models to estimate snowmelt contribution to the streamflow for present and future scenarios. Brown et al. (2014) [244] developed an integrated runoff and snowmelt model called HIMALA BASIN to compute the contribution of snow and glacier melt into the streamflow for Hindu-Kush Himalayan River Basins. They provided a case study for Langtang Khola watershed, which shows a reasonable good agreement of measured (5.02m) and simulated (5.31m) basin average streamflow-depth over the eight years (2003-2010) of the time span period. Devkota and Gyawali (2015) [249] used two regional climate models over the Koshi River basin to carry out future runoff simulations using SWAT for the Chatara outlet of the basin. They revealed the impact of future scenarios on hydrological regimes which changes the flood frequency for a given return period. The flood frequency for a given return period was found to be dependent on the climate run that is considered.

Critically, in the past, whether streamflow modeling studies have been done with energy balance or degree-day snowmelt models, all examples were confined to small watersheds with a single gauge at downstream of major snow accumulated areas. Moreover, it is important to consider elevation band effect on snowmelt analysis for snow-affected sub-basins in order to improve the water management in the large mountainous Himalayan River Basins.

In this study, an attempt has been made to determine (1) Suitable model setup within the SWAT model and (2) Optimal number elevation bands for TISM inbuilt in the SWAT for large Himalayan River Basin. Also, an attempted has made to simulate spatial and temporal distribution of snow and its water equivalent at different snow affected sub-basins. A standard calibration procedure based on observed streamflow has been fallowed.

Furthermore, no direct calibration for snowpack and snow water equivalent is being done, but the simulated snow water equivalent is validated using snow cover factor (SCF) derived from the MODIS weekly snow cover product MOD10A2.

6.2 Data and Methods

6.2.1 Data

6.2.1.1 Hydrological and Meteorological Data

The descriptions of the various spatial and temporal datasets are given in Table 6.1. In this study, daily climatology inputs temperature (minimum and maximum), wind velocity, humidity, and sunshine hours were taken from Climate Forecast System Reanalysis (CFSR) [229] and precipitation from APHRODITE (Asian Precipitation High-Resolution Observational Data Integrated Towards Evaluation) [256] precipitation data. Forty one APHRODITE grid points fall within the basin that have been used as precipitation input for the model. A map locating stream gauge points and other features in the study site is given in Figure 6.1.

The CFSR is the latest hourly global weather forecasts produced by National Centers for Environmental Prediction (NCEP). Forecast models are initialized at every 6h from 0000UTC using information from satellite-derived products and global weather station network. The CFSR model outputs are available at a spatial resolution of ~38 Km and hourly temporal resolution. Recently, many studies have examined the feasibility of CFSR dataset for climatic studies over Indian continent [257–260]. The CFSR data has been downloaded from http://globalweather.tamu.edu/ in the SWAT format.

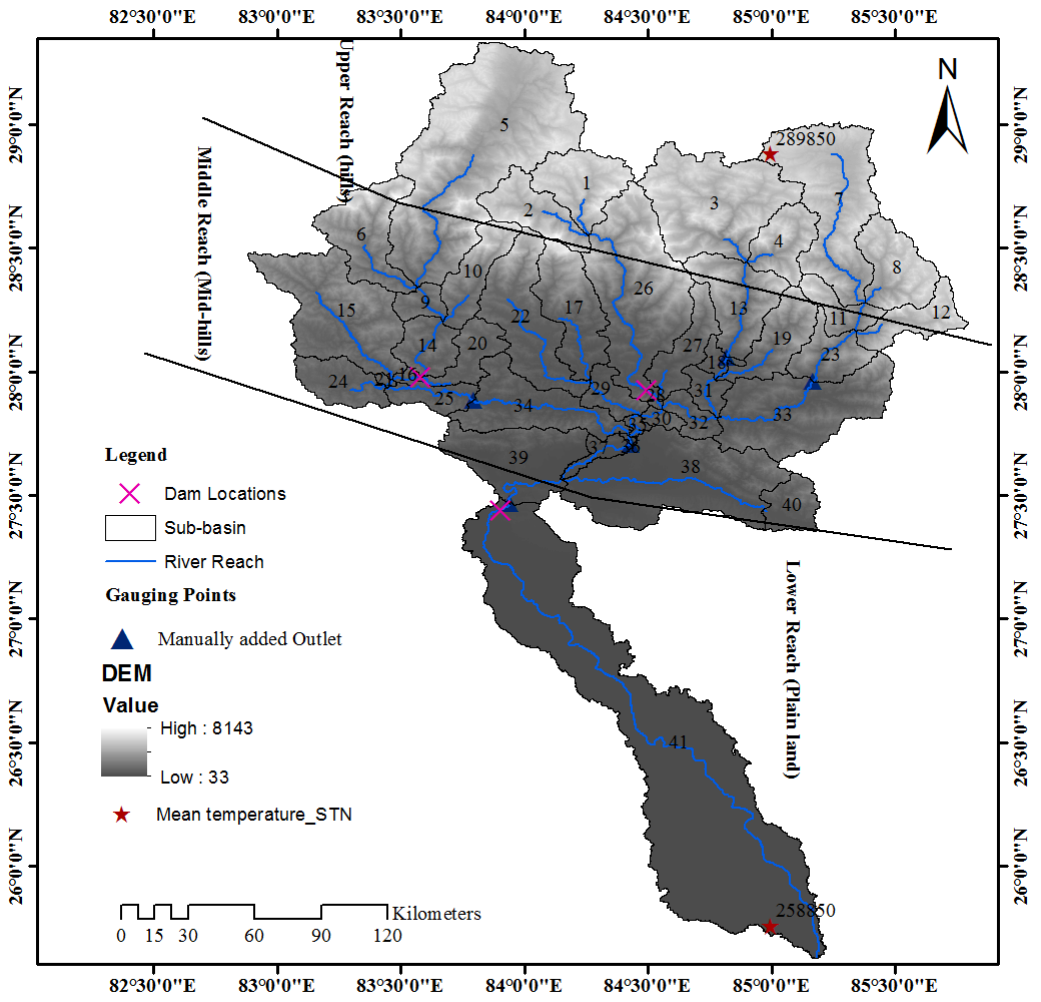

Figure 6.1: Locations of different stream gauge point (outlets), stream networks, mean temperature stations, dams, the reaches, sub-basins in the study site

Table 6.1: Table 6.1: Sources of input data and temporal availability in study area

Data	Source	Spatial/Temporal resolution
Soil	http://swat.tamu.edu/docs/swat/india-dataset/2012/soil_HWSD_FAO.7z	7225 m
Land use	http://www.globallandcover.com/GLC30Download/index.aspx	30 m (2010)
Climatology	http://rda.ucar.edu/pub/cfsr.html. Daily data for temperature, wind speed, relative humidity, and solar radiation from Climate forecast system re-analysis (CFSR)	~38km (1979-2014)
Rainfall	Daily rainfall data from APHRODITE (http://www.chikyu.ac.jp/precip/)	0.25°(1957-2007)
Discharge	Daily discharge data from Central Water Commission (CWC) gov. India and Department of Hydrology and Meteorology (DHM), Nepal	(2000-2007)
DEM	SRTM DEM V4.1 (http://srtm.csi.cgiar.org/SELECTION/inputCoord.asp)	90m (Latest, 19th April 2008)
MOD10A2 V6	http://nsidc.org/data-set/MOD10A2/versions/6	500 m, 8-day (Feb 2002- present)

The APHRODITE daily precipitation product is a state-of-art high-resolution (0.25°) dataset. This was accomplished by the Meteorology Research Institute of Japan Meteorological Agency (MRI/JMA) and the Research Institute for Humanity and Nature (RIHN) since 2006 [256,257]. It has been produced mainly with the *in-situ* rain gauge observation network data collected from the participating countries/organizations. The main objective behind developing APHRODITE dataset was to provide accurate quantitative estimate of precipitation for scientific studies related to climate change and natural resources management. The APHRODITE precipitation product can be downloaded from the site http://www.chikyu.ac.jp/precip/english/products.html that is available for the time span of 1951-2007. Few studies have validated the suitability of APHRODITE precipitation products over Himalayan region. Recently, Andermann et al. [261] evaluated five set of precipitation products available for Himalayan fronts and showed that distance weight interpolated APHRODITE gives the best precipitation estimates when compared with rain gauge precipitation data.

Daily streamflow data at five gauging stations (collected from DHM and CWC, Table 6.1) along the river reach were used to calibrate the SWAT model. Out of five, four gauging stations Narayanighat-36 (1963-2010), Kumalgoan-25 (1996-2010), Betrawati-23 (1977-2010), Arughat-13 (1964-2010) falls in Nepal and Triveni-39 (2000-2012) in Indian Territory. The selection of the streamflow gauging stations was planned in such a way that it could present the topographic diversity within the basin. Two gauging stations (36 and 39) fall in the plain areas while others in the mountains area (Figure 6.1). The ultimate intent was to calibrate along the river continuum considering the heterogeneity in the topography with in the sub-catchments.

6.2.1.2 Soil, Land use and MODIS Snow Cover Dataset

The spatial data inputs used for this study are DEM (SRTM 90m v4.1), soil map (FAO) and land use map (GlobeLand30). The SRTM 90m [231] is a joint project between the United States National Aeronautics and Space Administration (NASA), National Imagery and Mapping Agency (NIMA), and the German and Italian space agency. The SRTM mission (started in February 2000) covers almost 80% of the globe between 60N to 56S. The FAO world soil map is a 30 arc-second raster dataset and has more than 15000 soil mapping units that incorporate different national as well as regional updates of soil information. It combines the soil information at 1: 5000000 scale (FAO/UNESCO, 1995). GlobeLand30 global land use map [131] is produced using pixel-object-knowledge (POK) based operational approach developed by National Administration of Surveying, Mapping and Geoinformation (NASG), China. GlobeLand30 land use data uses imageries from Landsat TM/ETM+ and Chinese Environmental and Disaster satellite (HJ-1). POK based approach produces maps in ten land cover classes with a spatial resolution of 30m. The GlobalLand30 land cover data can be accessed from http://www.globallandcover.com.

Moderate Resolution Imaging Spectro-radiometer (MODIS) Terra and Aqua platforms produces many snow cover products, varying in temporal and spatial transformation. The MODIS global 8- day Terra snow cover product MOD10A2 is used in this study. MOD10A2 is a composite snow cover product with 500m spatial resolution, derived from the daily MODIS snow product MOD10A1. A pixel of MOD10A2 is classified as no snow pixel, only if that pixel has no snow in MOD10A1 product in the past eight days. Similarly, any pixel of MOD10A2 is classified as cloud, if that pixel is having cloud in the MOD10A1 product in the past eight days. Therefore MOD10A2 provides maximum coverage of snow, considering a filter for cloud and no snow pixels in the daily product MOD10A1. Several studies have been carried out to validate the MODIS snow cover products in the Himalayas and the Tibetan plateau [262–264] using high-resolution satellite imagery and ground observations. They illustrated a good agreement between field observed and MODIS snow cover area. Also, MODIS snow cover products have been widely used in various interdisciplinary research - for instance, input forcing for snowmelt runoff model [241,265] and to validate the modeling results [266,267]

For this study site, three hundred fifty MOD10A2 V6 (H25V06) images are downloaded from the site https://nsidc.org/data/MOD10A2#.n for the period 2000-2007.

Thereafter, images were re-projected in the WGS-1984/45N coordinate system at 500m resolution using nearest neighborhood resampling method in the MODIS Re-projection Tool [268]. An effective gap filling algorithm for cloud pixels in MODIS snow cover data was used [92,269]. The resulting gap free images were used to extract the snow cover factor (SCF) for first five snow dominated sub-basins to compute the change in the snow cover area at the eight-day time step. However, comparison for maximum and minimum snow cover area between MOD10A2 and SWAT model result at sub-basin-1 (section 6.3.2 and para 2) were carried out without any gap filling.

6.2.2 SWAT Model Description and Setup

SWAT model is able to simulate the impact on hydrology, sediment and nutrients load reasonably, due to physical changes brought in the large ungauged river basins [88,232]. It is a semi-distributed hydrological model that works on the concept of discretization of the watershed area into small homogeneous units called Hydrological response units (HRU). It first delineates the whole basin into different sub-basins based the defined threshold accumulation area and then it creates HRUs within each sub-basin based on the unique soil type, land use, and slope. It then computes water balance in each HRU based on the four reservoirs; snow, soil, shallow aquifer, and deep aquifer. Basic hydrological components within SWAT model are streamflow, evapotranspiration (ET), percolation and lateral flow. The water balance computed in each HRUs are then aggregated and routed towards river reach and basin outlets. The SWAT model is chosen in for this study because it can compute various hydrological fluxes including snowmelt [215,216,270–272]. The SWAT model integrated into the ArcSWAT 2012 (an ArcGIS based graphical user interface of SWAT model) has been used in this study because ArcSWAT easily/quickly processes various topographic and spatial inputs needed to run SWAT model. The detailed description for various SWAT setup can be found in the Rahman *et al.* 2013[218] and Neitsch *et al.*, 2011[232].

The computation for various phases in the SWAT model is based on the modeling setups-

1. Reference project (RP): calibrated for sensitive parameters other than snow and elevation band parameters.
2. Snowmelt project (RP+SP0): uses calibrated reference project at step (1) and calibrates only snow parameters.

3. Elevation band project (RP+SPE): uses calibrated reference project at step (1) and calibrates for snow and elevation band parameters.

In this paper, the effectiveness of above said SWAT model setups are tested to compute streamflow with snowmelt over the Himalayan River Basin. In SWAT model, ten elevation bands (E) can be set to better handle the snow cover and snowmelt in the mountains. Here, five sets of elevation bands (E= 2,4,6,8, and 10) have been considered to examine a suitable number of elevation bands for the study area. Last model setup (3) has only been applied in the snow-dominated sub-basins for which elevation cutoff point is >4000m and covers around 26.44% of basin (Table 6.2).

Table 6.2: Topographical characteristics of sub-basins. Shaded gray colored sub-basins are having snow dominance

Sub-basin	Elevation (m)				Sub-basin	Elevation (m)			
	Min	Max	Mean	St. dev.		Min	Max	Mean	St. dev.
1	2593	7096	5193.2	696.3	21	463	1646	978.3	241.2
2	2593	7892	4833.6	855.6	22	306	7515	1616.8	1309.2
3	1603	8042	4805.8	794.2	23	581	5760	2407.7	996.3
4	1611	7319	4490.1	922	24	461	2326	1156.2	267.3
5	831	8143	4390.4	1189.8	25	341	1793	874.4	289.8
6	829	8115	3352.2	1502.9	26	278	8055	2737.2	1684.1
7	1807	7362	4686.9	748.4	27	274	5830	1460.8	1076.9
8	1820	7275	4797.4	858.3	28	233	2117	826.5	397.2
9	670	3061	1589.3	464.2	29	208	2104	718.7	273.3
10	674	8032	3106.7	1665.2	30	216	1907	1003.5	385.7
11	1437	7351	3794.7	1219.1	31	322	1711	811.3	238.4
12	1443	7184	4734.4	947.5	32	238	1918	880	347.6
13	499	7806	3076.8	1330.2	33	326	5073	1280.7	664
14	493	2744	1305.5	398.8	34	188	1857	766.2	321.9
15	473	4016	1869.2	652.8	35	186	1280	499.2	265.7
16	472	2110	998.8	382.2	36	181	558	278.2	63.7
17	304	7924	1926.1	1531.4	37	136	811	238.6	133.6
18	405	2833	951.5	387.9	38	136	2577	524.2	411.9
19	404	7052	2413.3	1251.7	39	113	1857	457.6	349.4
20	508	2465	1178.1	317.2	40	400	2561	961.4	479.4

6.2.3 Calibration and Sensitivity Analysis

Model sensitivity and calibration are carried out using SUFI-2 algorithm inbuilt in the SWAT-CUP tool [9,273]. SWAT-CUP is an external parameter optimizing tool that lets the SWAT user to calibrate the model automatically with ease and efficiency. SWAT-CUP has been used extensively by the SWAT users worldwide [274]. In SWAT-CUP, there are several algorithms to optimize the model parameters, but the SUFI-2 method has been chosen because it is known to attain better calibration results than others for a given number of iterations [127]. Also, a large number of parameters can be calibrated with the SWAT-CUP making SWAT a very versatile and adoptive model [92]. In this study, SWAT parameters have been selected based on the past studies at this region and similar parts of

the globe [92,108,275,276]. In all, 37 parameters are selected: 27 for hydrological parameters related to the reference project, 7 for snow parameters and 3 for elevation band parameters. The list of selected SWAT parameters along with their range values are listed in Table 6.3.

Table 6.3: Description of parameters and their range considered for the first sensitivity analysis.

Parameters	Description	Range value	
		Min	Max
Reference Project (RP)			
ALPHA_BF.gw	Base flow alpha factor (days)	0	1
BIOMIX.mgt	Biological mixing efficiency	0	1
CANMX.hru	Maximum canopy storage	0	100
CH_K2.rte	Hydraulic conductivity in main channel	-0.01	500
CH_N2.rte	Manning's "n" value for the main channel.	-0.01	0.3
CN2.mgt	SCS runoff curve number	-0.2	0.2
DEEPST.gw	Initial water depth (mm) in the deep aquifer	0	50000
EPCO.hru	Plant uptake compensation factor	0	1
ESCO.hru	Soil evaporation compensation factor	0	1
EVLAI.bsn	Leaf area index for no evaporation	0	10
EVRCH.bsn	Reach evaporation adjustment	0.5	1
GW_DELAY.gw	Groundwater delay (days)	0	500
GW_REVAP.gw	Groundwater "revap" coefficient	0.02	0.2
GW_SPYLD.gw	Specific yield of the shallow aquifer (m3/m3)	0	0.4
GWHT.gw	Initial groundwater height (m)	0	25
GWQMN.gw	Threshold water depth for return flow in the shallow aquifer(mm)	0	5000
HRU_SLP.hru	Average slope steepness	0	1
OV_N.hru	Manning's "n" value for overland flow	0.01	30
RCHRG_DP.gw	Deep aquifer percolation fraction	0	1
REVAPMN.gw	Threshold water depth (mm) in the shallow aquifer to occur 'revap'	0	500
SHALLST.gw	Initial water depth (mm) in the shallow aquifer	0	50000
SLSUBBSN.hru	Average slope length	10	150
SOL_ALB(..).sol	Moist soil albedo	-0.5	0.5
SOL_AWC(..).sol	Water holding capacity of soil layers	-0.5	0.5
SOL_K(..).sol	Saturated hydraulic conductivity	-0.5	0.5
SOL_Z(..).sol	Depth from soil surface to bottom of layer	-0.5	0.5
SURLAG.bsn	Surface runoff lag time	0.05	24
Snow phase parameters (SP)			
SFTMP.bsn	Snowfall temperature (ºC)	-10	10
SMTMP.bns	Snowmelt base temperature (ºC)	-10	10
SMFMX.bsn	Maximum melt rate for snow during year	0	20
SMFMN.bsn	Minimum melt rate for snow during year	0	20
TIMP.bsn	Snowpack temperature lag factor	0	1
SNOW50COV.bsn	Snow water equivalent (mm) during the 50% snow cover	0	0.9
SNOWCOVMX.bsn	Snow water equivalent (mm) during100% snow cover	0	500
Elevation band parameters (SPE)			
SNOEB.sub	Initial water content in the elevation bands	100m (Constant for snow dominated sub-basins)	
PLAS.sub	Precipitation lapse rate	-100	1000
TLAPS.sub	Temperature lapse rate	-10	10

The one-at-a-time sensitivity analysis method [273] has been applied in this study. This method analyses the sensitivity of the SWAT model by changing a single parameter and keeping others constant. The sampling of the sensitivity process depends on the latin hypercube method [277]. To ensure the full range of variation within the sampled parameters, SUFI-2 divides user-defined input range into several subranges of equivalent probability. In this study, fifty runs [92] were executed for eight years (2000-2007) with initial four years (1996-1999) of warmup period to analyze the sensitive parameters. The implemented sensitive parameters for this study are listed in Table 6.4.

Table 6.4: List of parameters that display sensitivity to the hydrological system

Reference project			**Snow project**		
X_Parameter	t-stat	P-vale	Parameter	t-stat	P-vale
1_CN2	0.040	0.972	2_SMFMN	0.027	0.981
3_HRU_SLP	0.026	0.981	11_TIMP	0.004	0.994
5_EPCO	0.019	0.986	12_SMTMP	0.003	0.997
6_GW_REVAP	0.018	0.987	13_SNOWCOVMX	0.0025	0.998
7_SOL_ALB	0.010	0.993	16_SNOW50COV	-0.00004	0.999
9_SOL_AWC	0.005	0.996	18_SFTMP	-0.007	0.995
10_ALPHA_BF	0.004	0.997	22_SMFMX	-0.026	0.981
14_CANMX	0.0009	0.999			
15_ESCO	0.0008	0.999	**Elevation band project**		
17_REVAPMN	-0.002	0.998	Parameters	t-stat	P-vale
19_CH_K2	-0.012	0.992	4_TLAPS	0.0262	0.981
20_SLSUBBSN	-0.015	0.989	8_PLAPS	0.0086	0.994
21_CH_N2	-0.022	0.984			

*X_Paramere - where X denotes the rank of sensitivity.
*For most sensitive parameter t-stat value should be high and P-value should be low

SWAT-CUP allows users to select the sub-basin of their choice for calibration. Therefore, after sensitivity analysis, SWAT-CUP has been allowed to run for 500 run times with the sensitive parameters as recommended by Yang 2008 [127]. The process has been replicated for three iterations for each SWAT model setups and for five stream gauge stations. Reference project calibrations were performed separately for each gauging stations, propagating from upstream to downstream gauge stations. The calibrated parameters for upstream sub-basins were fixed during the further calibration of the downstream sub-basins. Thus, the heterogeneity among the sub-basins within the watershed has been maintained. In the snow project, calibrated parameters from reference project were transferred and only snow parameters were allowed calibrated using SUFI-2 algorithm. Similar to the snow project, elevation band project was allowed to use calibrated parameters of reference project and calibrated only for snow and elevation band parameters. All stream gauge stations have been used simultaneously during snow and elevation band project calibration. Elevation

band project was calibrated with the five set of elevation bands (E =2, 4, 6, 8 and 10) to examine the optimal number of elevation band for the considered study area.

In each project, calibrations were performed on a daily basis using the input data mentioned in Table 6.1. All projects were calibrated against observed streamflow (considering both runoff and snowmelt) for eight years (2000-2007) of time period. During parameters optimization with SUFI-2 algorithm, Nash–Sutcliffe Efficiency (NSE) was set as the objective function. The model performance was considered satisfactory if NSE ≥0.5. After calibrations, model performance was also assessed with the Percentage Bias (PBIAS) and Coefficient of Determination (R^2) between observed (O) and simulated (P) flow data.

$$NSE = 1 - \frac{\sum_{i=1}^{n}(O-P)^2}{\sum_{i=1}^{n}(O-\overline{O})^2} \tag{6.1}$$

$$PBIAS = \frac{\sum|O-P|}{\sum O} * 100 \tag{6.2}$$

$$R^2 = \left(\frac{\sum_{i=0}^{n}(O-\overline{O})(P-\overline{P})}{\left[\sum_{i=1}^{n}(O-\overline{O})^2 \sum_{i=0}^{n}(P-\overline{P})^2\right]^{0.5}} \right)^2 \tag{6.3}$$

6.2.4 Validation of Simulated Snow

Eight daily MODIS snow cover data MOD10A2 was used for snow validation. Here it is important to mention that no direct calibration of snow water equivalent (SWE) in the sub-basins have been performed. Because, to validate simulated snow on spatial scale, a very dense in-situ snow sampling is required, which is impossible for complex terrains like Himalayas [278,279]. However, remote sensed snow cover products like MODIS datasets are proving a very good spatial and temporal coverage of snow cover area [214,278]. Therefore, after the model calibration for streamflow, MODIS snow cover data was used to externally validate the simulated snow water equivalent.

The temporal comparison was performed between simulated SWE (mm) and MODIS snow cover factor (SCF %) on each snow-dominated sub-basins. This time series comparison could be informative about the status of sublimation and deposition process of snow in the study area. In the simulated results, increasing rate of SWE in the elevation

bands denotes deposition phase while decreasing rate denotes sublimation phase of snow in the sub-basins. Therefore, simulated deposition and sublimation phases should be examined with the increasing and decreasing rate of SCF respectively in the course of validation. Also, the spatial analysis compares snow presence and absence for a particular day: during minimum extent of the snow period i.e. end of snow sublimation season and maximum snow cover period i.e. end of snow depositing season. The ending month for deposition and sublimation phases of snow in a year are March and August [279] for Hindu-Kush Himalayan Region. The sensitivity of MODIS product to detect snow was estimated to be about 15 mm of SWE [280]. Therefore, 15 mm of SWE threshold has been taken to denote snow and no snow.

6.3 Results

6.3.1 Model Performances

The important parameters identified through sensitivity analysis (from the initial list given in Appendix I) have been presented in Table 6.4. Out of the thirty-seven initially selected parameters, twenty-two were found most sensitive based on the t-stat and P-value for daily simulation. There were thirteen parameters from reference project while the majority of the elevation band and snow project parameters were kept retained in this list for the same reasons.

The calibrated parameters values for each sub-basin, progressing from upstream to downstream gauge stations are given in Table 6.5.

The calibration results for different sub-basins and for each model setups are presented in Table 6.6. The statistical performances of the reference project (RP) are comparatively worse than snow project and elevation band projects. For RP, basin mean NSE is 0.57 while PBIAS and R^2 are 44.72% and 0.80 respectively. Snow project (RP+SP0) slightly improves the mean basin performance statistics (with NSE = 0.74, PBIAS = 39% and R^2 = 0.87) than reference project. Elevation band project (RP+SPE) outperforms to both reference project (RP) and snow project (RP+SP0) when compared with performance statistics for this region. The performance statistics for all elevation band projects (RP+SPE) are very close to each other, but RP+SP2 and RP+SP4 show better basin average PBIAS, 7.48 and 11.9 respectively than others. Also, the NSE for elevation band projects is consistent (>0.82) for each time, indicating homogeneity in the mountains snow dynamics. The NSE, R^2 and

PBIAS are getting improved when moving from upstream to downstream gauge sites, thereby creating consistency in the performance at the basin scale. The NSE for sub-basins Arughat-13 and Betravati-23 (figure 6.1) is ≤ 0.5 for reference project which improves to >0.7 for downstream sub-basins Narayanighat-36 and Triveni-39. The maximum statistical improvement is found for upstream sub-basins (13, 23, and 25) upon considering the elevation band approach. The performance in terms of PBIAS is more consistent in the sub-basins for elevation band projects except at the Betravati-23, where it is found to be 40.9%. It is worth to mention that the elevation band projects not only improves the performance in the snow dominated sub-catchments (13, 23, and 25) but it also improves to down stream outlets (sub-basin Triveni-39), located around 400 km into the plains where it improves the NSE from 0.6 to 0.8 while PBIAS changes from 41.3% to 4.4%.

Table 6.5: Calibration range and calibrated parameter values for each model setup

Parameters	**Range**	**Fitted Values**				
Reference Project		Sub_13	Sub_23	Sub_25	Sub_36	Sub_39
r_CN2	-0.2/0.2	0.18	0.14	0.18	0.18	0.20
a_ALPHA_BF	0/1	0.15	0.19	0.54	0.59	0.80
a_GW_DELAY	-30/60	-14.50	-27.01	-28.58	1.37	-7.49
a_GWQMN	-1000/1000	-273.83	-571.91	-660.41	-561.55	-566.06
v_CANMX	0/30	12.78	27.88	27.02	0.67	0.46
v_CH_N2	0.01/0.3	0.12	0.05	0.04	0.07	0.16
v_CH_K2	0.01/500	346.99	266.50	262.36	214.91	271.93
v_ESCO	0.75/0.95	0.93	0.95	0.87	0.89	0.90
a_GW_REVAP	0.02/0.2	0.10	0.06	0.13	0.08	0.11
a_REVAPMN	-750/750	-733.05	88.29	256.42	132.43	-146.36
r_SLSUBBSN	-0.2/0.2	0.09	-0.04	0.03	-0.12	-0.02
r_SOL_AWC	-0.1/0.1	-0.11	-0.04	0.05	0.03	-0.02
r_HRU_SLP	-0.2/0.2	-0.08	0.06	0.01	-0.01	-0.06
Snow Project	Range	Parameters calibrated for all gauge point simultaneously				
v_SFTMP	-5/3			1.74		
v_SMTMP	-1/5			4.17		
v_SMFMX	2/5			2.98		
v_SMFMN	0/3			0.06		
v_TIMP	0/1			0.03		
v_SNOCOVMX	20/75			30.11		
v_SNO50COV	0.3/0.9			0.73		
Elevation band Project	Range	Elv_2	Elv_4	Elv_6	Elv_8	Elv_10
v_SFTMP	-5/3	-3.86	-1.55	-3.17	-2.51	-1.93
v_SMTMP	-1/5	0.84	3.59	4.90	3.43	3.12
v_SMFMX	2/5	2.85	1.95	1.82	2.44	2.14
v_SMFMN	0/3	1.05	2.01	0.89	1.44	2.74
v_TIMP	0/1	0.01	0.33	0.29	0.01	0.01
v_SNOCOVMX	20/75	61.33	72.54	48.75	70.95	70.68
v_SNO50COV	0.3/0.9	0.45	0.61	0.47	0.50	0.66
r_TLAPS (default value=-6)	-2/2	-1.36	-0.72	-0.74	-1.06	-1.06
r_PLAPS(default value=200	-2/2	0.22	-0.09	0.49	0.35	-0.44

In Table 6.5, [v]Parameters will be replaced with new one and [r]parameters (please see Abbaspour et al. 2007 for deatil) that will changing relatively from given value (here from the default value) at each number of simulation.

Table 6.6: Calibration performance for different model structures and for all gauging sites at a daily time step

Gauge sites	Stat-Index	HP	HP+SP0	HP+SP2	HP+SP4	HP+SP6	HP+SP8	HP+SP10
	PBIAS	46.8	36.7	7.1	8.1	11.3	-3.4	1.2
13	NSE	0.43	0.74	0.83	0.85	0.88	0.85	0.87
	R2	0.69	0.88	0.83	0.89	0.9	0.89	0.89
	PBIAS	57.2	47	27.7	20.3	39.9	40.9	39
23	NSE	0.32	0.65	0.75	0.84	0.69	0.7	0.71
	R2	0.72	0.85	0.81	0.87	0.86	0.87	0.87
	PBIAS	39.7	36.9	6.8	19.3	16.5	13.6	19.4
25	NSE	0.74	0.79	0.82	0.84	0.84	0.86	0.85
	R2	0.87	0.88	0.83	0.87	0.86	0.87	0.88
	PBIAS	38.6	35.8	-8.6	0.4	-3.4	-0.2	12
36	NSE	0.73	0.81	0.88	0.9	0.89	0.91	0.92
	R2	0.9	0.94	0.89	0.91	0.9	0.91	0.93
	PBIAS	41.3	39.5	4.4	11.4	8.5	10.8	20.3
39	NSE	0.64	0.7	0.81	0.81	0.82	0.83	0.82
	R2	0.84	0.88	0.84	0.86	0.85	0.87	0.88
	PBIAS	44.72	39.18	7.48	11.9	14.56	12.34	18.38
Basin Mean	NSE	0.572	0.738	0.818	0.848	0.824	0.83	0.834
	R2	0.804	0.886	0.84	0.88	0.874	0.882	0.89

6.3.2 Snow Simulation

Elevation band project has improved the streamflow simulation in this study area. Here, an attempt has been made to further evaluate the temporal and spatial variation in the SWAT simulated SWE externally. The spatial variation is being evaluated by comparing MODIS snow cover on 20th March and 20th August (2004), which is roughly the end season for snow deposition and sublimation phase respectively. For example point of view, the extent of snow cover equivalent to SWAT simulated SWE in the elevation bands for snow-dominated sub-basin-1 have been shown in the Figure 6.2. The SWAT simulated snow cover pattern is fairly consistent with the MODIS snow cover area. However, SWE based snow cover is underestimating for sublimation phase Figure 6.2(a) and overestimating during the deposition phase. Also, SWE based snow cover shows slight inconsistency in the uppermost part of the sub-basin. Therefore, additionally independent calibration for snow water equivalent (SWE) could improve the model results for this region.

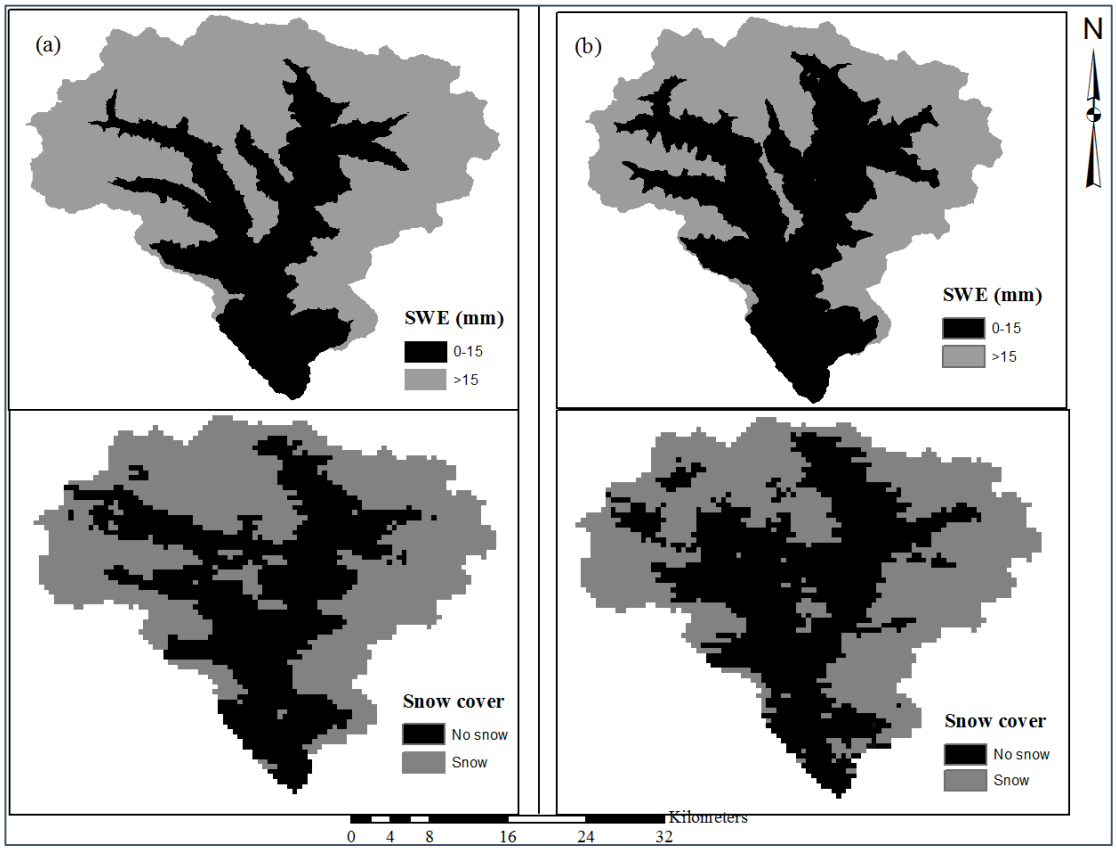

Figure 6.2: Snow comparison during (a) sublimation phase, 20th August 2004 and (b) deposition 20th March 2004

The temporal analysis has been accomplished with a stack area time-series plots (Figure 6.3) between MODIS snow cover factor (SCF)-percentage of basin area covered with snow and SWAT simulated SWE. For example point of view, the stack area plots have been schemed only for first five snow dominated sub-basins (Figure 6.3). For most of the time, SWAT simulated SWE reflects the rise and fall pattern alike MODIS SCF. The stack area graphs also show that SWE can depict the deposition phase (with the rising dark area peaks) and sublimation phase (with the falling dark area peaks). SWAT simulated SWE is almost zero during sublimation phase for sub-basin-2 and sub-basin-4, while at the same time MODIS shows a significant SCF. Therefore, SWAT has limitation to capture the sublimation phase SWE in the snow dominated sub-basins.

6.4 Discussion

6.4.1 Sensitivity Analysis and Calibration

Twenty two parameters are considered to be important by sensitivity analysis (Table 6.4). The parameters are found more or less same as other snow related studies, especially Pradhanang et al. 2011 [250] and Meng et al. 2015 [276] who simulated snowpack development and streamflow simulation in the snow-dominated watersheds. In the reference project (RP) parameters have been calibrated separately for each stream gauge site, moving from upper to lower reach along with transferring the calibrated parameters to the related sub-basins associated with that stream gauge site. This procedure maintains the heterogeneity between the sub-basins and makes possible to use relative parameters like CN2, SOL_ALB and SOL_AWC in the most distributed way within the sub-basins.

In the reference project, CN2, CH_N2, SOL_AWC, and CANMX are the prime parameters responsible for the water balance and runoff generation in a particular instance at daily time step. The CN2 is inversely proportional to the soil moisture retention (S), that means high CN value will have low permeability and vice versa. From the Table 6.5, the CN value for all calibrated sub-basins is positive CN value changes relatively from the default HRU value [273]. This implies that CN value will be greater than the default HRU values. The CN value is greater for stream gauge station Triveni-39 than others, which drains the mid-hills and has the majority of the basin area. It shows that the mid-mountains are less permeable and will generate more runoff compared to headwater areas.

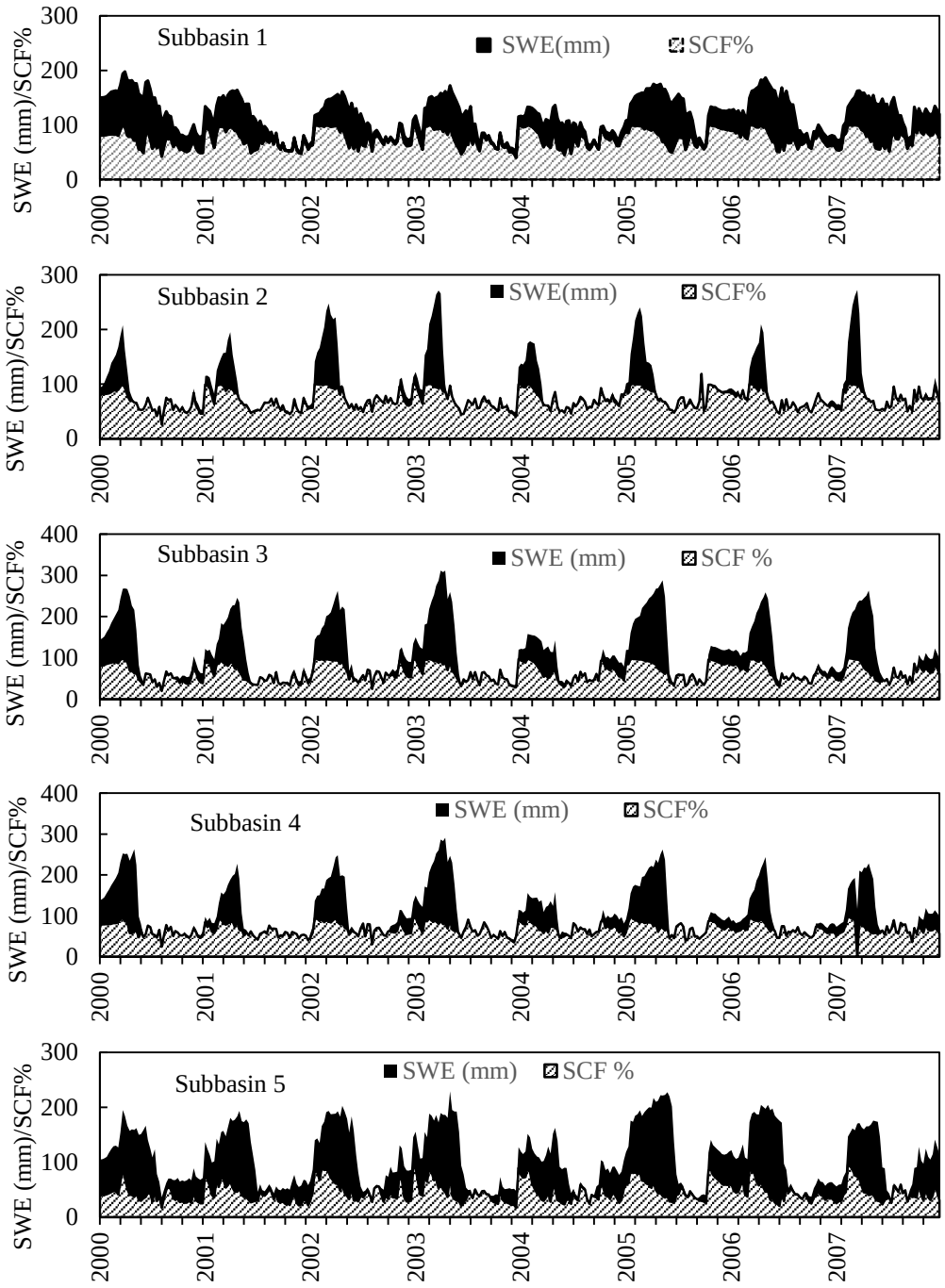

Figure 6.3: Stacked area plot for first five snow-affected sub-basins between the snow-cover factor (SCF %) and snow water equivalent [SWE (mm)] at weekly time interval

The Manning's 'n' value for the channel (CH_N2) is responsible for flow routing in the stream channels. The mean CH_N2 value of hilly stream gauge station Arugat-13, Betravati-23 and Kumalgaon-25 is more than in the stream gauge stations (Narayanighat-36 and Triveni-39) falling in the plain area. This is due to the floodways channels covered with timber and brush vegetation in the hilly part of the basin. Available water capacity for soil layers (SOL_AWC) is negative for the stream gauge sites Arughat-13 and betravati-23 while positive for mid mountain sites Kumalgaon-25 and Narayanighat-36. It indicates that mid mountain areas are have more water retention capacity than headwater locations. This may be due to alluvial soil presence in the mid hills which retains more water than glacial soil present in the upper part of basin. The value for the maximum canopy storage (CANMX) is greater for mountain sub-basins than plains. That implies, mountains are prone to canopy storage than and plains due to presence of broadleaf forest.

SWAT snow project setup uses temperature-index based snow modeling method along with the elevations bands approach. Elevation band setup of SWAT re-distributes the calculation on different sets of mean elevation bands for each sub-basins. There are eight parameters related to snow project and remaining three for elevation band project. The parameters found sensitive to snow and elevation band project are given in Table 6.4. In the Himalayas, mountains >4000m of elevation are always covered with snow. Thus, initial snow water content is always greater than zero [108,236] for sub-basins falling on these areas. Therefore, SNOEB have been set to 100m for all sub-basins having elevation ≥ 4000m. After accomplishment of snow (RP+SP0) and elevation band projects (RP+SPE), a significant improvement in results of RP+SPE project (for elevation bands 2-4 shaded results in Table 6.6 shows best results) has been found than RP+SP0 project. Between these two projects, SMFMN value has been increased from 0.06 to 1.05 while SMFMX is almost constant (~2.8). Also, the TIMP has seen a dip from 0.03 to 0.01 while SMTMP and SFTMP have been decreased from 4.17^{o}C to 0.84^{o}C and 1.74^{o}C to -3.86^{o}C.

The statistical performances of different SWAT setups reveal the drawbacks of calibrating SWAT model only with the reference or snow project parameters when the part of the basin area is covered with snow falling in mountainous areas. Therefore, the impact of snow model setups with a different number of elevation bands (E) has also been tried to address. The streamflow simulation results show that elevation band approach with two to four elevation bands does well in this region. Improvement in the simulated streamflow results (Table 6.6) after the introduction of elevation band parameters TLAPS and PLAPS

shows that the temperature and precipitation gradients are significant in this region. Thus, only snow parameters are not very useful at a basin scale. The TLAPS for RP+SP2 elevation band project (Table 6.6) is relative -1.36 (that mean TLAPS is decreased by 136 percent from default value 6, calculates to -2.16^{o}C/km) while PLAPS is relative 0.22 (that means PLAPS is increased by 22 percent from default value 200, calculates to 244 mm/km).

6.4.2 Validation of SWAT Simulated Snow

The addition of elevation band approach in the SWAT snow simulation setup has improved the streamflow results for each stream gauge sites. Therefore, it is assumed that it has also improved the hydrological components especially snowpack dynamics. Although, no directly calibration for the snowpack SWE has been carried out due to lack of in-*situ* snowpack data for the basin. But simulated snowpack SWE records have been externally compared with the MODIS 8-dalily snow cover product MOD10A2.

Figure 6.2 shows a consistent pattern between SWAT and MODIS snow cover. During sublimation phase, SWAT underestimates the snow cover area compared to MODIS, and overestimates during deposition phase. It may be due to lack of direct calibration for snowpack and assigning the unrealistic value of snow parameters like SMTMP, SMFMX and SMFMN. Therefore, this will lead to high and low snowmelt contribution in streamflow for sublimation and deposition phase respectively.

The time series analysis between SWE and SCF (Figure 6.3) reflects that sub-basins 1, 3, 4 and 5 are accurately depict the pattern throughout the year with few errors. But, sub-basin 2 shows an off track pattern between SWE and SCF during snowmelt season (sublimation phase) for all years. It may be due to the subsequent impact of human interventions such as presence of a reservoir (Figure 6.1) for hydropower generation in the study site. Also, it may be attributable to no direct calibration for snow pack parameters. A significant difference in the magnitude of the SCF and SWE has been found throughout the time series of all sub-basins. This may be due to the varying snow depth for same SCF. Because SWE alters due to increasing or decreasing snow depth in the elevation bands, but SCF will remain unchanged, if there is snow depth equivalent to >15 mm SWE in the MODIS product. However even with all these limitations the model performs well in depicting the snow accumulation and snowmelt process throughout the year.

6.4.3 Impact on the Hydrological Cycle

In this section, the changes in the SWAT water partitioning due to modifications in the snow dynamics caused by different SWAT setups has been discussed.

Introduction of elevation band based snow-model setups and their associated parameters such as temperature and precipitation lapse rate, alter the gauged volume of precipitation received by the snow dominated sub-basins. Figure 6.4 reflects the percentage of variation in the mean annual precipitation (%Var.) between different SWAT model setups. Changes are significant for all snow dominated sub-basins except for sub-basins 1, 8, 12 and 23 where %Var is less than 15% between reference and snow (R/S) and elevation band project (E). It has been noted that all snow-dominated sub-basins are under estimating annual precipitation without the use of elevation bands except in sub-basin 12. This may be due to unique grids of APHRODITE precipitation product for the entire sub-basins, which fall in the valleys rather than the mountain peaks. For instance, elevation in the sub-basin 5 varies from 831m to 8143m and if unique APHRODITE grid will fall on ridge (8143m), precipitation will be larger for elevation band project than reference and snow projects. Similarly, for underestimation, the APHRODTE precipitation grids will be falling close to the minimum elevation area (valley, 831m) in the sub-basin. Also, precipitation lapse rate are calibrated for all snow dominated sub-basins simultaneously and therefore it may not be feasible individually. The trend in the percentage variation (%Var) between yearly R/S and E precipitation positively increases with the amount of rainfall (Figure 6.4). This means precipitation lapse rate has more impact on sub-basins receiving significant amount rainfall, which is obvious.

The presence of snow cover in the sub-basins affects the water balance components. The water balance components differ from one project to another, especially precipitation, Evapotranspiration (ET), surface runoff (SQR) and infiltration (INFL) (INFL may be infiltration or accumulated snow depending upon the threshold SFTMP). Figure 6.5 illustrates the variation in the annual water partitioning for each sub-basins. In Figure 6.5, reference and snow project reflects imbalance partitioning of precipitated water in terms of high ET and SQR and pretty low INFL. Conversely, elevation band project improves the results by assigning a significant percentage of precipitated water to infiltration (INFL).

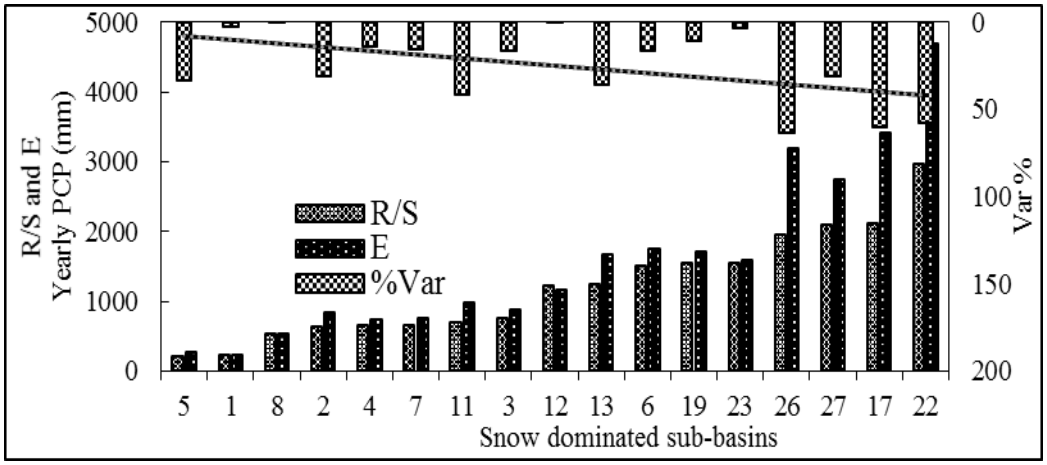

Figure 6.4: Plot between mean annual precipitation (P) for reference project (R), snow project (S) and elevation band project (E). Also, in secondary axis percentage of variation (Var%) between R/S and E for snow dominated sub-basins

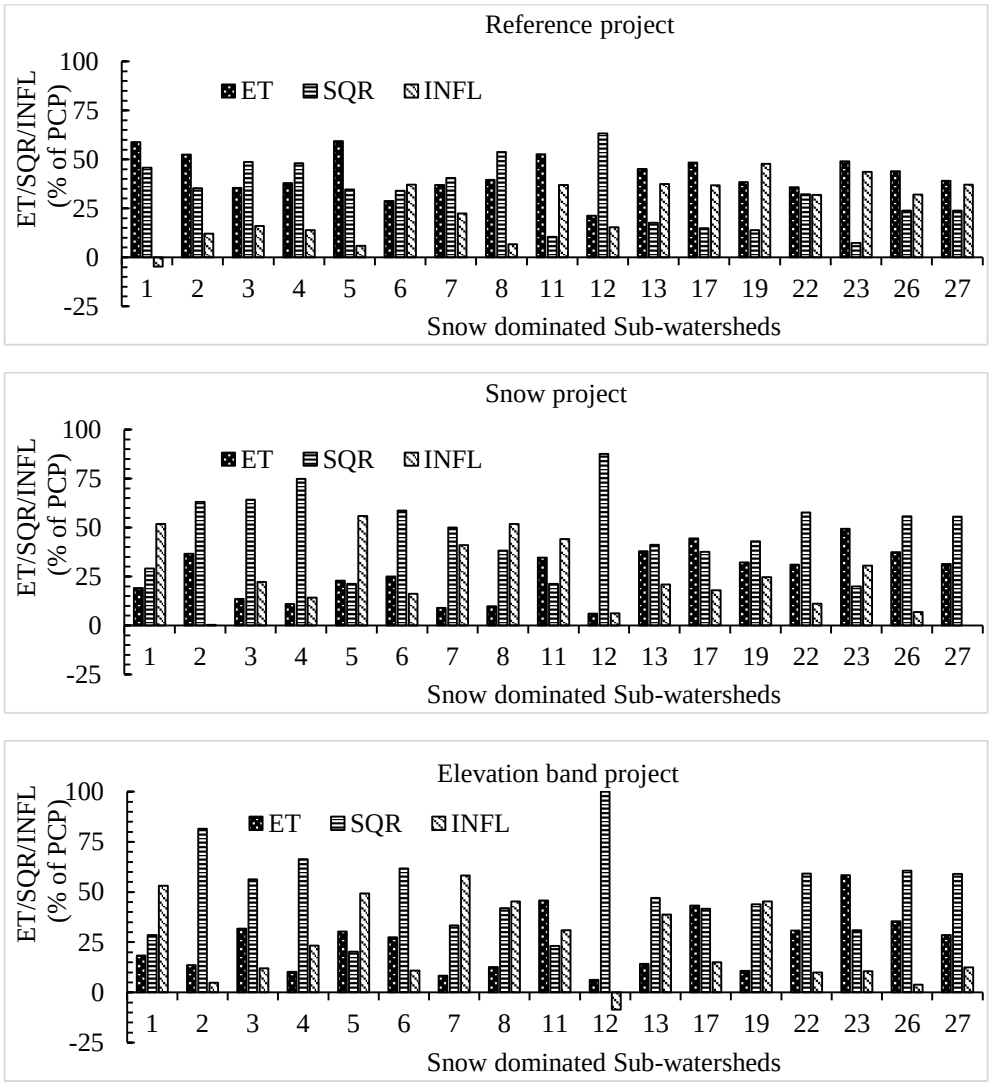

Figure 6.5: Partitioning of mean annual precipitation (P) into hydrological components

Figure 6.6 shows percent variation of ET, SQR and INFL between reference project and elevation band project. The average variation for ET is more than -40 percent and -22 percent for INFL. Negative (-ve) percentage variation for ET and INFL shows decrease in the ET and INFIL values when shifting the model setup from reference to elevation band project. Conversely, the SQR shows average variation more than 90 percent that means elevation band project imparts the differences between observed and simulated streamflow by adding snowmelt water into the runoff. Changes in the annual value of water balance component mainly attributed due to snow dynamics and present disparities based on the seasonality. It is worth to note that all snow-dominated sub-basins fall in the peaks of Himalayas where SFTMP remains below threshold limit (<0^{o}C) for most of the year. Therefore, major part of precipitation water in the snow-dominated basins will convert into the snow during this time.

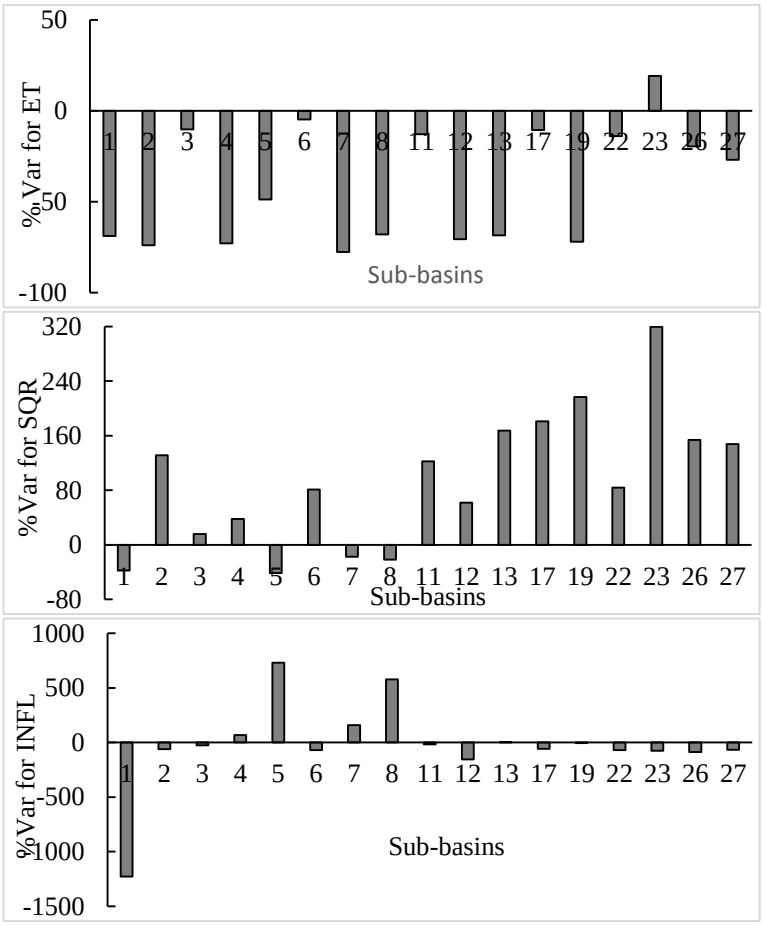

Figure 6.6: The percentage variation of ET, SQR and INFL. between reference and elevation band projects

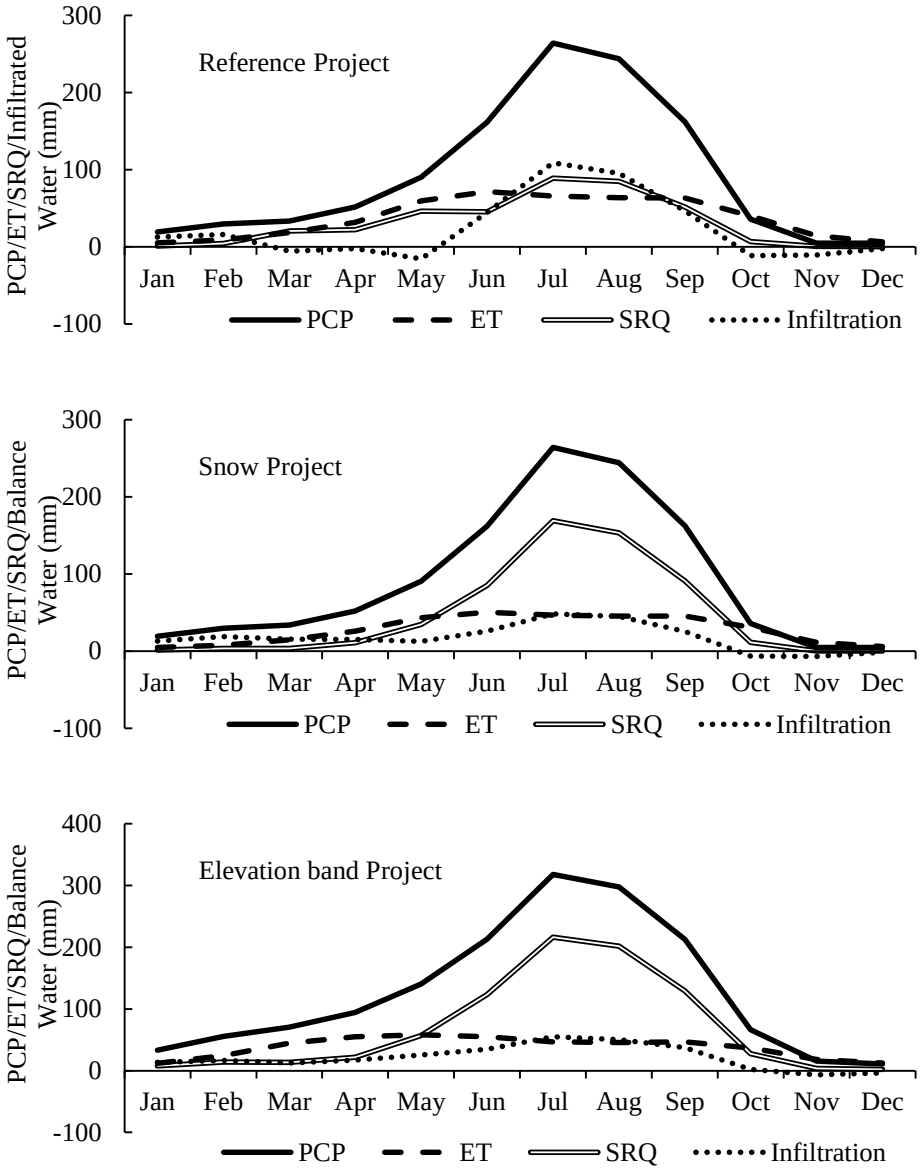

Figure 6.7: Weight average monthly mean values of water balance parameters for snow dominated sub-watersheds over 2000-2007

Figure 6.7 illustrates the weighted average hydrological components for snow-dominated sub-basins at a monthly time step and for different SWAT model setups. It clearly reflects a strong seasonal as well as model setup effect on the hydrological components. The reference and snow model setups exhibit negative infiltration for summer and post monsoon months (October to December). Also, both reference and snow projects reveal almost equal magnitude for SQR and ET. Introduction of snow model setup with elevation bands reduces the magnitude of ET and changes the infiltration to positive for all months. In the elevation band project, ET decreases mainly due to drop in air temperature resulted by use of TLAPS. The elevation project results are comparable with the yearly hydrological component results published by [281]. Also, The average annual ET for the snow sub-basin is 456mm which is very close to 500mm reported by Lambert and Chitrakar 1989 [282].

As discussed, modification in the model setups changes the water balance partitioning from upstream to downstream. Section 6.3.1 shows that model performance improves by using the snow model setup with elevation bands. For instance, the daily average hydrograph (2000-2008) for different model setups and for each gauging stations a have been presented in the Figure 6.8. The simulated hydrograph for RP+SP4 give better fit to the observed streamflow than RP and RP+SP0. The RP and RP+SP0 model setups always underestimate the observed streamflow. The RP+SP4 model setup shows better hydrographs for high flow during monsoons- except for Betravati (23) and Kumalgaon (25) where stream flows are underestimated for all model setups. Although, the low stream flows (during off season) are not improved by using RP+SP4 model setup and therefore needed a specific attention in further studies. The temperature and precipitation lapse rates varies spatially and seasonally in the alpine Himalayan region [224,283–285]. Therefore, use of monotonic temperature and precipitation lapse rate, as in SWAT, may introduce to erroneous modeling results [92].

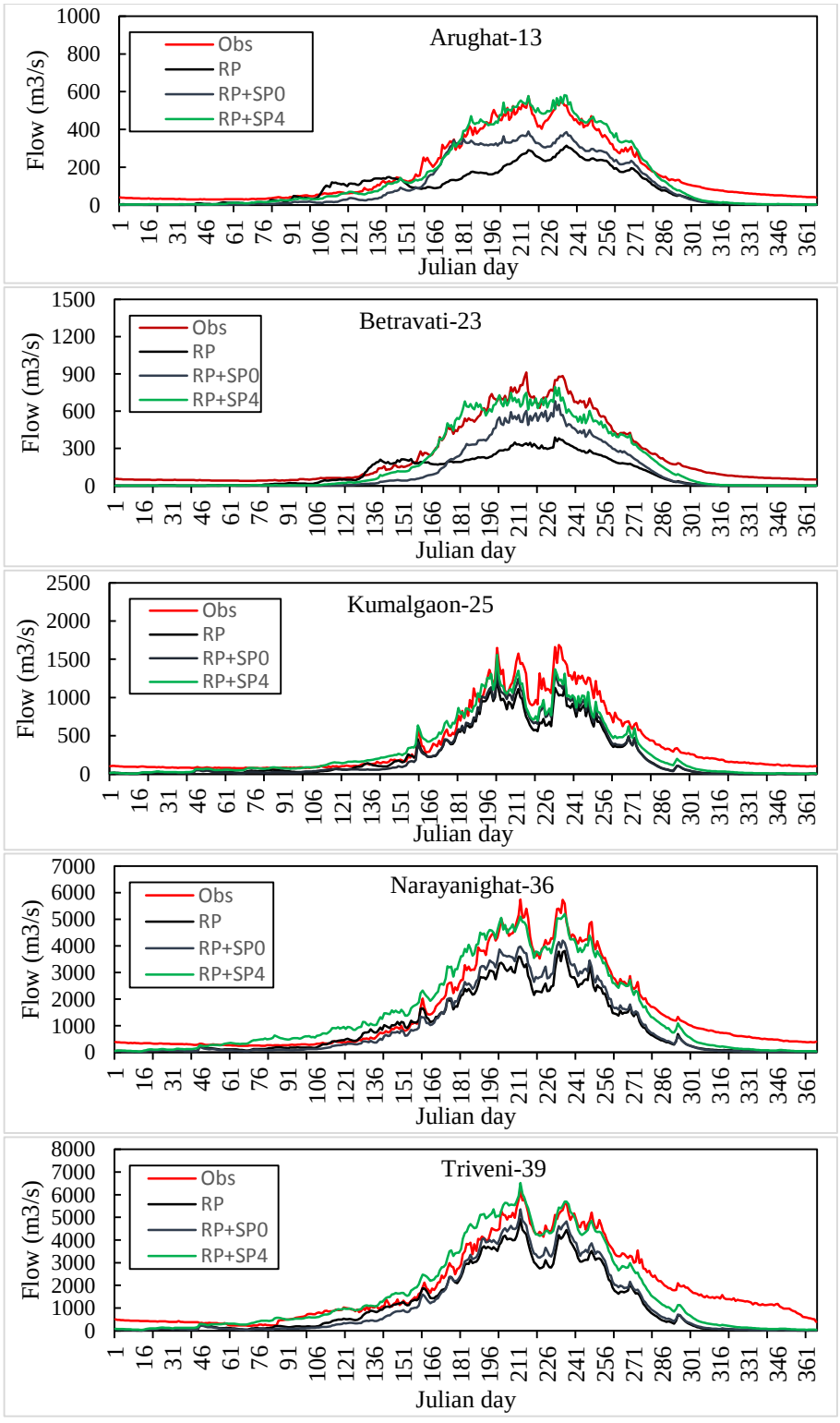

Figure 6.8: Daily average time series (2000-2008) for 5 gauging stations

6.5 Summary

Assessment of available water resources in the heads of alpine Himalayan region is crucial for planning and management in the South-East Asia. Diverse topography and climatology of along with variability of surface runoff, snow accumulation and snowmelt from high mountains simultaneously offer a challenging task to model hydrological processes in this region. In this study, different modeling routines available in the SWAT model have been tested to simulate streamflow and snow cover dynamics over the alpine Himalayan River Basin Gandak. Based on the study, the following interpretation have been drawn-

- The evaluation of the three SWAT modeling routines viz. reference project (RP), snow project (RP+SP0) and elevation band project (RP+SPE) highlight that inclusion of snow project parameters alone fail to improve the modeling results of the reference project. However, addition of lapse rates parameters (TLAPS and PLAPS associated with the elevation band project) in the snow project greatly improves the modeling results of snow-dominated sub-basins. The effect of elevation band project for the upper Himalayan sub-basins (snow dominated) has a positive impact on the modeling results at downstream sites.
- The lapse rates in the Himalayas changes with the altitude. In the SWAT model with the elevation band project, one need to choose the suitable number of elevation bands (E) that alters the lapse rate based on the mean altitude of the area. For this region, two to four elevation bands are found best for hydrological modeling. Increase beyond eight elevation bands modeling does not result in better simulations but may serve better for spatial snow cover mapping.
- The elevation band project affects the water portioning especially in the snow-dominated sub-basins. The results show that annual precipitation has increased due to the monotonic spatiotemporal lapse rates for all snow-dominated sub-basins. Also, elevation band project increases runoff and modifies water balance for each affected sub-basin. However, evapotranspiration decreases for elevation band project than reference and snow project under the effect of snow cover. The elevation band project shows more accurate partitioning of precipitated water into the hydrological comments and these are consistent with the findings of Andermann et al. (2012).

- SWAT simulated snow (SWE) has been compared with the MODIS snow cover data to assess its accuracy. The spatial comparison between MODIS and SWAT snow cover (based on the SWE in the elevation bands) confirm the good agreement in the spatial pattern for snow sublimation and deposition phases. The time series comparison between SWE and SCF reveal that SWAT is able to depict the variation in the snow dynamics for the region. Although, the reservoirs in the upper part of the basin exist for hydropower generation through streamflow, they have a limited impact during dry season, but they affects the snow simulations for few sub-basins. Therefore reservoir operation data should be taken into account for hydrological modeling.

This study highlighted the effect of different modeling routines to simulate snow dynamics and streamflow over the alpine Himalayan region. The use of elevation band approach is very meaningful for streamflow as well as snow cover representation. Therefore, it is recommended to implement SWAT model with snow modeling routine along with appropriate number of elevation bands in this region.

Chapter 7

Streamflow Simulation Using TRMM 3B42V7 Precipitation Product

In this chapter, the accuracy of gauge adjusted satellite precipitation estimate (TRMM 3B42V7) is evaluated to simulate the streamflow using five stream gauge stations for the entire river reach. Thereafter, the statistical performance between simulated and observed streamflow has been worked out for various rainfall intensity classes to see the relevance of TRMM 3B42V7 product for different kind of water management practices over the area.

7.1 Introduction

People and species living in mountains and downstream areas are frequently confronted to extreme hydrological events (floods and drought) [286,287]. In the case of Himalayan areas, people deal with these hostile events by accepting the losses and modifying their livelihood activities. Himalayan glaciers store the water in the form of snow and release it slowly during the dry season. Glacier melt water contributed to the river flow is vital to provide supplemental irrigation and drinking water during the non-monsoon period. Therefore, these two extreme discharge events pertain vulnerable situations. For example, if high- flow events (flood) are sudden, it can put living beings at risk. Conversely, low-flow events (drought) conquer slowly and affects a vast area. In results, the economic losses are huge for drought than flood situations [288,289]. Therefore, hydrological simulation of these extreme events is crucial to dilute their hazardous magnitude by suitable structural and non-structural measures [290].

Precipitation is the essential forcing for hydrological models. Reliable quality of rain and snow data is inevitable for model calibration, forecast, and simulations. In many parts of the globe, especially in the developing countries as well as for trans-boundary basins, obtaining rain gauge data is very challenging due to technical or administrative reasons [154,155]. The data exchange is even more difficult when needed in real-time for flood related studies [291]. Also, in the Himalayan region, precipitation estimates are subjected to significant

uncertainty due to inadequate rain gauge network to capture variability in these terrains [293]. Also, there is an addition in error by fault in the measuring device, human operation, and data transmission. Therefore, traditional rainfall records are susceptible to error and incomplete throughout time series for these regions.

In a view such difficulties remotely sensed data had proved its usefulness. Remote sensed precipitation products are more attractive input for large-scale water resource modeling [158,292]. For geographical coverage between latitude: 50°S - 50°N and longitude: 180°W - 180°E, such data is available by TRMM mission at no cost. TRMM mission has started in 1998 by the US and Japanese space agencies. There are several products of TRMM mission, but TRMM 3B42 (3-hourly, 0.25° gridded and gauge calibrated rainfall product) is mostly suitable for hydrological studies due to its high spatial and temporal resolution.

Numerous case studies have been conducted to compare the TRMM 3B42 V6 and V7 products with rain gauge data [293,294]. Recently several similar case studies have been conducted on Indian continent including Himalayas [161,162,165,166,171,172,294]. TRMM precipitation product has also been successfully used as an input for many hydrological models [138,158]. In the Himalayan region, suitability of TRMM precipitation product is yet to be evaluated for extreme hydrological events for most of its river basins.

In this study, our focus is to analyze the latest TRMM 3B42V7 precipitation product for hydrologically sound Himalayan region. The special emphasis is in the Gandak River Basin- falling above Triveni-39 gauge site (Figure 7.1) which causes flood and drought in the Bihar, India and Tarai portion of Nepal. To the best of our knowledge, no study has been conducted to see the quality of TRMM 3B42V7 product for simulation hydrological extremes (flood and drought) for this particular area. The satellite-based TRMM precipitation products TRMM 3B42V7 and CMROPH have already been compared in chapter 4. The study revealed that TRMM 3B42V7 has better statistical score than CMROPH. But, one still need to see the performance of TRMM 3B42V7 product for hydrological simulations.

7.2 Data and Methodology

7.2.1 Data

River Discharge Data

In the present study, river discharge data for five stream gauge (Figure 7.1) sites was collected from two countries, India and Nepal. Daily discharge data for a single gauge site at Triveni-39 (2000-2012) was collected from Central Water Commission, Government of India. However, stream gauge data for reaming four stream gauge sites [Arughat-13 (1964-2010), Betrawati-23 (1977-2010), Kumalgoan-25 (1996-2010), Narayanighat-36 (1963-2010)] were collected from Department of Hydrology and Meteorology, Government of Nepal. The geographical position of stream gauge sites and their contributing area is given Table 7.1.

Table 7.1: Analyzed stream gauges in the Gandak river basin

No.	**Gauge name**	**Position (degrees)**		**River**	**Catchment (Km2)**
		Latitude	Longitude		
13	Arughat	28.05	84.82	Burhi	3812.4
23	Betravati	27.96	85.17	Trisuli	3428.3
25	Kumalgaon	27.88	83.80	Kaligandaki	10639.3
36	Narayanighat	27.70	84.43	Narayani	31716.3
39	Triveni	27.45	84.97	Gandak	36373.8

Meteorological Data

In the present study, the gridded ($0.25^o \times 0.25^o$, Figure 7.1) daily gauge adjusted TRMM precipitation product 3B42 V7 data for Himalayan River Basin Gandak has been downloaded from NASA's online visualization system *TOVAS*. It allows the user to subset the data spatially and temporally and provides outputs in ASCII, NetCDF, and HDF file format. Ten years of TRMM 3B42 V7 data (from 2000-2010) have been downloaded in the NetCDF file format. Also, 3-hourly 3B42 data has been accumulated from 03UTC of the previous day to 06UTC of next day to get daily data at the basin's local time 8:30 AM (example is provided in chapter 4, table 4.7). The daily climatology (Wind Speed, Temperature, Relative humidity, and Solar radiation) data were taken from Climate Forecast System Reanalysis (CFSR) available at Global weather data for SWAT (http://globalweather. Tamu.edu/) since 1979-Present [257,295,296].

Physical Data

Digital Elevation Model (DEM) is the key input in SWAT. Slope, basin and sub-basin area, field slope length, river reach length and other topographical parameters are being calculated by SWAT model using DEM. Similarly, the calculation of channels parameters viz. channel width, channel length, channel depth and channel slope also lie on input DEM. In chapter 5, the effect of DEM grid size data on various topographical parameters have been presented. In this study, SRTM 90m V4.1 DEM (downloaded from the site http://srtm.csi.cgiar.org) have been used to set up our SWAT model.

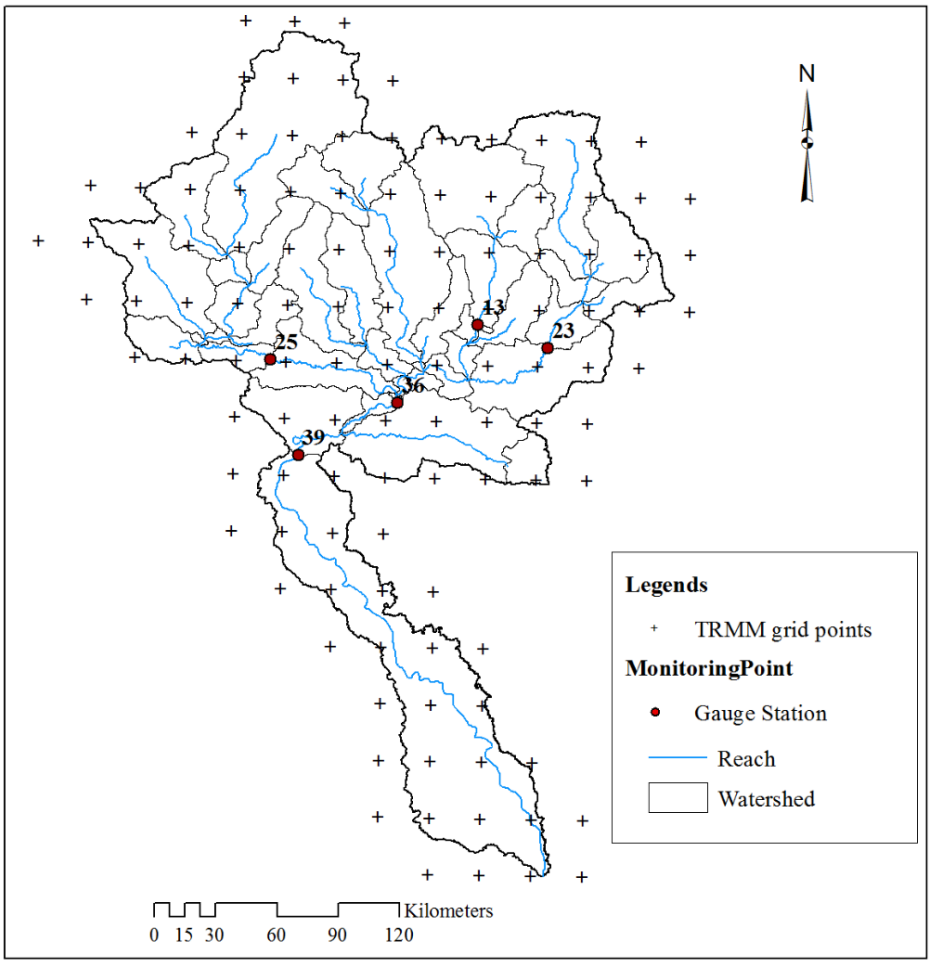

Figure 7.1: Location map of study area with TRMM grid points

The accuracy assessment for different global DEMs available for study area has been accomplished in Chapter 4. The curve number (CN) is an index to divide precipitated water into runoff and infiltration after subtracting initial losses, which depends on the slope, Land use and soil data. For this study, land use map have been taken from GlobeLand30 [131]. The GlobalLand30 land cover data can be accessed from http://www.globallandcover.com. However, 30 arc-second rasterized FAO soil map (downloaded from http://swat.tamu.edu/docs/swat/india-dataset/2012/soil_HWSD_FAO.7z) are used for soil characteristics information.

7.2.2 Description of SWAT model

SWAT is a physically based, semi-distributed, continuous hydrological model [213,232,274]. It simulates different hydrological components by solving process-based equations. Within the watershed, SWAT maintains the heterogeneity by dividing the whole basin into different sub-watershed and then into various Hydrological Response Units (HRUs) based on the similar threshold for land use, soil, and slope. SWAT counts runoff at each HRUs and then routes it towards outlet by using either variable storage or Muskingum method [297]. The basic equations governing hydrological processes by SWAT model are described below.

The SWAT model uses the water balance approach (equation 7.1) to simulate various hydrological components [213]. The equation is expressed as:

$$SW_t = SW_0 + \sum_{i=1}^{t} (R_{day} - Q_{surf} - E_a - W_{seep} - Q_{gw}) \quad (7.1)$$

Where, SW_t is change in soil moisture, SW_0 is the initial soil moisture, R_{day} is the rainfall on current day, Q_{suf} is the surface runoff, E_a is the evaporation losses, W_{seep} is the lateral seepage, Q_{gw} is the ground water recharge.

For snow-dominated basins, river flow is the combined effect of runoff from the land and snowmelt from snow and glaciers. Runoff and snowmelt can be simulated simultaneously in the SWAT model. SWAT2012 uses SCS-CN method to calculate the surface runoff (Q_{surf}, mm) [298] as follows.

$$Q_{surf} = (R_{day} - I_a)^2 / (R_{day} - I_a + S) \quad (7.2)$$

where R_{day} is the rainfall for the day (mm), I_a is the initial abstraction losses (mm), and S is the soil retention parameter (mm) that is a function of the CN value for the day.

However, the snow module of SWAT has components to compute snowpack, snowmelt and snow cover that mainly depends on the mean daily air temperature (T_B) and the mean precipitation (P_B) of a particular elevation band [88,215,238]. It has been described as elevation bands based Temperature Index Model (TMI). The equations are given as-

$$T_B = T + (Z_B - Z) * dT / dZ \tag{7.3}$$

$$P_B = P + (Z_B - Z) * dP / dZ \tag{7.4}$$

where T_B is the mean temperature for a particular elevation band (^{O}C), T is the measured temperature (^{O}C) at the weather station, Z_B the band's midpoint elevation (m), Z the elevation of weather station (m), P_B the band's mean precipitation (mm), P the precipitation measured at the weather station (mm).

7.2.3 Description of Optimization Algorithm SUFI-2

In SUFI-2 optimization algorithm, the deviation between observed and simulated variables are defined as the model uncertainty. It simultaneously works to analyze the uncertainties as well as calibration of the model to ensure appropriate model parameterization. SUFI-2 illustrates parametric uncertainty as a homogeneous distribution; however model output uncertainty is measured by the 95% prediction uncertainty (95PPU) plot. The p factor which represents the percentage of observed data enveloped by our modeling result, the 95PPU, shows the quantity of uncertainty being captured. While the r-factor indicates the thickness of 95PPU envelope plot. There is no fixed threshold for p-factor and r-factor, but p-factor should be close to 1(varies 0 to 1) and r-factor zero/ or as less possible (varies ∞ to 0) for better simulations.

7.2.4 Description of Rain Events

IMD has classified daily rain fall intensity into ten classes, ranging from no traces to extremely exceptionally heavy rainfall. In the present study, these ten rainfall intensity classes have been modified to four broad categories viz. light (<7.5mm/day), moderate (7.5 to 35.4mm/day), heavy (35.5 to 124.4mm/day) and extremely heavy (>124.4mm/day) by combining reliable classes. It is done because very low and extremely heavy rainfall events

are very rare and therefore, it will not provide the sufficient observations for statistical analysis.

7.2.5 Statistics Used for Variable Evaluation

To evaluate the performance of simulated results at the four stream gauge sites, a set of commonly used statistics viz. (1) Nash-Sutcliffe Efficiency (*NSE*), (2) Coefficient of determination (R^2) and (3) Percentage Bias (*PBIAS*) are used. Also, model's simulated variables can be better analyzed by computing p-factor and r-factor which is given by SUFI-2 in the summary_stat.txt.

During simulation with the SUFI-2, NSE has been set as objective function with value ≥0.5. The hydrograph of the simulated stream flow can be best reflected by the objective function (Sevat et al., 1991). The value of NSE varies from -∞ to 1, where NSE=1 means perfect match between observed and simulated values. Negative values suggest that the mean observed value is a superior predictor as compared to the simulated values. Basically, NSE is the degree of fit between observed and simulated values when we plot them into 1:1 scale. The equation for NSE is given below:

$$NSE = 1 - \frac{\sum_{i=1}^{n}(O-P)^2}{\sum_{i=1}^{n}(O-\overline{O})^2} \tag{7.5}$$

Coefficient determination (R^2) shows the proportion of collective variance between observed and simulated values. The R^2 value varies between 0 to 1 where, higher the value of shows lower error variance and vise-versa. Equation for R^2 is given is below:

$$R^2 = \left(\frac{\sum_{i=0}^{n}(O-\overline{O})(P-\overline{P})}{\left[\sum_{i=1}^{n}(O-\overline{O})^2 \sum_{i=0}^{n}(P-\overline{P})^2\right]^{0.5}} \right)^2 \tag{7.6}$$

Percent bias (PBIAS) is the measure of average tendency of the simulated data, that could smaller or larger than the counterpart observed data [299]. The perfect value for PBIAS is 0, however positive and negative values of PBIAS denote underestimation and overestimation bias respectively.

$$PBIAS = \frac{\sum_{i=1}^{n}|O-P|}{\sum_{i=1}^{n}(O)} * 100 \tag{7.7}$$

RMSE-observations standard deviation ratio (*RSR*) is the standardize representation of the Root Mean Square Error (RMSE). It is the ratio between RMSE and standard deviation of observed variables. Basically, it combines both an error index and the additional information recommended by Moradkhani et al. 2005 [300]. The RSR can be calculated as:

$$RSR = \frac{RMSE}{STDEV_{Obs}} = \frac{\left[\sqrt{\sum_{i=1}^{n}(O-P)^2}\right]}{\left[\sqrt{\sum_{i=1}^{n}(O-\overline{O})^2}\right]} \tag{7.8}$$

RSR combines the advantage of error index statistics as wel as a scaling/or normalization factor so that the subsequent statistic and stated values can relate to various constituents. It's value ranges from 0 to a large value. The RSR value of 0 indicates zero RMSE or residual variation and therefore perfect model simualtion. Lower the RSR value means lower is the RMSE/residual, and therefore better is the model simulation performance[301].

In the equations (7.5), (7.6), (7.7) and (7.8), *O* is the observed variables, *P* is the simualtes variables, $\overline{O}$ is the mean of observed variables, $\overline{P}$ is the mean of simulated varaibales and *i-n* is the length of observations.

7.3 Results and Discussion

7.3.1 Sensitivity and Model Performance

The sensitive parameters, as in the Chapter 6 (sensitivity analysis with gauge based precipitation product APHRODITE), were used in this study. These parameters are listed in the Table 7.2, which shows the overall hydrological properties of the basin in general. The sensitivity analysis found thirteen effective parameters from land phase in which four parameters are related to HRU (.hru file), five from ground water (.gw file), two from main channel (.rte file) and one each for soil (.sol file) and management practices (.mgt file). The rest of the sensitive parameters belong to snow and elevation band phase, found in basin (.bsn) and sub-basin (.sub) files.

Table 7.2: Sensitive parameters for the model and their rank

Land Phase Parameters	**Snow project**
1_CN2	2_SMFMN
3_HRU_SLP	11_TIMP
5_EPCO	12_SMTMP
6_GW_REVAP	13_SNOWCOVMX
7_SOL_ALB	16_SNOW50COV
9_SOL_AWC	18_SFTMP
10_ALPHA_BF	22_SMFMX
14_CANMX	**Elevation band project**
15_ESCO	4_TLAPS
17_REVAPMN	8_PLAPS
19_CH_K2	Here in X_paramters, X (1, 2, 3…) denotes the rank of the parameter in terms of the sensitivity.
20_SLSUBBSN	
21_CH_N2	

In this study, sensitive parameters (Table 7.2) have been tuned with the four elevations bands (2 to 4 elevation bands are found most suited for the area as outlined in the chapter 6) to simulate the stream flow at four gauging sites for a time span of ten years (2000-2010). The model was first initiated with two years of warmup period and then it iterated thrice for 1000 runs with the SUFI-2 optimization algorithm. The Nash- Sutcliffe Efficiency (NSE) have been used as the objective function (NSE≥0.5). The input details to simulate the SWAT model are given in Table 7.3.

Table 7.3: Input details for SWAT simulation

1.	Number of years for simulation	10
2.	Warmup period	2
3.	Number of Sub-basins in the project	41
4.	Number of HRUs in the project	420
5.	Number of Elevation bands	4
6.	Rainfall TRMM 3B42 V7 (gridded)	0.25^0
7.	Observed Streamflow data	Daily
8.	Land use Land cover	1 km
9.	Soil Type	10 km
10.	Digital Elevation Model (DEM)	90m
11.	Number of stream gauge stations	5

The model simulations are performed by modifying the twenty two parameters (Table 7.2) using SWAT-CUP. The streamflow have been simulated with these parameters to examine the streamflow during the extreme rain events (described in the section 7.2.4). The streamflow simulation has been done at various reach levels, moving from upstream gauge to downstream gauge. One thousand SWAT simulation has been performed with the

initial SWAT parameters range with objective function NSE≥0.5. Thereafter, the model have iterated the simulations twice by importing SWAT parameter's range each time from previous iteration. The SWAT parameters judged influential during sensitivity analysis are comparable with the studies conducted by Pradhanang et al. 2011 [250] and Meng et al. 2015 [276] for snow dominated basins. The fitted parameter's range and method adopted to change that parameter during simulation are given the Table 7.4.

The statistical results presented in Table 7.5 shows very good agreement between simulation streamflow and stream gauge data at each stations. The NSE value is greater than 0.65 for all station which shows that SWAT-CUP has optimized well to set objective function. Among all sub-basins Betravati-23 shows better simulation with the given parameters in terms of NSE (0.79), however downstream stream gauge station Triveni-39 shows better PBAIS (2.9%) than others. Similarly, Betravati-23 shows better R^2 than others. The p-factor (0.95) is better for Arughat-13 but r-factor (1.28) is largest among all, which is should be close to zero. Similarly r-factor is smallest (0.8) for Betravati-23, p-factor (0.66) is not good to make it best. Overall, statistics are getting improved on moving from upstream to downstream gauge stations.

The daily average (2000-2010) TRMM simulated vs. observed stream gauge hydrograph for each stream gauge stations have been presented in the Figure 7.2. From the hydrograph, Arughat-13 stream gauge station show little bit of underestimation throughout except few aspersions during hot summer-monsoon. However simulated hydrograph fallows the pattern of observed hydrograph decently at this gauge site. For the Betravati-23 site, the hydrograph patterns are similar to Arughat-13, but both the hydrographs are more close and smooth to each other which is quite irregular for Arughat-13. During monsoon (High rain events), TRMM simulated streamflow are significantly underestimating for Kumargaon-25, however both hydrograph matches well during non-monsoon season. Similarly, Narayanighat-36 and Triveni-39 also, reflect peaks for stream gauge hydrograph which are not matching with the TRMM simulated hydrograph. Therefore, it can be interpreted that TRMM simulated hydrograph are not able to depict extreme rain event's streamflow, but performs quite decent for moderate and high rain events.

Table 7.4: The calibrated parameters, range (Min, Max) and their fitted values. The V, A, R represents the replace, additive and relative methods to change the parameters value during simulations [275]

Parameter	Description	Default	Fitted value	Min	Max
Hydrological Parameters					
R_HRU_SLP.hru	Average slope steepness	HRU	0.088	-0.04	0.2
R_SLSUBBSN.hru	Average slope length	HRU	-0.172	-0.2	-0.05
V_ESCO.hru	Soil evaporation compensation factor	HRU	0.877	0.85	0.95
V_CANMX.hru	Maximum canopy storage	HRU	16.557	5	20
R_CN2.mgt	SCS curve number	HRU	-0.0849	-0.18	0
A_ALPHA_BF.gw	Base flow alpha factor (Days)	0.048	0.273	0.02	0.4
A_GW_DELAY.gw	Groundwater delay	31	32.62	5	45
A_GWQMN.gw	Threshold in the shallow aquifer for return flow to occur	1000	-704.56	-1000	-350
V_CH_N2.rte	Manning's "n" value for the main channel	0.014	0.323	0.2	0.35
V_CH_K2.rte	Hydraulic conductivity in main channel	0	543.772	315	550
A_GW_REVAP.gw	Groundwater "revap" coefficient	0.02	0.151	0.12	0.18
A_REVAPMN.gw	Threshold water depth (mm) in the shallow aquifer to occur 'revap'	750	149.46	-370	390
R_SOL_AWC.sol	Water holding capacity of soil layers	Soil layer	0.0117	0	0.2
Snow Parameters					
V_SFTMP.bsn	Snowfall temperature (°C)	1	-2.194	-6	-2
V_SMTMP.bsn	Snowmelt base temperature (°C)	0.5	4.8435	3	6
V_SMFMX.bsn	Maximum melt rate for snow during year	4.5	5.849	4	6
V_SMFMN.bsn	Minimum melt rate for snow during year	4.5	3.061	2	4
V_TIMP.bsn	Snowpack temperature lag factor	1	0.203	0	0.3
V_SNOCOVMX.bsn	Snow water equivalent (mm) during the 50% snow cover	1	66.075	60	90
V_SNO50COV.bsn	Snow water equivalent (mm) during100% snow cover	0.5	0.203	0	0.35
Elevation band Parameters					
SNOEB.sub	Initial water content in the elevation bands	100m Constant for snow dominated sub-basins			
R_TLAPS.sub	Precipitation lapse rate °C/km	-6	-0.528	-1.2	0.38
R_PLAPS.sub	Temperature lapse rate mm/km	200	0.46	-0.2	1.35

Table 7.5: Streamflow simulation statistics for different stream gauge sites of Gandak River basin

Station	Model simulation Statistics				
	p-factor	r-factor	R^2	NSE	PBIAS
Arughat_13	0.95	1.28	0.75	0.71	9.7
Betravati_23	0.66	0.8	0.82	0.79	11.8
Kumalgaon_25	0.92	1.04	0.71	0.68	15.8
Narayanighat_36	0.83	1.07	0.67	0.65	12.2
Triveni_39	0.86	1.21	0.68	0.67	2.9

7.3.2 Evaluation of TRMM Simulated vs. Observed Streamflow for Various Rain Events

The Hydrograph (Figure 7.2) is only depicting pattern with respect to the rain events but it does not reveal the characteristics/or response of TRMM simulated streamflow to different class of rain fall intensities. For this, PBIAS and RSR statistics between TRMM simulated and observed streamflow have been evaluated for various rain fall intensity classes (described in the section 7.2.4).

The BIAS statistics is able to indicate about the nature as well as magnitude of error, however RSR gives information on the error index in terms of accumulated residual error. A simple linear trend line for PBIAS and RSR by plotting increasing rainfall intensities in the x-axis and magnitude to statistics (BIAS and RSR) in y-axis have also been drawn (Figure 7.3), that shows the overall character of particular statistical parameters with respect to rain fall intensity classes.

From Figure 7.3, it can be seen that light rain events shows very high and positive PBIAS for all sites except at Kumalgaon-25 where it is considerably low. High and positive BIAS for low rain events shows that TRMM simulated streamflow are underestimated. In case of high rain events Arughat-13 and Betravati-23 shows large negative PBIAS which means, for extreme rain events TRMM simulated stream flow is overestimating for these sub-basins. At the Narayanighat-36 and Triveni-39 sites, PBIAS is ±10% for rain events >7.5 mm/day, which shows a consistent TRMM based stream flow simulations at these sites. All stream gauge sites show a decreasing trend line for PBIAS. Conversely, Kumalgaon-25 shows a gradual positive increase in the PBIAS with respect to increase in the rain fall intensities.

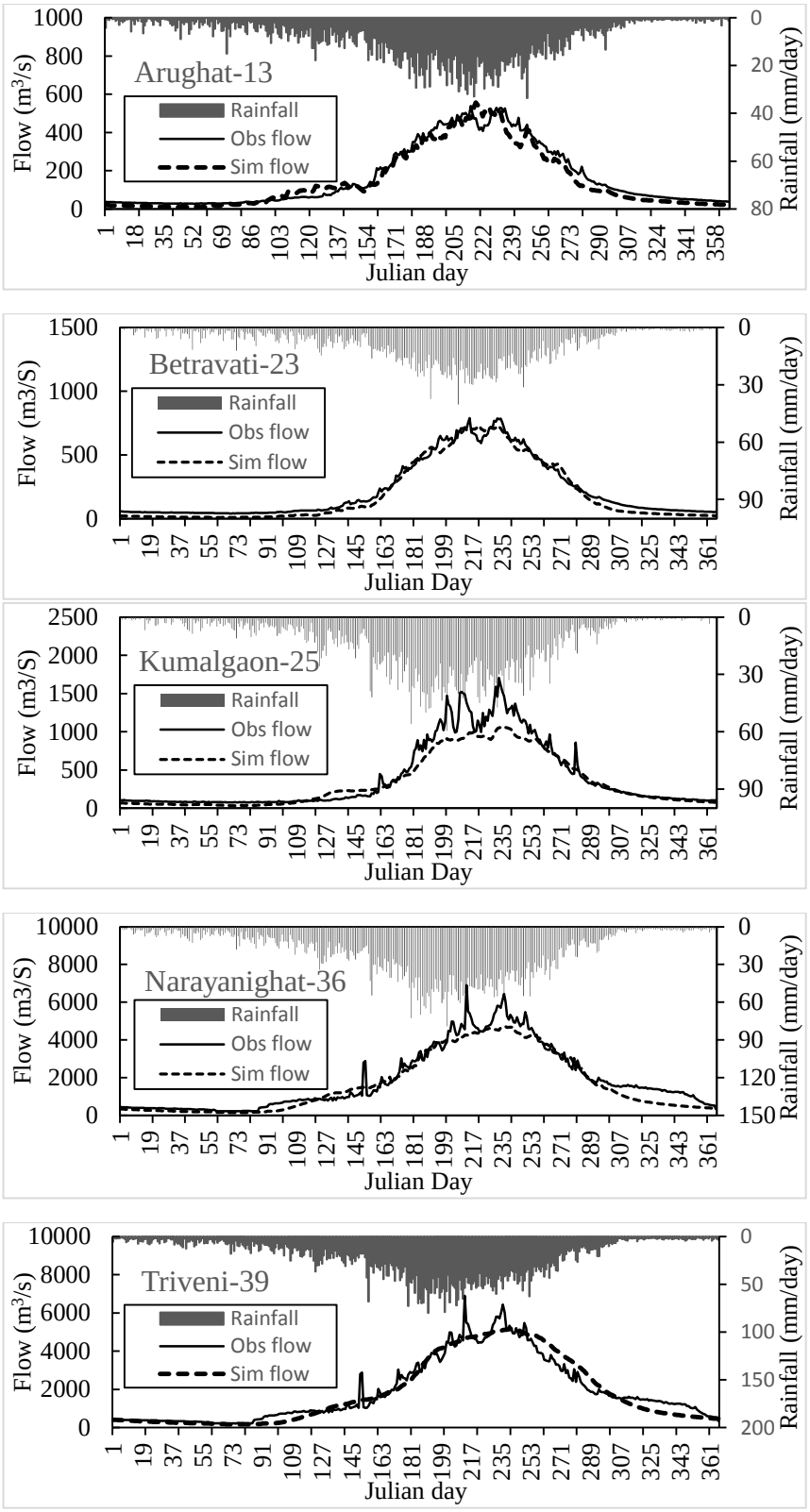

Figure 7.2: Daily average (2000-2010) TRMM simulated streamflow vs. Observed streamflow (in primary axis), and daily average rainfall (in secondary axis)

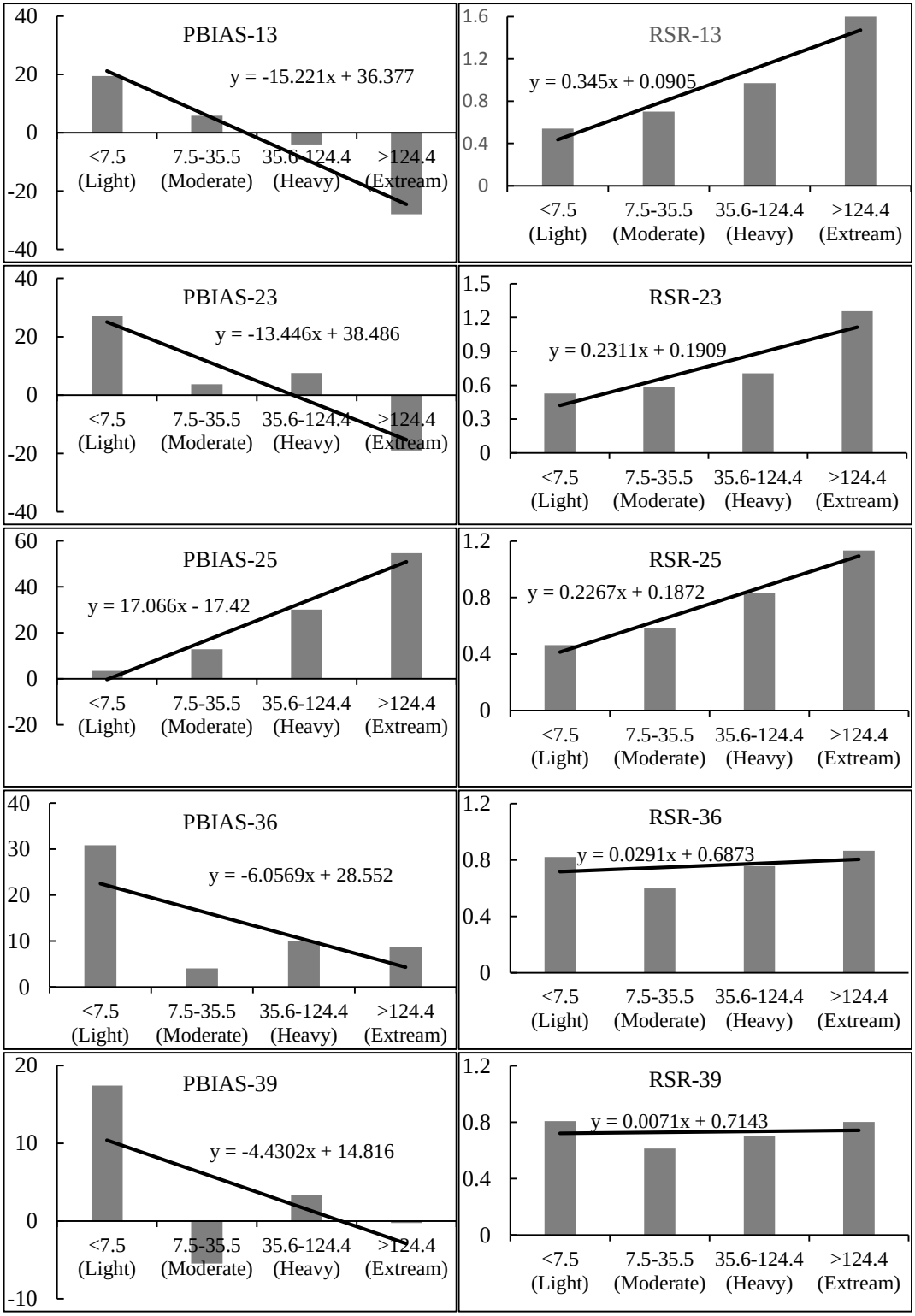

Figure 7.3: The statistical results for TRMM simulated streamflow vs. observed streamflow at various Rain events

This change in the nature of PBIAS trend for this site may be due to human induced innervation [302], which may be affecting natural flow regime. The RSR statistics shows a gradual increase for Arughat-13, Betravati-23 and Kumalgaon-25, which reveals a consistent increase in the residual error by moving from light to extreme rain events. However, the trend line for the RSR at the downstream sites have almost zero tangent, showing no change in the character of residual error for various rain events. Considering both the statistics at all sites, in general TRMM simulated stream flow is worse for extreme events and low events, however it does well for moderate and heavy rain events.

7.4 Summary

The present research work comprises of the application of SWAT model to simulate the stream flow based on TRMM 3B42 precipitation data product and assessing their applicability for various rainfall intensity classes. The work has been carried out at a Himalayan "Gandak River Basin. The five stream gauge sites from upstream to downstream have been used to get better fit between TRMM simulated and observed stream flow. The summary point are as follows-

- The whole basin has been divided into 41 sub-basins to use their own channel characteristics and climatic data. Sub-basins are further divided into 420 HRUs using similar threshold for soil, land use and slope characteristics. The model performance is rated to be reasonably good in terms of NSE>0.65, R^2>0.67 and PBIAS≤ 15 percent. The SWAT model is simulated for three iterations with NSE≥0.5 as objective functions to achieve the said stream flow simulation results.
- After the TRMM based stream flow simulations, the suitability for four broad category of rainfall intensities have been evaluated by using two frequently used statistics PBIAS and RSR. Both the statistics reveal that TRMM 3B42 V7 based stream flow simulation is performing well for moderate to high rainfall intensities, however it is not found reasonable better for low and extreme rainfall intensities. The analysis reveals critical information about the watershed response to TRMM 3B42 V7 based stream flow simulation for various rainfall intensities. Therefore, the results based on this analysis will assist in the methodical water resources allocation, planning and management by using TRMM 3B42 V7 precipitation product over the Himalayan River Basins.

Chapter 8

Conclusions

8.1 Conclusions

In this study various uncertainties due to input, model structure/setup and parameters have been evaluated for a Himalayan River Basin Gandak. The conclusions drawn based on objective themes are segmented below-

In the first segment (Chapter 4), error in the inputs especially physical as well as topographical model inputs derived from DEMs and error in satellite precipitation products have been analyzed. The conclusions based on the study are follows-

- In the first part of this work, error in the basin morphology for three DEMs namely SRTM 30m, ASTER 30m and SRTM 90m have been evaluated. The error in the basin area shows that SRTM 90m delineates close to the GFCC (reference) map. Relative difference (RD) statistics shows a close agreement between digital stream networks and reference stream networks for ASTER 30m at upper mountainous part of the basin, however SRTM 90m proved better at over all basin scale. In general, SRTM 90m DEM performs well in all respects, whereas SRTM30m and ASTER30m DEMs can be used with due care over flat terrains.
- In the second part of this work, two satellite precipitation products: gauge adjusted TRMM 3B42 V7 and exclusively satellite derived CMORPH have been evaluated for their qualitative and quantitative feasibility. The results of the study show that the quality of satellite precipitation product varies with the elevation of the area. The gauge adjusted TRMM 3B42 V7 precipitation product is found more accurate than exclusively satellite-based precipitation product CMORPH. Therefore, TRMM 3B42V7 product can be used for water balance modeling and extreme event analysis in mountainous Himalayan basin with caution.

In second segment (Chapter 5) different DEM grid size and resampling techniques have been evaluated for model output uncertainties. For this, SRTM DEM 90m is resampled for sixteen grid size from 40-1000m with three methods namely nearest neighborhood,

bilinear and cubic convolution. Thereafter, all scenarios were used to setup SWAT model. The uncertainty in the modeling outputs for these scenarios have been evaluated with the relative difference (RD) statistics. In general, DEM grid sizes ≤150m resampled with bilinear method performs well for flow, sediment, TN and TP. Also, the *t-test* statistics show no significant change in the SWAT outputs for DEM grid size ≤ 500m at monthly and yearly scale.

The third segment (chapter 6) highlight the effect of different model setups to simulate snow dynamics and streamflow over the alpine Himalayan region. The study concludes that the use of elevation band approach has very meaningful enhancement in the results of streamflow as well as other hydrological components. Therefore, it is recommended to implement SWAT model with snow model setup along with appropriate number of elevation bands in this region.

Fourth and final segment (Chapter 7) is on the streamflow simulation by using TRMM 3B42 V7 gauge adjusted precipitation data for Gandak River Basin. The simulations were constraints with the minimum attainable NSE≥0.5. The statistical results based on NSE, R^2 and PBIAS shows a good simulation of streamflow based on the calibrated parameters. Also the statistics PBIAS and RSR between observed and simulated streamflow for various rainfall intensity classes show that simulated streamflow performs well for moderate to high rainfall intensity classes.

8.2 Scope of the Future Work

The following are some suggestions for future work based on the findings, conclusions and problems identified on the course of the present work.

i) The first objective only illustrates the error in the topography and basin area by using three widely available DEMs SRTM 30m, SRTM 90m and ASTER 30m, it would be interesting to see the feasibility of other available DEM like Carto-Sat.
ii) The second objective analyses the error in the TRMM 3B42 V7 and CMROPH at daily time steps, so other satellite products like PERSIANN and CPC REF 2.0 can also be accessed for their accuracy at daily and sub-daily time steps.
iii) Our study have not checked the accuracy of simulated sediment, TN and TP, it would be great to simulate these with their observed values.
iv) It would be interesting to simulate the hydrological component, streamflow, evapotranspiration and infiltration simultaneously with their observed data.
v) Evapotranspiration can also be modelled using MODIS evapotranspiration data as an input in the SWAT model for the study area.
vi) Uncertainty in the SWAT model outputs can be accessed for various land use grid size and number of rain gauge points for the basin.

References

[1] A.F. Lutz, W.W. Immerzeel, A.B. Shrestha, M.F.P. Bierkens, Consistent increase in High Asia's runoff due to increasing glacier melt and precipitation, Nat. Clim. Chang. 4 (2014) 587–592.

[2] D. Alford, R. Armstrong, The role of glaciers in stream flow from the Nepal Himalaya, Cryosph. Discuss. 4 (2010) 469–494.

[3] J. Yang, P. Gong, R. Fu, M. Zhang, J. Chen, S. Liang, B. Xu, J. Shi, R. Dickinson, The role of satellite remote sensing in climate change studies, Nat. Clim. Chang. 3 (2013) 875–883.

[4] K.K. Benke, K.E. Lowell, A.J. Hamilton, Parameter uncertainty, sensitivity analysis and prediction error in a water-balance hydrological model, Math. Comput. Model. 47 (2008) 1134–1149.

[5] S.P. Wechsler, Uncertainties associated with digital elevation models for hydrologic applications: a review, Hydrol. Earth Syst. Sci. 11 (2007) 1481–1500.

[6] A. Montanari, What do we mean by " uncertainty "? The need for a consistent wording about uncertainty assessment in hydrology, Hydrol. Process. 21 (2007) 841–845.

[7] L.A. Zadeh, Toward a generalized theory of uncertainty (GTU)—an outline, Inf. Sci. (Ny). 172 (2005) 1–40.

[8] B. Renard, D. Kavetski, G. Kuczera, M. Thyer, S.W. Franks, Understanding predictive uncertainty in hydrologic modeling: The challenge of identifying input and structural errors, Water Resour. Res. 46 (2010) 1–22.

[9] K.C. Abbaspour, C. a. Johnson, M.T. van Genuchten, Estimating uncertain flow and transport parameters using a sequential uncertainty fitting procedure, Vadose Zo. J. 3 (2004) 1340–1352.

[10] K.C. Abbaspour, M. Vejdani, S. Haghighat, J. Yang, SWAT-CUP Calibration and Uncertainty Programs for SWAT, Fourth Int. SWAT Conf. (2007) 1596–1602.

[11] M.M. Rahman, D.S. Arya, N.K. Goel, Limitation of 90 m SRTM DEM in drainage network delineation using D8 method—a case study in flat terrain of Bangladesh, Appl. Geomatics. 2 (2010) 49–58.

[12] R. Sørensen, J. Seibert, Effects of DEM resolution on the calculation of topographical indices: TWI and its components, J. Hydrol. 347 (2007) 79–89.

[13] A.R. Da Paz, W. Collischonn, A. Risso, C.A.B. Mendes, Errors in river lengths derived from raster digital elevation models, Comput. Geosci. 34 (2008) 1584–1596.

[14] H. McMillan, B. Jackson, M. Clark, D. Kavetski, R. Woods, Rainfall uncertainty in hydrological modelling: An evaluation of multiplicative error models, J. Hydrol. 400 (2011) 83–94.

[15] L. Moulin, E. Gaume, C. Obled, Uncertainties on mean areal precipitation: assessment and impact on streamflow simulations, Hydrol. Earth Syst. Sci. 13 (2009)

99–114.

[16] S.N. Miller, D. Phillip Guertin, D.C. Goodrich, Hydrologic modeling uncertainty resulting from land cover misclassification, J. Am. Water Resour. Assoc. 43 (2007) 1065–1075.

[17] X.C. Ye, N.R. Viney, Q. Zhang, Effects of spatial resolution of soil data on hydrological processes modelling: A case study using the SWAT model, in: 18th World Imacs Congr. Modsim09 Int. Congr. Model. Simul. Interfacing Model. Simul. with Math. Comput. Sci., 2009: pp. 3216–3222.

[18] R.J. Pike, Geomorphometry -diversity in quantitative surface analysis, Prog. Phys. Geogr. 24 (2000) 1–20.

[19] P.F. Fisher, N.J. Tate, Causes and consequences of error in digital elevation models, Prog. Phys. Geogr. 30 (2006) 467–489.

[20] S. Wise, Assessing the quality for hydrological applications of digital elevation models derived from contours, Hydrol. Process. 14 (2000) 1909–1929.

[21] G.B.M. Heuvelink, Error propagation in environmental modelling with GIS, Taylor & Francis, 1998.

[22] G. Petersen, I. Lebed, N. Fohrer, SRTM DEM levels over papyrus swamp vegetation – a correction approach, Adv. Geosci. 21 (2009) 81–84.

[23] S. Mukherjee, P.K. Joshi, S. Mukherjee, A. Ghosh, R.D. Garg, A. Mukhopadhyay, Evaluation of vertical accuracy of open source Digital Elevation Model (DEM), Int. J. Appl. Earth Obs. Geoinf. 21 (2013) 205–217.

[24] S. Muralikrishnan, A. Pillai, B. Narender, S. Reddy, V.R. Venkataraman, V.K. Dadhwal, Validation of indian national dem from Cartosat-1 data, J. Indian Soc. Remote Sens. 41 (2013) 1–13.

[25] D. Athmania, H. Achour, External validation of the ASTER GDEM2, GMTED2010 and CGIAR-CSI- SRTM v4.1 free access Digital Elevation Models (DEMs) in Tunisia and Algeria, Remote Sens. 6 (2014) 4600–4620.

[26] A. Patel, S.K. Katiyar, V. Prasad, Performances evaluation of different open source DEM using Differential Global Positioning System (DGPS), Egypt. J. Remote Sens. Sp. Sci. 19 (2016) 7–16..

[27] J.P. Wilson, J.C. Gallant, Terrain analysis : principles and applications, Wiley, 2000.

[28] L.W. Martz, J. Garbrecht, Numerical definition of drainage network and subcatchment areas from Digital Elevation Models, Comput. Geosci. 18 (1992) 747–761.

[29] J.F. O'Callaghan, D.M. Mark, The extraction of drainage networks from digital elevation data, Comput. Vision, Graph. Image Process. 28 (1984) 323–344.

[30] J. Seibert, B.L. McGlynn, A new triangular multiple flow direction algorithm for computing upslope areas from gridded digital elevation models, Water Resour. Res. 43 (2007) WR005128.

[31] D.G. Tarboton, A new method for the determination of flow directions and upslope areas in grid digital elevation models, Water Resour. Res. 33 (1997) 309–319.

[32] P. Quinn, K. Beven, P. Chevallier, O. Planchon, The prediction of hillslope flow paths for distributed hydrological modelling using digital terrain models, Hydrol. Process. 5 (1991) 59–79.

[33] A.R. Paz, W. Collischonn, A.L. Lopes Da Silveira, Improvements in large-scale drainage networks derived from digital elevation models, Water Resour. Res. 42 (2006) 1–7.

[34] S.M. Reed, Deriving flow directions for coarse-resolution (1-4 km) gridded hydrologic modeling, Water Resour. Res. 39 (2003) WR001989.

[35] L.P. Rampi, J.F. Knight, C.F. Lenhart, Comparison of flow direction algorithms in the application of the cti for mapping wetlands in minnesota, Wetlands. 34 (2014) 513–525.

[36] Z. Li, Variation of the accuracy of digital terrain models with sampling interval, Photogramm. Rec. 14 (2006) 113–128.

[37] D.M. Wolock, G.J. McCabe, Differences in topographic characteristics computed from 100- and 1000-m resolution digital elevation model data, Hydrol. Process. 14 (2000) 987–1002.

[38] D. Yang, S. Herath, K. Musiake, Spatial resolution sensitivity of catchment geomorphologic properties and the effect on hydrological simulation, Hydrol. Process. 15 (2001) 2085–2099.

[39] V. Chaplot, Impact of DEM mesh size and soil map scale on SWAT runoff, sediment, and NO3-N loads predictions, J. Hydrol. 312 (2005) 207–222.

[40] I. Chaubey, A.S. Cotter, T.A. Costello, T.S. Soerens, Effect of DEM data resolution on SWAT output uncertainty, Hydrol. Process. 19 (2005) 621–628.

[41] B. Dixon, J. Earls, Resample or not?! Effects of resolution of DEMs in watershed modeling, Hydrol. Process. 23 (2009) 1714–1724.

[42] G.J. Zhao, G. Hörmann, N. Fohrer, J.F. Gao, Impacts of spatial data resolution on simulated discharge, a case study of Xitiaoxi catchment in South China, Adv. Geosci. 21 (2009) 131–137.

[43] S. Lin, C. Jing, V. Chaplot, X. Yu, Z. Zhang, N. Moore, J. Wu, Effect of DEM resolution on SWAT outputs of runoff, sediment and nutrients, Hydrol. Earth Syst. Sci. Discuss. 7 (2010) 4411–4435.

[44] S. Lin, C. Jing, N.A. Coles, V. Chaplot, N.J. Moore, J. Wu, Evaluating DEM source and resolution uncertainties in the Soil and Water Assessment Tool, Stoch. Environ. Res. Risk Assess. 27 (2013) 209–221.

[45] V. Chaplot, Impact of spatial input data resolution on hydrological and erosion modeling: Recommendations from a global assessment, Phys. Chem. Earth, Parts A/B/C. 67 (2014) 23–35.

[46] P. Zhang, R. Liu, Y. Bao, J. Wang, W. Yu, Z. Shen, Uncertainty of SWAT model at different DEM resolutions in a large mountainous watershed, Water Res. 53 (2014) 132–144.

[47] L. Chen, Y. Gong, Z. Shen, A comprehensive evaluation of input data-induced

uncertainty in nonpoint source pollution modeling, HESSD Earth Syst. Sci. Discuss. 12 (2015) 11421–11447.

[48] H. Wang, Z. Wu, C. Hu, A Comprehensive Study of the Effect of Input Data on Hydrology and non-point Source Pollution Modeling, Water Resour. Manag. 29 (2015) 1505–1521.

[49] M.L. Tan, D.L. Ficklin, B. Dixon, A.L. Ibrahim, Z. Yusop, V. Chaplot, Impacts of DEM resolution, source, and resampling technique on SWAT-simulated streamflow, Appl. Geogr. 63 (2015) 357–368.

[50] P.A. Burrough, R. McDonnell, C.D. Lloyd, Principles of geographical information systems, Oxford Uni. Press 1988.

[51] W. Rieger, A phenomenon-based approach to upslope contributing area and depressions in DEMs, Hydrol. Process. 12 (1998) 857–872.

[52] G. Zhao, J. Gao, P. Tian, K. Tian, Comparison of two different methods for determining flow direction in catchment hydrological modeling, Water Sci. Eng. 2 (2009) 1–15.

[53] K.J. Beven, Rainfall-runoff modelling : the primer, Wiley, 2012.

[54] G. Kuczera, D. Kavetski, S. Franks, M. Thyer, Towards a Bayesian total error analysis of conceptual rainfall-runoff models: Characterising model error using storm-dependent parameters, J. Hydrol. 331 (2006) 161–177.

[55] G. Villarini, P. V. Mandapaka, W.F. Krajewski, R.J. Moore, Rainfall and sampling uncertainties: A rain gauge perspective, J. Geophys. Res. 113 (2008) D11102.

[56] J.C. Refsgaard, J.P. van der Sluijs, J. Brown, P. van der Keur, A framework for dealing with uncertainty due to model structure error, Adv. Water Resour. 29 (2006) 1586–1597.

[57] A. Molini, L.G. Lanza, P. La Barbera, The impact of tipping-bucket raingauge measurement errors on design rainfall for urban-scale applications, Hydrol. Process. 19 (2005) 1073–1088.

[58] B.P. La, L.G. Lanza, L. Stagi, Tipping bucket mechanical errors and their influence on rainfall statistics and extremes., Water Sci. Technol. 45 (2002) 1–10.

[59] V.S. Shedekar, K.W. King, L.C. Brown, N.R. Fausey, M. Heckel, R. Daren Harmel, Measurement errors in tipping bucket rain gauges under different rainfall intensities and their implication to hydrological models, in: ASABE Annu. Iternational Meet., Reno, Nevada, June 21 – June 24, 2009.

[60] W.F. Krajewski, J.A. Smith, Radar hydrology: rainfall estimation, Adv. Water Resour. 25 (2002) 1387–1394.

[61] B. Chapon, G. Delrieu, M. Gosset, B. Boudevillain, Variability of rain drop size distribution and its effect on the Z–R relationship: A case study for intense Mediterranean rainfall, Atmos. Res. 87 (2008) 52–65.

[62] P. Reichert, J. Mieleitner, Analyzing input and structural uncertainty of nonlinear dynamic models with stochastic, time-dependent parameters, Water Resour. Res. 45 (2009) W10402.

[63] V. Maggioni, H.J. Vergara, E.N. Anagnostou, J.J. Gourley, Y. Hong, D. Stampoulis, V. Maggioni, H.J. Vergara, E.N. Anagnostou, J.J. Gourley, Y. Hong, D. Stampoulis, Investigating the applicability of error correction ensembles of satellite rainfall products in river flow simulations, J. Hydrometeorol. 14 (2013) 1194–1211.

[64] W. Yu, E. Nakakita, S. Kim, K. Yamaguchi, W. Yu, E. Nakakita, S. Kim, K. Yamaguchi, Impact assessment of uncertainty propagation of ensemble NWP rainfall to flood forecasting with catchment scale, Adv. Meteorol. 2016 (2016) 1–17.

[65] S. Ud Din, a. Al-Dousari, a. Ramdan, a. Al Ghadban, Site-specific precipitation estimate from TRMM data using bilinear weighted interpolation technique: An example from Kuwait, J. Arid Environ. 72 (2008) 1320–1328.

[66] E.E. Ebert, Fuzzy verification of high-resolution gridded forecasts : a review and proposed framework, 64 (2008) 51–64.

[67] Z. Yu, H. Yu, P. Chen, C. Qian, C. Yue, Verification of tropical cyclone-related satellite precipitation estimates in mainland China, J. Appl. Meteorol. Climatol. 48 (2009) 2227–2241.

[68] S. Nair, G. Srinivasan, R. Nemani, Evaluation of multi-satellite TRMM derived rainfall estimates over a western state of India, J. Meteorol. Soc. Japan. 87 (2009) 927–939.

[69] S.H. Rahman, D. Sengupta, M. Ravichandran, Variability of Indian summer monsoon rainfall in daily data from gauge and satellite, J. Geophys. Res. 114 (2009) D17113.

[70] a. K. Mitra, a. K. Bohra, M.N. Rajeevan, T.N. Krishnamurti, Daily Indian precipitation analysis formed from a merge of rain-gauge data with the TRMM TMPA satellite-derived rainfall estimates, J. Meteorol. Soc. Japan. 87A (2009) 265–279.

[71] T. Condom, P. Rau, J.C. Espinoza, Correction of TRMM 3B43 monthly precipitation data over the mountainous areas of Peru during the period 1998-2007, Hydrol. Process. 25 (2011) 1924–1933.

[72] A. Harris, S. Rahman, F. Hossain, L. Yarborough, A.C. Bagtzoglou, G. Easson, Satellite-based flood modeling using TRMM-based rainfall products, Sensor. 7 (2007) 3416–3427.

[73] B. Collischonn, W. Collischonn, C.E.M. Tucci, Daily hydrological modeling in the Amazon basin using TRMM rainfall estimates, J. Hydrol. 360 (2008) 207–216.

[74] B. Yong, L.L. Ren, Y. Hong, J.H. Wang, J.J. Gourley, S.H. Jiang, X. Chen, W. Wang, Hydrologic evaluation of Multisatellite Precipitation Analysis standard precipitation products in basins beyond its inclined latitude band: A case study in Laohahe basin, China, Water Resour. Res. 46 (2010) 1–20.

[75] C.B. Moffitt, F. Hossain, R.F. Adler, K.K. Yilmaz, H.F. Pierce, Validation of a TRMM-based global Flood Detection System in Bangladesh, Int. J. Appl. Earth Obs. Geoinf. 13 (2011) 165–177.

[76] P. Mantovan, E. Todini, Hydrological forecasting uncertainty assessment: Incoherence of the GLUE methodology, J. Hydrol. 330 (2006) 368–381.

[77] K. Beven, P. Smith, J. Freer, Comment on “Hydrological forecasting uncertainty assessment: Incoherence of the GLUE methodology” by Pietro Mantovan and Ezio Todini, J. Hydrol. 338 (2007) 315–318.

[78] K.J. Beven, P.J. Smith, J.E. Freer, So just why would a modeller choose to be incoherent?, J. Hydrol. 354 (2008) 15–32.

[79] J.A. Vrugt, C.J.F. ter Braak, H. V. Gupta, B.A. Robinson, Equifinality of formal (DREAM) and informal (GLUE) Bayesian approaches in hydrologic modeling?, Stoch. Environ. Res. Risk Assess. 23 (2009) 1011–1026.

[80] K. Beven, P.J. Smith, A. Wood, On the colour and spin of epistemic error (and what we might do about it), Hydrol. Earth Syst. Sci. 15 (2011) 3123–3133.

[81] D. Kavetski, G. Kuczera, S.W. Franks, Bayesian analysis of input uncertainty in hydrological modeling: 1. Theory, Water Resour. Res. 42 (2006) W03407.

[82] D. Huard, A. Mailhot, Calibration of hydrological model GR2M using Bayesian uncertainty analysis, Water Resour. Res. 44 (2008) W02424.

[83] H. Moradkhani, S. Sorooshian, H. V. Gupta, P.R. Houser, Dual state–parameter estimation of hydrological models using ensemble Kalman filter, Adv. Water Resour. 28 (2005) 135–147.

[84] P. Young, Data-based mechanistic modelling of environmental, ecological, economic and engineering systems, Environ. Model. Softw. 13 (1998) 105–122.

[85] N. Bulygina, H. Gupta, Estimating the uncertain mathematical structure of a water balance model via Bayesian data assimilation, Water Resour. Res. 45 (2009) W00B13

[86] K. Beven, A. Binley, The future of distributed models: Model calibration and uncertainty prediction, Hydrol. Process. 6 (1992) 279–298.

[87] A.P. Jacquin, A.Y. Shamseldin, Development of a possibilistic method for the evaluation of predictive uncertainty in rainfall-runoff modeling, Water Resour. Res. 43 (2007) W04425.

[88] J.G. Arnold, J.R. Kiniry, R. Srinivasan, J.R. Williams, E.B. Haney, S.L. Neitsch, Soil & Water Assessment Tool: Input/output documentation. version 2012, Texas Water Resour. Institute, TR-439. (2013) 650.

[89] K.L. White, I. Chaubey, Sensitivity analysis, calibration, and validations for a multisite and multivariable SWAT model, J. Am. Water Resour. Assoc. 41 (2005) 1077–1089.

[90] Ö. Güngör, S. Göncü, Application of the soil and water assessment tool model on the Lower Porsuk Stream Watershed, Hydrol. Process. 27 (2013) 453–466.

[91] V. Singh, A.K. Bera, J.R. Sharma, Hydrological stream flow modeling on Tungabhadra catchment : Parameterization and uncertainty analysis using SWAT CUP Hydrological stream flow modelling on Tungabhadra catchment : parameterization and uncertainty analysis using SWAT CUP, Curr. Sci. 104 (2013) 1187–1199.

[92] Y. Grusson, X. Sun, S. Gascoin, S. Sauvage, S. Raghavan, F. Anctil, J.-M. Sáchez-

Pérez, Assessing the capability of the SWAT model to simulate snow, snow melt and streamflow dynamics over an alpine watershed, J. Hydrol. 531 (2015) 574–588.

[93] J. Doherty, J.M. Johnston, Methodologies for calibration and predictive analysis of a watershed model, J. Am. Water Resour. Assoc. 39 (2003) 251–265.

[94] K. Beven, J. Freer, Equifinality, data assimilation, and uncertainty estimation in mechanistic modelling of complex environmental systems using the GLUE methodology, J. Hydrol. 249 (2001) 11–29.

[95] J. Benaman, C.A. Shoemaker, Methodology for analyzing ranges of uncertain model parameters and their impact on total maximum daily load process, J. Environ. Eng. 130 (2004) 648–656.

[96] Z.Y. Shen, L. Chen, T. Chen, Analysis of parameter uncertainty in hydrological and sediment modeling using GLUE method: a case study of SWAT model applied to Three Gorges Reservoir Region, China, Hydrol. Earth Syst. Sci. 16 (2012) 121–132.

[97] Y.K. Tung, B.C. Yen, Hydrosystems engineering uncertainty analysis, McGraw-Hill, 2005.

[98] Y. Gong, Z. Shen, Q. Hong, R. Liu, Q. Liao, Parameter uncertainty analysis in watershed total phosphorus modeling using the GLUE methodology, Agric. Ecosyst. Environ. 142 (2011) 246–255.

[99] N. Nandakumar, R.G. Mein, Uncertainty in rainfall—runoff model simulations and the implications for predicting the hydrologic effects of land-use change, J. Hydrol. 192 (1997) 211–232.

[100] K.J. Raat, J.A. Vrugt, W. Bouten, A. Tietema, Towards reduced uncertainty in catchment nitrogen modelling: quantifying the effect of field observation uncertainty on model calibration, Hydrol. Earth Syst. Sci. 8 (2004) 751–763.

[101] V.P. Singh, Computer models of watershed hydrology, Water Resources Publications, 1995.

[102] J. Jorgeson, P. Julien, Peak flow forecasting with radar precipitation and the distributed model CASC2D, Water Int. 30 (2005) 40–49.

[103] Cochrane T. A.; Flanagan D. C., Effect of DEM resolution in the runoff and soil loss predictions of the WEPP watershed model, Trans. ASAE 2005. 48 (2005) 109–120.

[104] I. Zacharias, E. Dimitriou, T. Koussouris, Integrated water management scenarios for wetland protection: Application in Trichonis Lake, Environ. Model. Softw. 20 (2005) 177–185.

[105] H. Xu, R.G. Taylor, Y. Xu, Quantifying uncertainty in the impacts of climate change on river discharge in sub-catchments of the Yangtze and Yellow River Basins, China, Hydrol. Earth Syst. Sci. 15 (2011) 333–344.

[106] Z. Shen, Q. Hong, H. Yu, J. Niu, Parameter uncertainty analysis of non-point source pollution from different land use types, Sci. Total Environ. 408 (2010) 1971–1978.

[107] D.G. Kingston, R.G. Taylor, Sources of uncertainty in climate change impacts on river discharge and groundwater in a headwater catchment of the Upper Nile Basin, Uganda, Hydrol. Earth Syst. Sci. 14 (2010) 1297–1308.

[108] N. Omani, R. Srinivasan, R. Karthikeyan, P.K. Smith, Impacts of climate change on the glacier melt runoff from five river basins, Trans. of the ASABE (2015). doi:10.13031/CC.20152114686.

[109] Shelie A. Miller, A. Amy E. Landis, Thomas L., Use of Monte Carlo analysis to characterize nitrogen fluxes in agroecosystems, Environ. Sci. Technol. 40 (2006) 2324–2332.

[110] C.S. Melching, C.G. Yoon, Key sources of uncertainty in QUAL2E model of Passaic River, J. Water Resour. Plan. Manag. 122 (1996) 105–113.

[111] G. Kuczera, E. Parent, Monte Carlo assessment of parameter uncertainty in conceptual catchment models: the Metropolis algorithm, J. Hydrol. 211 (1998) 69–85.

[112] J.A. Vrugt, H. V. Gupta, W. Bouten, S. Sorooshian, A Shuffled Complex Evolution Metropolis algorithm for optimization and uncertainty assessment of hydrologic model parameters, Water Resour. Res. 41 (2005) W08406.

[113] M. Thiemann, M. Trosset, H. Gupta, S. Sorooshian, Bayesian recursive parameter estimation for hydrologic models, Water Resour. Res. 37 (2001) 2521–2535.

[114] A. Montanari, Large sample behaviors of the generalized likelihood uncertainty estimation (GLUE) in assessing the uncertainty of rainfall-runoff simulations, Water Resour. Res. 41 (2005) W08406.

[115] D.P. Solomatine, D.L. Shrestha, A novel method to estimate model uncertainty using machine learning techniques, Water Resour. Res. 45 (2009) W08406.

[116] D.L. Shrestha, D.P. Solomatine, Data-driven approaches for estimating uncertainty in rainfall-runoff modelling, Int. J. River Basin Manag. 6 (2008) 109–122.

[117] S. Maskey, V. Guinot, R.K. Price, Treatment of precipitation uncertainty in rainfall-runoff modelling: a fuzzy set approach, Adv. Water Resour. 27 (2004) 889–898.

[118] H. Haario, M. Laine, A. Mira, E. Saksman, DRAM: Efficient adaptive MCMC, Stat. Comput. 16 (2006) 339–354.

[119] J.A. Vrugt, C.G.H. Diks, H. V. Gupta, W. Bouten, J.M. Verstraten, Improved treatment of uncertainty in hydrologic modeling: Combining the strengths of global optimization and data assimilation, Water Resour. Res. 41 (2005) W01017.

[120] H. Moradkhani, K.-L. Hsu, H. V Gupta, S. Sorooshian, Uncertainty assessment of hydrologic model states and parameters: Sequential data assimilation using the particle filter, Water Resour. Res. 41 (2005) W05012.

[121] Ajami N.K., Q. Duan, An integrated hydrologic Bayesian multimodel combination framework: Confronting input, parameter, and model structural uncertainty in hydrologic prediction, Water Resour. 43 (2007) 1–19.

[122] J.A. Vrugt, B.A. Robinson, Treatment of uncertainty using ensemble methods: Comparison of sequential data assimilation and Bayesian model averaging, Water Resour. Res. 43 (2007) W01411

[123] J.A. Vrugt, C.J.F. ter Braak, M.P. Clark, J.M. Hyman, B.A. Robinson, Treatment of input uncertainty in hydrologic modeling: Doing hydrology backward with Markov

chain Monte Carlo simulation, Water Resour. Res. 44 (2008) W00B09.

[124] R. Rostamian, A. Jaleh, M. Afyuni, S. farhad Mousavi, M. Heidarpour, A. Jalalian, K.C. Abbaspour, Application of a SWAT model for estimating runoff and sediment in two mountainous basins in central Iran, Hydrol. Sci. J. 53 (2008) 977–988.

[125] A. van Griensven, T. Meixner, A global and efficient multi-objective auto-calibration and uncertainty estimation method for water quality catchment models, J. Hydroinformatics. 9 (2007) 277–291.

[126] S. Samadi, M. Meadows, Examining the robustness of the SWAT distributed model using PSO and GLUE uncertainty frameworks, S.C. Water Resour. Conf. (2014).

[127] J. Yang, P. Reichert, K.C.C. Abbaspour, J. Xia, H. Yang, Comparing uncertainty analysis techniques for a SWAT application to the Chaohe Basin in China, J. Hydrol. 358 (2008) 1–23.

[128] H. Wu, B. Chen, Evaluating uncertainty estimates in distributed hydrological modeling for the Wenjing River watershed in China by GLUE, SUFI-2, and ParaSol methods, Ecol. Eng. 76 (2015) 110–121.

[129] B. Uniyal, M.K. Jha, A.K. Verma, Parameter identification and uncertainty analysis for simulating streamflow in a river basin of Eastern India, Hydrol. Process. 3766 (2015) 3744–3766.

[130] S.K. Jain, Assessment of environmental flow requirements for hydropower projects in India, Curr. Sci. 108 (2015) 1815–1825.

[131] J.J. Chen, A. Liao, X. Cao, L. Chen, X. Chen, C. He, G. Han, S. Peng, M. Lu, W. Zhang, X. Tong, J. Mills, Global land cover mapping at 30 m resolution: A POK-based operational approach, ISPRS J. Photogramm. Remote Sens. 103 (2015) 7–27.

[132] GFCC, Updated comprehensive plan of flood management of Gandak River system, Ganga Flood Control Comm. Minist. Water Resour. Gov. India. (2004).

[133] R.K. Dahal, S. Hasegawa, T. Masuda, M. Yamanaka, Roadside slope failures in nepal during torrential rainfall and their mitigation, in: Disaster Mitig. Debris Flows, Slope Fail. Landslides, Universal Academy Press, Inc., Tokyo, Japan, 2006: pp. 503–514.

[134] G. Kuczera, B. Renard, M. Thyer, D. Kavetski, There are no hydrological monsters, just models and observations with large uncertainties!, Hydrol. Sci. J. 55 (2010) 980–991.

[135] W.C. and C.E.M.T. A.R.Paz, J.M.Brabo, D.Allasia, Large-scale hydrodynamic modeling of a complex river network and floodplains, J. Hydrol. Eng. 15 (2010) 152–165.

[136] J.M. Bravo, D. Allasia, A.R. Paz, W. Collischonn, C.E.M. Tucci, Coupled hydrologic-hydraulic modeling of the upper Paraguay River Basin, J. Hydrol. Eng. 17 (2012) 635–646.

[137] M.C. Demirel, A. Venancio, E. Kahya, Flow forecast by SWAT model and ANN in Pracana basin, Portugal, Adv. Eng. Softw. 40 (2009) 467–473.

[138] R.C.D. Paiva, W. Collischonn, C.E.M. Tucci, Large scale hydrologic and hydrodynamic modeling using limited data and a GIS based approach, J. Hydrol. 406

(2011) 170–181.

[139] S.J. Pereira-Cardenal, N.D. Riegels, P.A.M. Berry, R.G. Smith, A. Yakovlev, T.U. Siegfried, P. Bauer-Gottwein, Real-time remote sensing driven river basin modeling using radar altimetry, Hydrol. Earth Syst. Sci. 15 (2011) 241–254.

[140] N. Pramanik, R.K. Panda, D. Sen, One dimensional hydrodynamic modeling of river flow using DEM extracted river cross-sections, Water Resour. Manag. 24 (2009) 835–852.

[141] P.A. Burrough, Principles of Geographical Information Systems for Land Resources Assessment, 2nd ed., Clarendon Press, Oxford, 1986.

[142] D. Han, M. Hammond, Issues of using digital maps for catchment delineation, Proc. ICE - Water Manag. 159 (2006) 45–51.

[143] Vladimir J. Alarcon and Chuck O' Hara, Using IFSAR and SRTM elevation data for watershed delineation, MAPPS/ASPRS 2006 Fall Conf. Novemb. 6-10, San Antonio, Texas. (2006).

[144] S.K. Jenson, J.O. Domingue, Extracting topographic structure from digital elevation data for geographic information system analysis, Photogrammatric Eng. Remote Sens. 54 (1988) 1593–1600.

[145] I.D. Moore, R.B. Grayson, Terrain-based catchment partitioning and runoff prediction using vector elevation data, Water Resour. Res. 27 (1991) 1177–1191.

[146] J. Fairfield, P. Leymarie, Drainage networks from grid digital elevation models, Water Resour. Res. 27 (1991) 709–717.

[147] M.C. Costa-Cabral, S.J. Burges, Digital Elevation Model Networks (DEMON): A model of flow over hillslopes for computation of contributing and dispersal areas, Water Resour. Res. 30 (1994) 1681–1692.

[148] S. Orlandini, Path-based methods for the determination of nondispersive drainage directions in grid-based digital elevation models, Water Resour. Res. 39 (2003) 1144.

[149] D.R. Maidment, Arc Hydro: GIS for water resources, (2002) 1–12.

[150] V.M. and M.P. P.Venkatachalam, B.Krishna Mohan, Amit Kotwal, Vikash Mishra, Automatic delineation of watersheds for hydrological applications, 22nd Asian Conferance Remote Sensing, Singapore. (2001).

[151] A.N. Strahler, Hypsometric (Area-Altitude) analysis of erosional topograply, Geol. Soc. Am. Bull. 63 (1952) 1117–1142.

[152] P.D. Jones, E.B. Horton, C.K. Folland, M. Hulme, D.E. Parker, T.A. Basnett, The use of indices to identify changes in climatic extremes, Clim. Change. 42 (1999) 131–149.

[153] C.K. Folland, P. Frich, T. Basnett, N. Rayner, D. Parker, B. Horton, Uncertainties in climate data sets - a challenge for WMO, WMO Bull. (2000) 59–68.

[154] A. Viglione, M. Borga, P. Balabanis, G. Blöschl, Barriers to the exchange of hydrometeorological data in Europe: Results from a survey and implications for data policy, J. Hydrol. 394 (2010) 63–77.

[155] B. Plengsaeng, U. Wehn, P. van der Zaag, Data-sharing bottlenecks in transboundary integrated water resources management: a case study of the Mekong River Commission's procedures for data sharing in the Thai context, Water Int. 39 (2014) 933–951.

[156] S.H. Rahman, B. Simon, Summer monsoon intraseasonal oscillation over eastern Arabian sea — As revealed by TRMM microwave imager products, J. Earth Syst. Sci. 115 (2006) 575–586.

[157] R.R.E. Vernimmen, A. Hooijer, E. Aldrian, a. I.J.M. van Dijk, Evaluation and bias correction of satellite rainfall data for drought monitoring in Indonesia, Hydrol. Earth Syst. Sci. 16 (2012) 133–146.

[158] D. Kneis, C. Chatterjee, R. Singh, Evaluation of TRMM rainfall estimates over a large Indian river basin (Mahanadi), Hydrol. Earth Syst. Sci. 18 (2014) 2493–2502.

[159] S. Jiang, L. Ren, Y. Hong, B. Yong, X. Yang, F. Yuan, M. Ma, Comprehensive evaluation of multi-satellite precipitation products with a dense rain gauge network and optimally merging their simulated hydrological flows using the Bayesian model averaging method, J. Hydrol. 452 (2012) 213–225.

[160] J. Wang, D.B. Wolff, J. Wang, D.B. Wolff, Evaluation of TRMM ground-validation radar-rain errors using rain gauge measurements, J. Appl. Meteorol. Climatol. 49 (2010) 310–324.

[161] M.M. Rahman, D. Singh Arya, N.K. Goel, A.K. Mitra, Rainfall statistics evaluation of ECMWF model and TRMM data over Bangladesh for flood related studies, Meteorol. Appl. 19 (2012) 501–512.

[162] W.U. Lu, Z. Panmao, Validation of daily precipitation from two high-resolution satellite precipitation datasets over the Tibetan plateau and the regions to its east, Acta. Meteor. Sin. 26 (2012) 735–745.

[163] Y. Chen, E.E. Ebert, K.J.E. Walsh, N.E. Davidson, Evaluation of TRMM 3B42 precipitation estimates of tropical cyclone rainfall using PACRAIN data, J. Geophys. Res. Atmos. 118 (2013) 2184–2196.

[164] S. Prakash, A.K. Mitra, D.S. Pai, Comparing two high-resolution gauge-adjusted multisatellite rainfall products over India for the southwest monsoon period, Meteorol. Appl. 22 (2015) 679–688.

[165] V. Bharti, C. Singh, Evaluation of error in TRMM 3B42V7 precipitation estimates over the Himalayan region, J. Geophys. Res. Atmos. 120 (2015) 12458–12473.

[166] M.F. Müller, S.E. Thompson, Bias adjustment of satellite rainfall data through stochastic modeling: Methods development and application to Nepal, Adv. Water Resour. 60 (2013) 121–134.

[167] T.P.R. Team, Tropical Rainfall Measuring Mission (TRMM) precipitation radar algorithm instruction manual, 2011.

[168] S. Sorooshian, K.L. Hsu, X. Gao, H. V. Gupta, B. Imam, D. Braithwaite, Evaluation of PERSIANN system satellite-based estimates of tropical rainfall, Bull. Am. Meteorol. Soc. 81 (2000) 2035–2046.

[169] S. Shige, T. Yamamoto, T. Tsukiyama, S. Kida, H. Ashiwake, T. Kubota, S. Seto, K.

Aonashi, K. Okamoto, The GSMaP precipitation retrieval algorithm for microwave sounders—Part I: over-ocean algorithm, IEEE Trans. Geosci. Remote Sens. 47 (2009) 3084–3097.

[170] R.J. Joyce, J.E. Janowiak, P.A. Arkin, P. Xie, R.J. Joyce, J.E. Janowiak, P.A. Arkin, P. Xie, CMORPH: A method that produces global precipitation estimates from passive microwave and infrared data at high spatial and temporal resolution, J. Hydrometeorol. 5 (2004) 487–503.

[171] J. Guo, P. Zhai, L. Wu, M. Cribb, Z. Li, Z. Ma, F. Wang, D. Chu, P. Wang, J. Zhang, Diurnal variation and the influential factors of precipitation from surface and satellite measurements in Tibet, Int. J. Climatol. 34 (2013) 2940–2956.

[172] X. Xue, Y. Hong, A.S. Limaye, J.J. Gourley, G.J. Huffman, S.I. Khan, C. Dorji, S. Chen, Statistical and hydrological evaluation of TRMM-based Multi-satellite Precipitation Analysis over the Wangchu Basin of Bhutan: Are the latest satellite precipitation products 3B42V7 ready for use in ungauged basins?, J. Hydrol. 499 (2013) 91–99.

[173] N. Krakauer, S. Pradhanang, T. Lakhankar, A. Jha, Evaluating satellite products for precipitation estimation in mountain regions: A case study for Nepal, Remote Sens. 5 (2013) 4107–4123.

[174] D. Chu, T. Pubu, G. Norbu, B. Sagar, S. Mandira, J. Guo, Validation of the satellite-derived rainfall estimates over the Tibet, Acta Meteorol. Sin. 25 (2011) 734–741.

[175] M.S. Shrestha, G.A. Artan, S.R. Bajracharya, D.K. Gautam, S.A. Tokar, Bias-adjusted satellite-based rainfall estimates for predicting floods: Narayani Basin, J. Flood Risk Manag. 4 (2011) 360–373.

[176] M.N. Islam, S. Das, H. Uyeda, Calibration of TRMM derived rainfall over Nepal during 1998-2007, Open Atmos. Sci. J. 4 (2010) 12–23.

[177] G.J. Huffman, D.T. Bolvin, E.J. Nelkin, D.B. Wolff, R.F. Adler, G. Gu, Y. Hong, K.P. Bowman, E.F. Stocker, The TRMM Multisatellite Precipitation Analysis (TMPA): Quasi-global, multiyear, combined-sensor precipitation estimates at fine scales, J. Hydrometeorol. 8 (2007) 38–55.

[178] G.J. Huffman, R.F. Adler, D.T. Bolvin, E.J. Nelkin, The TRMM Multi-Satellite Precipitation Analysis (TMPA), in: Satell. Rainfall Appl. Surf. Hydrol., Springer Netherlands, Dordrecht, 2010: pp. 3–22.

[179] A.E. Brito, S.H. Chan, S.D. Cabrera, SAR image superresolution via 2-D adaptive extrapolation, Multidimens. Syst. Signal Process. 14 (2003) 83–104.

[180] H. Kühl, M.D. Sacchi, Least-squares wave-equation migration for AVP/AVA inversion, GEOPHYSICS. 68 (2003) 262–273.

[181] K.T. Gribbon, D.G. Bailey, A novel approach to real-time bilinear interpolation, in: Second IEEE Int. Work. Electron. Des. Test Appl., IEEE, 2004: pp. 126–126.

[182] D.N. Arnold, D. Boffi, R.S. Falk, P.G. Ciarlet, B. Nagy, H. Federer, V. Girault, P.-A. Raviart, R. Rannacher, S. Turek, J. Zhang, F. Kikuchi, Approximation by quadrilateral finite elements, Math. Comput. 71 (2002) 909–922.

[183] A.H. Murphy, What is a good forecast? An essay on the nature of goodness in

weather forecasting, Weather Forecast. 8 (1993) 281–293.

[184] D.S. Wilks, Statistical methods in the atmospheric sciences, Acad. Press 2011.

[185] D.S. Wilks, Statistical methods in the atmosphere, Acad. Press 2006.

[186] H.R. Stanski, L.J. Wilson, W.R. Burrows, Survey of common verfication methods in meteorology - 2, Atmos. Res. (1989) 9–42.

[187] B.G. Brown, G. Thompson, R.T. Bruintjes, R. Bullock, T. Kane, Intercomparison of in-flight icing algorithms. part II: statistical verification results, Weather Forecast. 12 (1997) 890–914.

[188] WMO TD No. 1485, Recommendations for the verification and intercomparison of QPFs and PQPFs from operational NWP models, 2009.

[189] J. Qiu, Pollutants capture the high ground in the himalayas, Science (80-.). 339 (2013) 1030–1.

[190] Grumbine et al., Threats from India's Himalaya dams., Science. 339 (2013) 36–37.

[191] J. Qiu, Organic pollutants poison the roof of the world, Nature. (2013) doi:10.1038/nature.2013.12776.

[192] C.P. Kala, Indigenous uses, population density, and conservation of threatened medicinal plants in protected areas of the Indian Himalayas, Conserv. Biol. 19 (2005) 368–378. doi:10.1111/j.1523-1739.2005.00602.x.

[193] A.K. Misra, A River about to Die: Yamuna, J. Water Resour. Prot. 2 (2010) 489–500.

[194] R.J. Rao, Biological resources of the Ganga River, India, Hydrobiologia. 458 (2001) 159–168.

[195] S.C. Sati, P.C. Paliwal, Physico-chemical and bacteriological analysis of Kosi River water in central Himalaya, Pollut. Res. 27 (2008) 179–183.

[196] Y. Sharma, Case Study I * - The Ganga , India, Water Pollut. Control - A Guid. to Use Water Qual. Manag. Princ. (1997).

[197] M.K. Pandit, The Himalayas must be protected, Nature. 501 (2013) 283.

[198] Z.Y. Shen, L. Chen, Q. Liao, R.M. Liu, Q. Huang, A comprehensive study of the effect of GIS data on hydrology and non-point source pollution modeling, Agric. Water Manag. 118 (2013) 93–102.

[199] R.M. Darbra, E. Eljarrat, D. Barceló, How to measure uncertainties in environmental risk assessment, Trends Anal. Chem. 27 (2008) 377–385.

[200] T. Wagener, H. V. Gupta, Model identification for hydrological forecasting under uncertainty, Stoch. Environ. Res. Risk Assess. 19 (2005) 378–387.

[201] R.A. Skeffington, P.G. Whitehead, J. Abbott, Quantifying uncertainty in critical loads: (B) acidity mass balance critical loads on a sensitive site, Water. Air. Soil Pollut. 169 (2006) 25–46.

[202] M. Faramarzi, K.C. Abbaspour, S. Ashraf Vaghefi, M.R. Farzaneh, A.J.B. Zehnder, R. Srinivasan, H. Yang, Modeling impacts of climate change on freshwater

availability in Africa, J. Hydrol. 480 (2013) 85–101.

[203] H. Bormann, Sensitivity of a soil-vegetation-atmosphere-transfer scheme to input data resolution and data classification, J. Hydrol. 351 (2008) 154–169.

[204] M.J. Booij, Impact of climate change on river flooding assessed with different spatial model resolution, J. Hydrol. 303 (2005) 176–198.

[205] S. Fu, T.O. Sonnenborg, K.H. Jensen, X. He, Impact of precipitation spatial resolution on the hydrological response of an integrated distributed water resources model, Vadose Zo. J. 10 (2011) 25.

[206] P. Yang, D.P. Ames, A. Fonseca, D. Anderson, R. Shrestha, N.F. Glenn, Y. Cao, What is the effect of LiDAR-derived DEM resolution on large-scale watershed model results?, Environ. Model. Softw. 58 (2014) 48–57.

[207] A. Sharma, K.N. Tiwari, A comparative appraisal of hydrological behavior of SRTM DEM at catchment level, J. Hydrol. 519 (2014) 1394–1404.

[208] S.K. Jain, A. Goswami, A.. Saraf, Role of elevation and aspect in snow distribution in western Himalaya, Water Resour. Manag. 23 (2008) 71–83.

[209] T. Grunewald, Y. Buhler, M. Lehning, Elevation dependency of mountain snow depth, Cryosphere. 8 (2014) 2381–2394.

[210] R. Kour, N. Patel, A.P. Krishna, Effects of terrain attributes on snow cover dynamics in parts of chenab basin, western Himalayas, Hydrol. Sci. J. 61 (2016) 1861–1876.

[211] K. Shichang, K.J. Kreutz, P.A. Mayewski, D. Qin, T. Yao, Stable-isotopic composition of precipitation over the northern slope of the central Himalaya, J. Glaciol. 48 (2002) 519–526.

[212] A. Sen Gupta, D.G. Tarboton, P. Hummel, M.E. Brown, S. Habib, Integration of an energy balance snowmelt model into an open source modeling framework, Environ. Model. Softw. 68 (2015) 205–218.

[213] J.G. Arnold, R. Srinivasan, R.S. Muttiah, J.R. Williams, Large area hydrologic modeling and assessment part I: model development, J. Am. Water Resour. Assoc. 34 (1998) 73–89.

[214] M. Rohrer, N. Salzmann, M. Stoffel, A. V. Kulkarni, Missing (in-situ) snow cover data hampers climate change and runoff studies in the Greater Himalayas, Sci. Total Environ. 468–469 (2013) S60–S70.

[215] R. Hock, Temperature index melt modelling in mountain areas, J. Hydrol. 282 (2003) 104–115.

[216] B. Debele, R. Srinivasan, A.K. Gosain, Comparison of process-based and temperature-index snowmelt modeling in SWAT, Water Resour. Manag. 24 (2010) 1065–1088.

[217] M. Winchell, R. Srinivasan, M. Di Luzio, J.G. Arnold, ArcSWAT user's guide, (2013) 464.

[218] K. Rahman, C. Maringanti, M. Beniston, F. Widmer, K. Abbaspour, A. Lehmann, Streamflow modeling in a highly managed mountainous glacier watershed using SWAT: The upper Rhone River watershed case in Switzerland, Water Resour.

Manag. 27 (2013) 323–339.

[219] E.J. Gabet, B.A. Pratt-Sitaula, D.W. Burbank, Climatic controls on hillslope angle and relief in the Himalayas, Geology. 32 (2004) 629–632.

[220] R. Wen, L. De Tian, Y.B. Weng, Z.F. Liu, Z.P. Zhao, The altitude effect of δ18 O in precipitation and river water in the Southern Himalayas, Chinese Sci. Bull. 57 (2012) 1693–1698.

[221] P. Singh, N. Kumar, M. Arora, Degree-day factors for snow and ice for Dokriani Glacier, Garhwal Himalayas, J. Hydrol. 235 (2000) 1–11.

[222] W.W. Immerzeel, L. Petersen, S. Ragettli, F. Pellicciotti, The importance of observed gradients of air temperature and precipitation for modeling runoff from a glacierized watershed in the Nepalese Himalayas, Water Resour. Res. 50 (2014) 2212–2226.

[223] T. Haiden, G. Pistotnik, Intensity-dependent parameterization of elevation effects in precipitation analysis, Adv. Geosci. 20 (2009) 33–38.

[224] D.B. Kattel, T. Yao, K. Yang, L. Tian, G. Yang, D. Joswiak, Temperature lapse rate in complex mountain terrain on the southern slope of the central Himalayas, Theor. Appl. Climatol. 113 (2013) 671–682.

[225] J.R. Minder, P.W. Mote, J.D. Lundquist, Surface temperature lapse rates over complex terrain: Lessons from the Cascade Mountains, J. Geophys. Res. Atmos. 115 (2010) D1422.

[226] P. Singh, N. Kumar, Effect of orography on precipitation in the western Himalayan region, J. Hydrol. 199 (1997) 183–206.

[227] B. Ding, K. Yang, J. Qin, L. Wang, Y. Chen, X. He, The dependence of precipitation types on surface elevation and meteorological conditions and its parameterization, J. Hydrol. 513 (2014) 154–163.

[228] S. Nepal, A.B. Shrestha, Impact of climate change on the hydrological regime of the Indus, Ganges and Brahmaputra river basins: a review of the literature, Int. J. Water Resour. Dev. 627 (2015) 1–18.

[229] S. Saha, S. Moorthi, X. Wu, J. Wang, S. Nadiga, P. Tripp, D. Behringer, Y.T. Hou, H.Y. Chuang, M. Iredell, M. Ek, J. Meng, R. Yang, M.P. Mendez, H. Van Den Dool, Q. Zhang, W. Wang, M. Chen, E. Becker, The NCEP climate forecast system version 2, J. Clim. 27 (2014) 2185–2208.

[230] A. Yatagai, K. Kamiguchi, O. Arakawa, A. Hamada, N. Yasutomi, A. Kitoh, Aphrodite constructing a long-term daily gridded precipitation dataset for Asia based on a dense network of rain gauges, Bull. Am. Meteorol. Soc. 93 (2012) 1401–1415.

[231] A. Jarvis, H.I. Reuter, A. Nelson, E. Guevara, Hole-filled SRTM for the globe version 4, Available from CGIAR-CSI SRTM 90 M Database. (2008)

[232] S.. Neitsch, J.. Arnold, J.. Kiniry, J.. Williams, Soil & Water Assessment Tool Theoretical Documentation Version 2009, Texas Water Resour. Institute, TR-406. (2011) 1–647.

[233] J.R. Williams, H.D. Berndt, Sediment yield prediction based on watershed hydrology, Trans. Am. Soc. Agric. Eng. 20 (1977) 1100–1104.

[234] A.D. McElroy, S.Y. Chiu, J.W. Nebgen, A. Aleti, F.W. Bennett, Loading functions for assessment of water pollution from nonpoint sources, EPA Doc. EPA 600/2-76-151USEPA, Athens, GA. (1976).

[235] J. Williams, R. Hann, Optimal operation of large agricultural watersheds with water quality restraints, Texas Water Resour. Institute. TR-96 (1978).

[236] D.R. Gurung, A. Giriraj, K.S. Aung, B. Shrestha, A. V Kulkarni, Snow-cover mapping and monitoring in the Hindu Kush-Himalayas, Int. Cent. Integr. Mt. Dev. (2011) 1–44.

[237] K.. Sharma, Role of meltwater in major river systems of Nepal, in: Snow Glacier Hydrol. (Proceedings Kathmandu Symp., 1993: pp. 113–122.

[238] E.A. Anderson, A point energy and mass balance model of a snow cover, Energy. 114 (1976) 150.

[239] W.W. Immerzeel, L.P.H. van Beek, M.F.P. Bierkens, Climate change will affect the Asian water towers., Science. 328 (2010) 1382–5.

[240] T.P. Barnett, J.C. Adam, D.P. Lettenmaier, Potential impacts of a warming climate on water availability in snow-dominated regions, Nature. 438 (2005) 303–309.

[241] W.W. Immerzeel, P. Droogers, S.M. de Jong, M.F.P. Bierkens, Large-scale monitoring of snow cover and runoff simulation in Himalayan river basins using remote sensing, Remote Sens. Environ. 113 (2009) 40–49.

[242] S.W. Rex Victor Cruz, Hideo Harasawa, Murari Lal, Asia, in: J. Parry, M, Canziani, O, Palutikof (Ed.), Clim. Chang. 2007 Impacts, Adapt. Vulnerability, M. L. Parr, Cambridge University Press, New York, 2007: pp. 469–506.

[243] J. Martinec, Snowmelt - Runoff model for stream flow forecasts, Hydrol. Res. 6 (1975) 145–154.

[244] M.E. Brown, A.E. Racoviteanu, D.G. Tarboton, A. Sen Gupta, J. Nigro, F. Policelli, S. Habib, M. Tokay, M.S. Shrestha, S. Bajracharya, P. Hummel, M. Gray, P. Duda, B. Zaitchik, V. Mahat, G. Artan, S. Tokar, An integrated modeling system for estimating glacier and snow melt driven streamflow from remote sensing and earth system data products in the Himalayas, J. Hydrol. 519 (2014) 1859–1869.

[245] A. Kushwaha, M.K. Jain, Hydrological simulation in a forest dominated watershed in Himalayan Region using SWAT model, Water Resour. Manag. 27 (2013) 3005–3023.

[246] M. Shrestha, L. Wang, T. Koike, Y. Xue, Y. Hirabayashi, M. Shrestha, L. Wang, T. Koike, Y. Xue, Y. Hirabayashi, Modeling the spatial distribution of snow cover in the dudhkoshi region of the Nepal Himalayas, J. Hydrometeorol. 13 (2012) 204–222.

[247] K.P.S. Ram Gopal Kharbuja, Impact of climate changes on hydrology of the Narayani basin : distributed Top Model-based assessment, J. Hydrol. Meteorol. 5 (2008) 1–14.

[248] B. Bookhagen, D.W. Burbank, Toward a complete Himalayan hydrological budget: Spatiotemporal distribution of snowmelt and rainfall and their impact on river discharge, J. Geophys. Res. Earth Surf. 115 (2010) 1–25.

[249] L.P. Devkota, D.R. Gyawali, Impacts of climate change on hydrological regime and water resources management of the Koshi River Basin, Nepal, J. Hydrol. Reg. Stud. 4 (2015) 502–515.

[250] S.M. Pradhanang, A. Anandhi, R. Mukundan, M.S. Zion, D.C. Pierson, E.M. Schneiderman, A. Matonse, A. Frei, Application of SWAT model to assess snowpack development and streamflow in the Cannonsville watershed, New York, USA, Hydrol. Process. 25 (2011) 3268–3277.

[251] C. Siderius, H. Biemans, A. Wiltshire, S. Rao, W.H.P. Franssen, P. Kumar, A.K. Gosain, M.T.H. van Vliet, D.N. Collins, Snowmelt contributions to discharge of the Ganges, Sci. Total Environ. 468 (2013) S93–S101.

[252] B. Fang, V. Lakshmi, Soil moisture at watershed scale: Remote sensing techniques, J. Hydrol. 516 (2014) 258–272.

[253] V. Lakshmi, The role of satellite remote sensing in the Prediction of Ungauged Basins, Hydrol. Process. 18 (2004) 1029–1034.

[254] V. Lakshmi, Beyond GRACE: Using satellite data for groundwater investigations, Groundwater. 54 (2016) 615-618..

[255] A.J. Dietz, C. Kuenzer, U. Gessner, S. Dech, Remote sensing of snow – a review of available methods, Int. J. Remote Sens. 33 (2012) 4094–4134.

[256] A. Yatagai, K. Kamiguchi, O. Arakawa, A. Hamada, N. Yasutomi, A. Kitoh, A. Yatagai, K. Kamiguchi, O. Arakawa, A. Hamada, N. Yasutomi, A. Kitoh, Aphrodite constructing a long-term daily gridded precipitation dataset for Asia based on a dense network of rain gauges, Bull. Am. Meteorol. Soc. 93 (2012) 1401–1415.

[257] P. Kishore, S. Jyothi, G. Basha, S.V.B. Rao, M. Rajeevan, I. Velicogna, T.C. Sutterley, Precipitation climatology over India: validation with observations and reanalysis datasets and spatial trends, Clim. Dyn. 46 (2016) 541–556.

[258] W. Wang, P. Xie, S.-H. Yoo, Y. Xue, A. Kumar, X. Wu, An assessment of the surface climate in the NCEP climate forecast system reanalysis, Clim. Dyn. 37 (2011) 1601–1620.

[259] V. Misra, P. Pantina, S. C. Chan, S. DiNapoli, A comparative study of the Indian summer monsoon hydroclimate and its variations in three reanalyses, Clim. Dyn. 39 (2012) 1149–1168.

[260] M.M. Nageswararao, U.C. Mohanty, S. Kiran Prasad, K.K. Osuri, S.S.V.S. Ramakrishna, Performance evaluation of NCEP climate forecast system for the prediction of winter temperatures over India, Theor. Appl. Climatol. 126 (2015) 437–451.

[261] C. Andermann, S. Bonnet, R. Gloaguen, Evaluation of precipitation data sets along the Himalayan front, Geochemistry, Geophys. Geosystems. 12 (2011) Q07023.

[262] S.K. Jain, A. Goswami, A.K. Saraf, Accuracy assessment of MODIS, NOAA and IRS data in snow cover mapping under Himalayan conditions, Int. J. Remote Sens. 29 (2008) 5863–5878.

[263] P. Mishra, V. V. Zaphu, N. Monica, A. Bhadra, A. Bandyopadhyay, Accuracy assessment of MODIS fractional snow cover product for eastern Himalayan

catchment, J. Indian Soc. Remote Sens. 44 (2016) 977–98.

[264] Z. Pu, L. Xu, V. V. Salomonson, MODIS/Terra observed seasonal variations of snow cover over the Tibetan Plateau, Geophys. Res. Lett. 34 (2007) L06706.

[265] X. Li, M.W. Williams, Snowmelt runoff modelling in an arid mountain watershed, Tarim Basin, China, Hydrol. Process. 22 (2008) 3931–3940.

[266] S. Maskey, S. Uhlenbrook, S. Ojha, An analysis of snow cover changes in the Himalayan region using MODIS snow products and in-situ temperature data, Clim. Change. 108 (2011) 391–400.

[267] L. Brown, R. Thorne, M. Woo, Using satellite imagery to validate snow distribution simulated by a hydrological model in large northern basins, Hydrol. Process. 22 (2008) 2777–2787.

[268] J. Dwyer, G. Schmidt, The MODIS reprojection tool, in: Earth Sci. Satell. Remote Sens., 2006: pp. 162–177.

[269] J. Parajka, G. Blöschl, Spatio-temporal combination of MODIS images - potential for snow cover mapping, Water Resour. Res. 44 (2008) W03406.

[270] P.W. Gassman, M.R. Reyes, C.H. Green, J.G. Arnold, The soil and water assessment tool: Historical development, applications, and future research directions, Trans. ASABE. 50 (2007) 1211–1250.

[271] P.W. Gassman, A.M. Sadeghi, R. Srinivasan, Applications of the SWAT model special section: Overview and insights, J. Environ. Qual. (2014) 1–8.

[272] X. Zhang, R. Srinivasan, B. Debele, F. Hao, Runoff simulation of the headwaters of the Yellow River using the SWAT model with three snowmelt algorithms, J. Am. Water Resour. Assoc. 44 (2008) 48–61.

[273] K.C. Abbaspour, SWAT-CUP 2012: SWAT calibration and uncertainty programs - A user manual, Eawag Swishs Fed. Inst. Aquat. Sci. Technol. (2015) 106.

[274] J.G. Arnold, D.N. Moriasi, P.W. Gassman, K.C. Abbaspour, M.J. White, R. Srinivasan, C. Santhi, R.D. Harmel, a. Van Griensven, M.W. VanLiew, N. Kannan, M.K. Jha, SWAT: Model use, calibration, and validation, Trans. ASABE. 55 (2012) 1491–1508.

[275] Y. Luo, J. Arnold, S. Liu, X. Wang, X. Chen, Inclusion of glacier processes for distributed hydrological modeling at basin scale with application to a watershed in Tianshan Mountains, northwest China, J. Hydrol. 477 (2013) 72–85.

[276] X.-Y. Meng, D.-L. Yu, Z.-H. Liu, Energy balance-based SWAT model to simulate the mountain snowmelt and runoff — taking the application in Juntanghu watershed (China) as an example, J. Mt. Sci. 12 (2015) 368–381.

[277] M.D. McKay, R.J. Beckman, W.J. Conover, A comparison of three methods for selecting values of input variables in the analysis of output from a computer code, Technometrics. 21 (1979) 239.

[278] F. Pellicciotti, C. Buergi, W.W. Immerzeel, M. Konz, A.B. Shrestha, Challenges and uncertainties in hydrological modeling of remote Hindu Kush–Karakoram–Himalayan (HKH) basins: Suggestions for calibration strategies, Mt. Res. Dev. 32

(2012) 39–50.

[279] F. Brun, M. Dumont, P. Wagnon, E. Berthier, M.F. Azam, J.M. Shea, P. Sirguey, A. Rabatel, A. Ramanathan, Seasonal changes in surface albedo of Himalayan glaciers from MODIS data and links with the annual mass balance, Cryosph. 9 (2015) 341–355.

[280] A.G. Klein, A.C. Barnett, Validation of daily MODIS snow cover maps of the Upper Rio Grande River Basin for the 2000-2001 snow year, Remote Sens. Environ. 86 (2003) 162–176.

[281] C. Andermann, L. Longuevergne, S. Bonnet, A. Crave, P. Davy, R. Gloaguen, Impact of transient groundwater storage on the discharge of Himalayan rivers, Nat. Geosci. 5 (2012) 127–132.

[282] L. Lambert, B.D. Chitrakar, Variation of potential evapotranspiration with elevation in Nepal, Mt. Res. Dev. 9 (1989) 145–152.

[283] L. Gerlitz, B. Bechtel, J. Böhner, M. Bobrowski, B. Bürzle, M. Müller, T. Scholten, U. Schickhoff, N. Schwab, J. Weidinger, Analytic comparison of temperature lapse rates and precipitation gradients in a Himalayan treeline environment: Implications for statistical downscaling, in: Clim. Chang. Glacier Response, Veg. Dyn. Himalaya, Springer International Publishing, Cham, 2016: pp. 49–64.

[284] R.J. Thayyen, J.T. Gergan, D.P. Dobhal, Slope lapse rates of temperature in Din Gad (Dokriani Glacier) catchment , Garhwal Himalaya, India, Bull. Glaciol. Res. 22 (2005) 31–37.

[285] D.B. Kattel, T. Yao, W. Yang, Y. Gao, L. Tian, Comparison of temperature lapse rates from the northern to the southern slopes of the Himalayas, Int. J. Climatol. 35 (2015) 4431–4443.

[286] V. Jain, R. Sinha, Geomorphological manifestations of the flood hazard: A remote sensing based approach, Geocarto Int. 18 (2003) 51–60.

[287] J. Qiu, Droughts threaten high-altitude Himalayan forests, Nature. (2015). doi:10.1038/nature.2015.16806.

[288] R. Pushpalatha, C. Perrin, N. Le Moine, T. Mathevet, V. Andréassian, A downward structural sensitivity analysis of hydrological models to improve low-flow simulation, J. Hydrol. 411 (2011) 66–76.

[289] S. Shukla, D.P. Lettenmaier, Seasonal hydrologic prediction in the United States: understanding the role of initial hydrologic conditions and seasonal climate forecast skill, Hydrol. Earth Syst. Sci. 15 (2011) 3529–3538.

[290] L. Zaharia, R. Costache, R. Prăvălie, G. Minea, Assessment and mapping of flood potential in the Slănic catchment in Romania, J. Earth Syst. Sci. 124 (2015) 1311–1324.

[291] M.M. Rahman, N.K. Goel, D.S. Arya, Development of the Jamuneswari flood forecasting system : Case study in Bangladesh, J. Hydrol. Eng. 17 (2012) 1123–1140.

[292] B. Nishat, S.M.M. Rahman, Water resources modeling of the Ganges-Brahmaputra-Meghna River basins using satellite remote sensing data, JAWRA J. Am. Water Resour. Assoc. 45 (2009) 1313–1327.

[293] V. Maggioni, P.C. Meyers, M.D. Robinson, V. Maggioni, P.C. Meyers, M.D. Robinson, A review of merged high-resolution satellite precipitation product accuracy during the tropical rainfall measuring mission (TRMM) Era, J. Hydrometeorol. 17 (2016) 1101–1117.

[294] S. Prakash, C. Mahesh, V. Sathiyamoorthy, R.M. Gairola, a. K. Mitra, An investigation of long-term changes in rainfall over the equatorial Indian Ocean trough region during northern summer using multisatellite data, Theor. Appl. Climatol. 124 (2015) 129–139.

[295] Saha et al., The NCEP climate forecast system reanalysis, Bull. Am. Meteorol. Soc. 91 (2010) 1015–1057.

[296] Y.T. Dile, R. Srinivasan, Evaluation of CFSR climate data for hydrologic prediction in data-scarce watersheds: an application in the Blue Nile River Basin, JAWRA J. Am. Water Resour. Assoc. 50 (2014) 1226–1241.

[297] V. Te Chow, D.R. Maidment, L.W. Mays, Applied hydrology, Tata McGraw-Hill Education, 2010.

[298] USDA-SCS, Section 4: Hydrology, in: Natl. Eng. Handb., 1972: pp. 10-1-10–22.

[299] H.V. Gupta, S. Sorooshian, P.O. Yapo, Status of automatic calibration for hydrologic models: Comparison with multilevel expert calibration, J. Hydrol. Eng. 4 (1999) 135–143.

[300] D.R. Legates, G.J. McCabe, Evaluating the use of "goodness-of-fit" Measures in hydrologic and hydroclimatic model validation, Water Resour. Res. 35 (1999) 233–241.

[301] D.N. Moriasi, J.G. Arnold, M.W. Van Liew, R.L. Binger, R.D. Harmel, T.L. Veith, Model evaluation guidelines for systematic quantification of accuracy in watershed simulations, Trans. ASABE. 50 (2007) 885–900.

[302] B. Kumar, K.C. Patra, V. Lakshmi, Daily rainfall statistics of TRMM and CMORPH: A case for trans-boundary Gandak River basin, J. Earth Syst. Sci. 125 (2016) 919–934.

Dissemination

Journal Articles

[1] Brijesh Kumar, Kanhu Charan Patr, Venkat Lakshmi (2016). Error in Digital Network and Basin Area Delineation using D8 Method: A Case Study in a Sub-basin of the Ganga, Journal of Geological Society of India, Springer, Vol. 89(1), pp. 65-70.

[2] Brijesh Kumar, Kanhu Charan Patra, Venkat Lakshmi (2016). Daily rainfall statistics of TRMM and CMORPH: A case for trans-boundary Gandak River basin, Earth System Sciences, Springer, Vol. 125(5), pp. 919-935.

[3] Brijesh Kumar, Venkat Lakshmi, Kanhu Charan Patra (2016). Evaluating the Uncertainties in the SWAT Model Outputs due to DEM Grid Size and Resampling Techniques in a Large Himalayan River Basin, Journal of Hydrological Engineering, ASCE, 22(9), pp. 04017039.

[4] Brijesh Kumar, Venkat Lakshmi, Kanhu Charan Patra (2017). Assessing the Suitability of SWAT model to simulate snow cover, snowmelt and stream flow dynamics in a large Himalayan River basin, Journal of Hydrology, Elsevier (Under Review).

[5] Brijesh Kumar, Venakt Lakshmi, Kanhu Charan Patra (2017). Accessing the Capability of TRMM 3B42 V7 to Simulate Streamflow during Extreme Rain Events: Case Study for a Himalayan River Basin, Journal of Earth System Sciences, Springer (Accepted).

Conference Presentations

[1] Brijesh Kumar, Venkat Lakshmi, Kanhu Charan Patra (2016). Assessing Hydrological Uncertainties Using the SWAT model to Simulate Stream flow over the Alpine Himalayas. American Geological Union (AGU) held at San Francisco, USA at 12-16 December, and Paper ID: H43A-1392.

[2] Brijesh Kumar, Kanhu Charan Patra, Venkat Lakshmi (2016). Evaluating Hydrological Uncertainties Arising due to DEM resolution: Study for Himalayan River Basin Gandak. ETAE 2016 held at IIT Kharagpur-27-30 December 2016.

Book Chapters

[1] Brijesh Kumar, K.C. Patra, Venkat Lakshmi (2016). Precision Farming and Resource Management, Evaluating Hydrological Uncertainties Arising due to DEM resolution (24). Excel India Publisher, New Delhi, ISBN: 978-93-86256-29-4.